Alma Mater Studiorum – Università di Bologna

School of Science
Department of Physics and Astronomy
Master Degree Program in Astrophysics and Cosmology

On The Gamma-Ray Emission From The Neutrino Emitter NGC 1068: Prospects For Future Ground-Based Observatories And Space-Based Missions

Graduation Thesis

Presented by:
Denise Sammartino

Supervisor:
Chiar.mo Prof.Cristian Vignali

Co-Supervisors:
Dott.ssa Paula Kornecki
Dott. Daniel Morcuende Parrilla

Accademic Year 2024/2025

Abstract

The galaxy NGC 1068 represents one of the most intriguing and well-studied obscured, Seyfert 2 galaxies in the nearby Universe. Located at a distance of approximately 14 Mpc, NGC 1068 exhibits a composite nature, hosting both a luminous Active Galactic Nucleus powered by accretion onto a supermassive black hole and an intense starburst region that contributes significantly to its emission. Its complex structure, characterized by obscuring material in the circumnuclear region and powerful outflows, makes it an interesting target for investigating the connection between nuclear activity and star formation, as well as for exploring potential sites of cosmic-ray acceleration.
Recently, the IceCube collaboration has reported evidence for high-energy neutrino emission from the direction of NGC 1068. This discovery strongly suggests the presence of hadronic acceleration processes within the source, in which protons or heavier nuclei interact with ambient matter or radiation fields, producing charged and neutral pions that decay into neutrinos and gamma rays, respectively. Consequently, if neutrino emission indeed originates from NGC 1068, one would also expect corresponding very high energy gamma-ray emission.
My thesis aims to characterize the gamma-ray emission from NGC 1068 using recent observations carried out by the Large-Sized Telescope prototype (LST-1), the first operational prototype of the future Cherenkov Telescope Array Observatory (CTAO), which is under construction and represents the next generation of ground-based gamma-ray observatories. It will consist of an array of telescopes of different sizes (Large, Medium, and Small) distributed across two sites in the northern and southern hemispheres. This configuration will allow CTAO to cover an unprecedented energy range, from a few tens of GeV up to several hundreds of TeV, with sensitivities up to an order of magnitude better than current instruments. LST-1, located on the island of La Palma (Canary Islands), is designed to explore the low-energy domain of CTAO, with a threshold of about 20–30 GeV.
In addition to LST-1 data, my study makes use of archival observations from the Fermi-LAT telescope, the MAGIC observatory, and the Very Large Array (VLA), thereby providing a comprehensive multiwavelength context for the analysis. The analysis combines data reduction, spectral fitting, and temporal studies to constrain the gamma-ray emission from the source. Furthermore, the study incorporates the instrument response functions of upcoming facilities, such as the full CTAO and future MeV gamma-ray missions, to assess their potential for detecting or constraining the emission from NGC 1068.
Part of my work focuses on the investigation of the so-called "MeV gap," a spectral region between a few hundred keV and several tens of MeV that remains poorly explored due to the lack of sufficiently sensitive instruments. This region is crucial for understanding the transition between thermal and non-thermal processes in astrophysical sources. To this end, we evaluate the capabilities of the upcoming Compton Spectrometer and Imager (COSI), a NASA MeV gamma-ray space mission scheduled for launch in 2027. COSI will operate in the 0.2–5 MeV energy range, using advanced Compton imaging techniques to achieve unprecedented sensitivity and energy resolution.
The work presented in this thesis is divided into two main parts. The first part focuses on the analysis of observational data, in particular the reduction and processing of LST-1 observations. Through this analysis, we derived upper limits in the upper-TeV range. Furthermore, an in-depth investigation of the dataset revealed background-related issues affecting the lower-energy regime (below 0.6 TeV), which limited the reliability of po-

tential detections in that energy band.
The second part of my thesis is dedicated to the theoretical modeling of the non-thermal emission from the starburst region of NGC 1068. We developed a comprehensive framework based on state-of-the-art models that incorporate both hadronic and leptonic processes, motivated by the evidence for neutrino emission and the possibility of cosmic-ray acceleration in the starburst environment. As part of this work, we performed an exploration of the parameter space, testing the impact of each free parameter on the total spectral energy distribution (SED), which includes synchrotron, bremsstrahlung, inverse-Compton, and pion-decay components, as well as the absorbed pion-decay contribution. By comparing these model predictions with the multi-wavelength and multi-messenger data, combining the upper limits derived from LST-1 with archival observations from the literature, we identified a set of physically consistent parameters capable of reproducing the observed SED well. This final model provides a scenario in which the observed emission can be explained within the framework of cosmic-ray acceleration in the starburst region of NGC 1068.
By combining observational and theoretical approaches, my study provides new constraints on the very-high-energy emission of NGC 1068 and contributes to the broader effort of understanding the mechanisms potentially powering high-energy neutrino sources. Our results also demonstrate the potential of next-generation observatories, such as CTAO, to revolutionize our view of active galaxies, offering higher sensitivity and extended energy coverage. These future facilities will be decisive in closing the existing observational gaps and in unveiling the nature of the extreme particle accelerators operating in nearby AGN-starburst systems like NGC 1068, as well as many other kinds of objects characterized by gamma-ray emission.

Contents

1 Astrophysical background

This chapter provides a general theoretical introduction to the astrophysical context of this work. It aims to offer an overview of the studied source, outlining its main components and the physical mechanisms that characterize it. The chapter begins by presenting the motivation and framework for this study, which focuses primarily on the analysis of the gamma-ray emission. Subsequently, the general structure of the system is discussed, emphasizing its two principal components: the Active Galactic Nucleus and the surrounding starburst region. Finally, particular attention is given to the source under investigation, NGC 1068, whose peculiar properties are examined through a multimessenger perspective, highlighting the distinctive features of its emission across different energy bands.

1.1 Introduction

For around 13 years, the IceCube Neutrino Observatory, a cubic-kilometer-scale detector located at the South Pole and designed to explore the high-energy universe, has been continuously observing a diffuse flux of high-energy neutrinos, massless subatomic particles that interact only via the weak nuclear force and gravity. These astronomical messengers provide a unique window into the most energetic and extreme environments in the cosmos, such as active galactic nuclei (AGN), gamma-ray bursts (GRBs), and star-forming galaxies, where cosmic rays (CRs) are accelerated to ultra-high energies.
Neutrinos are primarily produced in hadronic interactions, where collisions between high-energy protons and ambient matter or radiation fields give rise to pions, which subsequently decay into gamma rays and neutrinos. Although gamma rays can also originate from purely leptonic processes, neutrinos are exclusively produced by hadronic reactions (Kelner et al., 2006). Consequently, a simultaneous emission of neutrinos and gamma rays is generally expected, linking the two as complementary messengers of cosmic-ray interactions (Abbasi et al., 2025).
Hence, because of the close physical connection between gamma rays and neutrinos, it is crucial to investigate the gamma-ray spectrum in detail to gain deeper insight into the nature of the particle acceleration mechanisms and to identify potential astrophysical sources responsible for the observed neutrino flux.
My work focuses on the detailed study on the gamma-ray emission from a particular galaxy named NGC 1068 that have been identified as an AGN-starburst composite system (e.g., Eichmann et al., 2022). Such systems are of particular interest because they combine two powerful energy-producing environments: an AGN, driven by accretion onto a supermassive black hole, and an intense star-forming (starburst) region, where frequent supernova explosions and stellar winds can efficiently accelerate cosmic rays.
The main physical mechanisms associated with the AGN and starburst regions are discussed in detail in Sections 1.2 and 1.3, respectively.
The overall structure of the system is illustrated in Figure 1. At the center lies the AGN, constituted of several components. The central supermassive black hole acts as the engine of the system, accreting surrounding matter. The material around forms an accretion disk, heated to extreme temperatures around T$\sim 10^5$ K. Above the disk resides the corona, a hot, compact, and still poorly understood region, which is believed to be one of the potential sites for high-energy neutrino production. Surrounding the central engine is the dusty torus, a thick, obscuring structure of gas and dust that reprocesses

the radiation emitted from the inner regions and determines the observed characteristics of the AGN depending on the viewing angle. Because of its particular inclination with respect to the Earth, NGC 1068 has been classified as a Seyfert Galaxy, meaning that the observers' eyesight is aligned with its dusty torus.
Beyond the central nucleus lies the starburst region, where intense star formation activity leads to frequent supernova explosions and strong stellar winds. These processes inject large amounts of energy into the interstellar medium, driving shocks responsible for the cosmic rays acceleration. The interaction between the AGN and the starburst region, as represented in Figure 1, plays a crucial role in shaping the multiwavelength and multimessenger emission properties of the galaxy, which will be further discussed in Section 1.4.1.

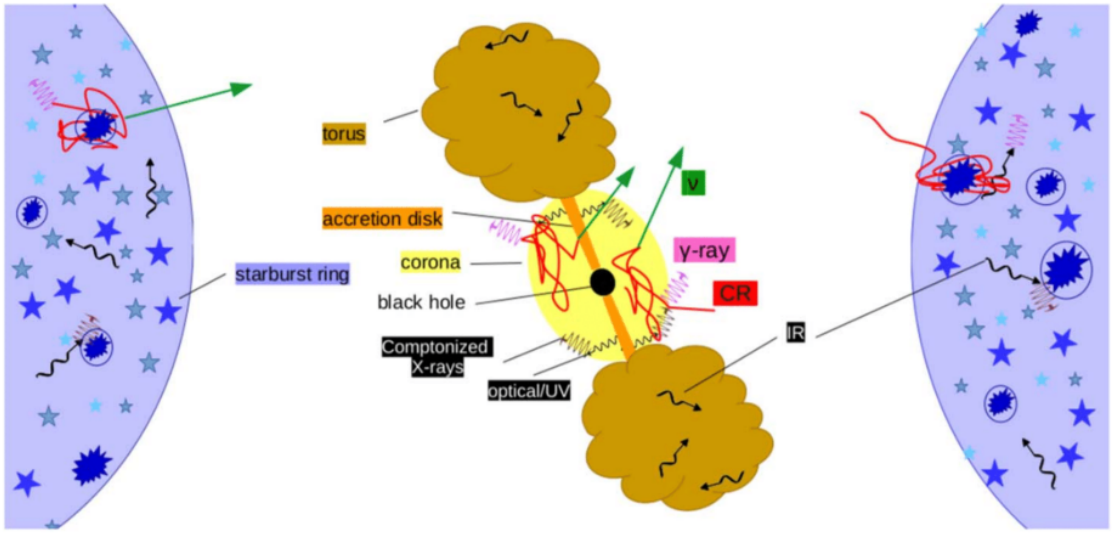

Figure 1: Schematic representation of the two-zone AGN–starburst model for NGC 1068. The central AGN comprises a black hole, accretion disk, coronal region, and surrounding dusty torus, producing radiation across multiple wavelengths (optical/UV, X-rays, γ-rays, and infrared). The corona emits high-energy γ-rays, X-rays and CRs, which can escape into the surrounding medium. At a larger scale (around 1 kpc), a starburst ring hosts intense star formation and supernova activity, contributing additional cosmic rays and high-energy emission. The arrows indicate particle and photon propagation between the AGN core and the starburst regions (Eichmann et al., 2022).

1.2 Active Galactic Nuclei

The term AGN, refers to extremely energetic processes undergoing in the very central regions of certain galaxies, which are not attributed to stars. The source of the AGN luminosity is the gravitational potential energy of supermassive black holes (e.g., Urry and Padovani, 1995).
According to the unified model presented in e.g. Urry and Padovani (1995) and displayed in Figure 2, matter pulled towards the center is collected in an accretion disk around the black hole and experiences viscous or turbulent processes that lead to angular momentum loss. The disk can be observed at ultraviolet wavelengths for certain types of AGN, when the obscuring material does not intercept the line of sight. Emission at hard X-rays is also present but near the black hole, possibly due to the hot electrons (T$\sim 10^{8-9}K$) above the disk, due to inverse Compton scattering (see Section 1.4.1).

Near the disk there are dense, rapidly moving clouds of gas (the broad-line region,

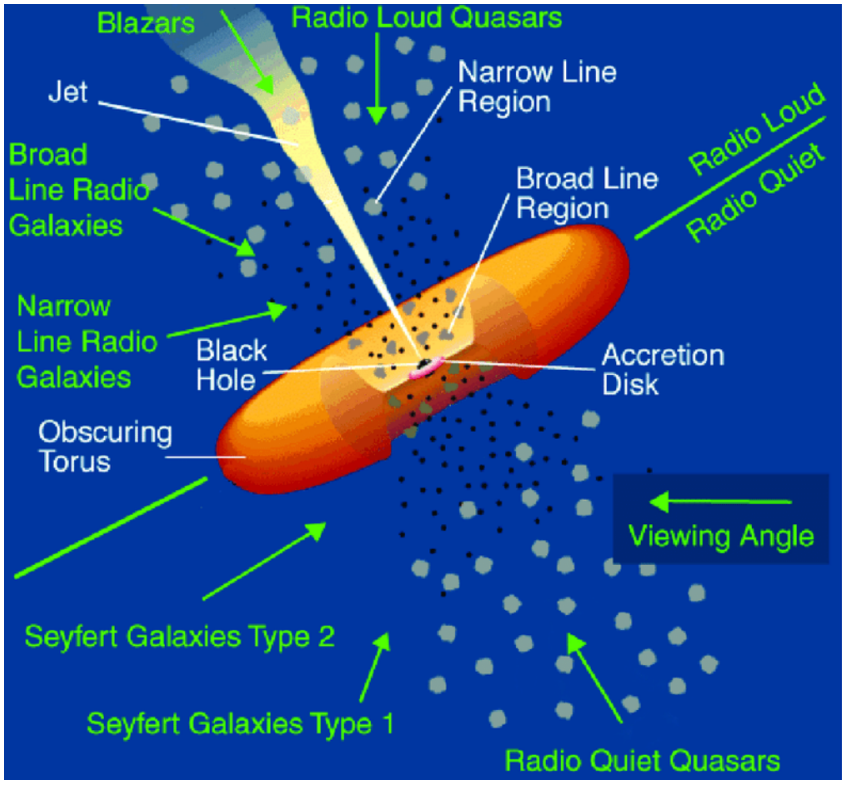

Figure 2: Unified model of AGN. The central supermassive black hole is surrounded by an accretion disk and an obscuring dusty torus, with broad-line and narrow-line regions located at different distances from the core. The observed AGN type depends primarily on the viewing angle: when viewed face-on, the nucleus and jet are visible as blazars or radio-loud quasars, while edge-on views, obscured by the torus, appear as Seyfert type 2 or radio galaxies. The population of jetted AGN corresponds only to 10-15% of the entire population.
Intermediate orientations give rise to Seyfert type 1 and radio-quiet quasars, illustrating how geometry and orientation unify different AGN classifications (Reynolds et al., 2014).

BLR) orbiting close to the supermassive black hole, responsible for strong optical and UV broad emission lines that can be obscured along some lines of sight by a surrounding torus; beyond this structure lies the narrow-line region (NLR), formed by more extended and less dense clouds ionized either by the central continuum or by jet-driven shocks. A fraction of around 10-15% of the entire AGN population presents some outflows of energetic particles that escape along the poles and form collimated radio-emitting jets and eventually some radio sources (prominent for elliptical hosting galaxies, weak when the host is a gas-rich spiral). The plasma present in the jets streams outward at extremely high velocities, producing relativistic beamed radiation (Urry and Padovani, 1995).
For this reason AGN be distinguished as jetted versus non-jetted, depending on the presence or lack of strong relativistic jets, a characteristic can be quantified through radio observations (further discussed in Section 1.2.1. Jetted AGN are the minority of the population, while non-jetted AGN constitute the remaining 85-90% (Padovani et al., 2017).
AGN present axisymmetry, which implies a different appearance, hence a different AGN's class, based on the different observation angle of the object (Figure 2).

1.2.1 Properties and classification

The whole AGN taxonomy can be conveniently visualized in the diagram in Fig. 3. AGN

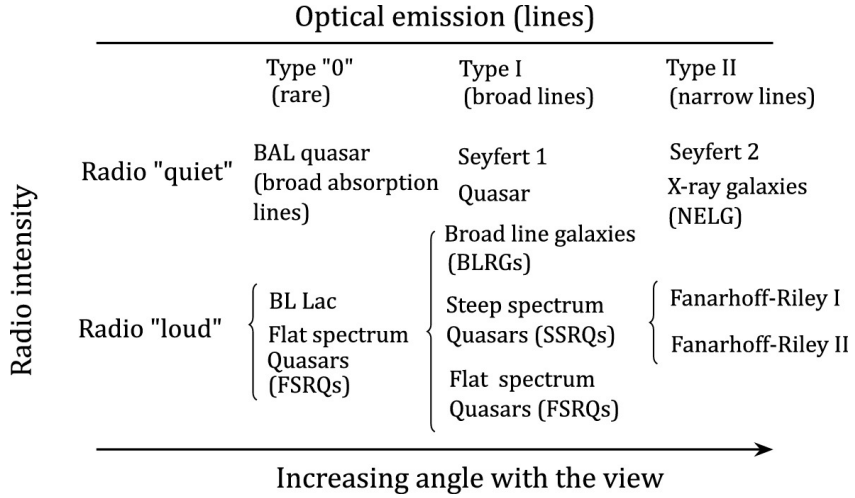

Figure 3: Unified classification diagram of AGN showing the relationship between optical emission-line properties, radio intensity, and viewing angle. The diagram distinguishes between radio-quiet and radio-loud AGN, further categorized by optical emission line types (Type 0, Type I, and Type II). Radio-loud AGN include BL Lac objects, flat- and steep-spectrum quasars (FSRQs, SSRQs), and Fanaroff–Riley (FR I and FR II) radio galaxies, while radio-quiet AGN include Seyfert 1 and 2 galaxies, quasars, and X-ray narrow-line galaxies (NELG). The horizontal axis represents increasing viewing angle with respect to the AGN jet axis, illustrating orientation-based unification (Horvath, 2022).

are firstly classified based on based on the ratio of radio flux at 5 GHz (F_{radio}) versus the optical (B-band) flux (F_{optical}). If the ratio $\frac{F_{\text{radio}}}{F_{\text{optical}}} \gtrsim 10$, then the object is classified as radio-loud. Due to the fact that the emission-line spectra and the continuum of radio-quiet and radio-loud objects exhibit strong similarities, this distinction is thought to depend on the host galaxy or the black hole spin, responsible to enable the formation of powerful relativistic jets that are mainly responsible for the radio emission, as we mentioned in Section 1.2.
According to Padovani et al. (2017), the radio-loud AGN are also jetted as the majority of their emission is non-thermal, hence associated with the presence of powerful relativistic jets. On the other hand, radio-quiet AGN are non-jetted as they are dominated by thermal emission related to the accretion disk.
AGN can also be classified based on the optical and ultraviolet spectra, defining three subclasses depending on the value of the Full Width at Half Maximum (FWHM) defined as the width of a spectrum curve measured between those points on the y-axis which are half the maximum amplitude:

- **Type 1:** characterized by broad emission lines (FWHM $>$ 1500 km/s) and bright continua.
  In the radio-quiet category, low-luminosity sources (historically referred to those objects with absolute magnitude $M_B > -23$) with a resolved host galaxy are identified as Seyfert 1 galaxies, whereas high-luminosity ($M_B < -23$) objects are classified as Quasar, which are typically observed at larger distances and often lack a clearly resolved host galaxy. In the radio-loud category, low luminosity sources are

referred to as Broad-Line Radio Galaxies (BLRG), while high-luminosity sources are classified as Steep Spectrum Radio Quasars (SSRQ) and Flat Spectrum Radio Quasars (FSRQ) according to their continuum spectral shape.

- **Type 2:** exhibit narrow emission lines (FWHM < 1000 km/s) and weak continua, a feature generally attributed to obscuration along the line of sight. In the radio-quiet class, low-luminosity sources include Seyfert 2 galaxies and narrow-emission-line X-ray galaxies (NELG). In the radio-loud class, they are known as Narrow-Line Radio Galaxies (NLRG) and are further distinguished into Fanaroff–Riley type I (FR I) sources, which are of lower luminosity and frequently display symmetric radio jets, and Fanaroff–Riley type II (FR II) sources, which are more luminous and exhibit collimated jets terminating in well-defined lobes and hot spots.

- **Type 0:** AGN with intermediate or mixed spectral properties, typically observed at very small inclination angles (close to 0°). It includes Broad Absorption Lines (BAL) quasars for the radio-quiet class, and BL Lacertae (BL Lac) objects (featureless spectra) and Flat Spectrum Radio Quasars (FSRQ) for the radio-loud class.

As our object of study is specifically a Seyfert galaxy, this class of AGN deserves particular attention, and we will expand on it in the following subsection.

1.2.2 Seyfert Galaxies

Seyfert galaxies did not attract significant attention until the mid-20th century, when their radio emission was recognized. Pioneering studies by Woltjer in 1959 (Peterson, 1997) demonstrated that Seyferts lacked spatially resolved nuclei, with sizes constrained to scales $\lesssim 100$ pc. He further estimated the lifetimes of the AGN activity corresponding to $\sim 10^8$ years, noting their rarity (around 1% of spiral galaxies), and through simple virial arguments, inferred the presence of compact masses in the range of $10^{9\pm1} M_\odot$ at their centers. These results proved that Seyfert galaxies must contain extraordinarily energetic engines confined to very small volumes, starting point for the modern paradigm of accreting supermassive black holes (SMBHs).
Within the radio-loud classification, Seyfert galaxies are recognized today as one of the two major AGN subclasses, accounting for about 10% of all galaxies (Maiolino and Rieke, 1995). By definition, Seyferts host a luminous non-stellar nucleus (Rigopoulou et al., 1997), often coinciding with circumnuclear starburst activity (Whittle, 1992). They are typically associated with nuclear jets (Hummel et al., 1983; De Grijp et al., 1985), visible in the radio or optical, which help distinguish them from pure starburst galaxies. Spectroscopically, Seyferts are divided into type 1 and type 2: type 1 nuclei show both broad emission lines (FWHM $\lesssim 10^4$ km s^{-1}) and narrow lines ($\sim 10^2$ km s^{-1}), while type 2 systems reveal only the narrow components. As already introduced in Section 1.2, the BLR is understood to arise from the orbiting dense ($n_{gas} \sim 10^9$cm^{-3}) close to the SMBH, while the NLR originates in more extended and less dense ($n_{gas} \sim 10^{3-6}$cm^{-3}) clouds ionized directly by the central continuum or through jet-driven shocks (Dopita, 1995). According to the unified models, these spectral differences are attributed to orientation effects: the optically thick and dusty torus surrounding the nucleus obscures the BLR in type 2 objects, while type 1 Seyferts offer a direct view of both regions (Antonucci, 1993). Intermediate types (1.5, 1.8, 1.9) reflect partial obscuration or variations in line strengths (Osterbrock, 1991).

When considering more advanced evolutionary stages, beyond the orientation of the obscuring structure relative to Earth, there is evidence suggesting that type 1 Seyferts may generally be more evolved than type 2 (Oliva et al., 1995).
The huge amount of energy produced by Seyfert nuclei, are most consistently explained by accretion of gas onto SMBHs ($M \gtrsim 10^6\ M_\odot$), with radiative efficiencies surpassing by ~ 10 times that of nuclear fusion ($\epsilon = 0.007$). Evidence for such central masses has been established through observations of extragalactic H_2O mega-masers, which reveal Keplerian rotation curves in circumnuclear disks and yield precise black hole mass measurements (Nakai et al., 1993, 1995).

1.3 Starburst region

Observations carried out by Le Floc'h et al. (2001) show that the circumnuclear starburst region of starburst galaxies forms a prominent ring at a radius of roughly one kiloparsec from the nucleus and constitutes one of the most luminous and active sites of star formation in galaxies like our source, presented in detail in Section 1.4 . These observations were performed with the Infrared Space Observatory Camera and have shown that this structure is dominated by strong Unidentified Infrared Bands (UIBs), interpreted as emission from polycyclic aromatic hydrocarbons (PAHs) excited in the photodissociation regions around young, massive stars, and these features are entirely absent from the nucleus itself, where the harsh radiation field of the AGN efficiently destroys the PAH carriers. The ring is correlated with regions of molecular gas and cold dust traced by CO(1–0) and submillimeter observations. In the same region, we observe gas inflows that trigger shocks and subsequently ignite episodes of intense star formation. Within the ring, the mid-infrared spectra are characterized by strong PAHs at 6.2, 7.7, 8.6, and 11.3 μm, a rising continuum beyond 10 μm attributed to dust grains heated by ultraviolet photons from hot stars, and low-ionization lines such as [Ne II] at 12.8 μm that trace the surrounding ionized gas, all of which are typical signatures of starburst activity.
Energetically, the contribution of the starburst region is substantial: although the AGN dominates the hot continuum in the mid-infrared, the circumnuclear ring accounts for the majority of the UIB emission and provides a major fraction of the far-infrared and submillimeter luminosity through its association with the cold dust component.
As discussed in Eichmann et al. (2021), starburst galaxies are characterized by exceptionally high star-formation rates (SFRs), which lead to the acceleration of cosmic rays through different mechanisms: one is the presence of a large number of supernova remnants, the other is the presence of massive star winds, both strictly connected to the SFR. The associated CRs produce non-thermal emission spanning a broad range of energies, as revealed by multiwavelength observations. Since the first *Fermi*-LAT detections, starburst galaxies have emerged as significant γ-ray sources. Multiwavelength observations reveal that in some starburst galaxies, the central region dominates the non-thermal emission, in combination with an AGN, forming AGN-starburst composites. These AGN–starburst composite galaxies show that the starburst region contributes significantly to gamma-ray emission, although it alone may not account for the total emission (Eichmann et al., 2021). The dense interstellar medium and strong magnetic fields in starburst regions enhance particle interactions, making them candidate sites for gamma-ray production through CR collisions and potential neutrino emission. In these systems, infrared emission, as explained before, dominates the low-energy spectrum. Observations

of NGC 1068 suggest that multiple emission zones, composed by the starburst region and the AGN corona, are required to explain the multimessenger signals.
Based on a previous work carried out by Ackermann et al. (2012), Kornecki et al. (2020) reported that observations of nearly a dozen star-forming galaxies in γ-rays by *Fermi*-LAT have revealed a quasi-linear relation between γ-ray luminosity and SFR. This correlation supports a scenario in which GeV emission is dominated by hadronic interactions of CRs with interstellar protons, producing photons via neutral pion decay. Since CRs are predominantly generated by supernova remnants, galaxies with higher SFRs host higher CR energy densities and are therefore more luminous in γ-rays. In their population study, it was established that the gamma-ray luminosity of star-forming galaxies scales with the SFR more steeply than previously thought. This result implies that galaxies experiencing extreme starburst activity, characterized by compact, dusty, and gas-rich environments, are more efficient gamma-ray emitters compared to normal spirals. The mechanism is linked to the formation of massive stars, which rapidly evolve into supernovae that inject large populations of cosmic rays into the interstellar medium. Unlike in lower-SFR galaxies, where cosmic ray escape through galactic winds or diffusion reduces radiative efficiency, in starbursts the combination of high gas densities, short cooling timescales, and turbulent magnetic fields makes them nearly perfect calorimeters, with the majority of cosmic ray energy radiated away before escape.

1.4 NGC 1068

NGC 1068 is a nearby (redshift $z = 0.003$) galaxy that exhibits both the energetic signatures of an active galactic nucleus (AGN) and intense star-forming activity. This dual nature classifies it as an AGN–starburst composite galaxy.
NGC 1068, classified as a Seyfert 2 galaxy (a specific kind of AGN which was discussed in Section 1.2.2) in the unified model of AGN (Antonucci, 1993), played a fundamental role in understanding the physics and evolution of this class of objects. The galaxy first appeared in the literature as early as 1908, when E. A. Fath at Lick Observatory (California, USA) obtained the first optical spectrum, revealing prominent emission lines (Peterson, 1997). Shortly thereafter, V. M. Slipher at Lowell Observatory (Arizona, USA) refined these results, resolving the emission features and measuring their velocity widths, on the order of hundreds of $\mathrm{km\,s^{-1}}$. The systematic study of such phenomena began in 1943, when Carl Seyfert identified a class of galaxies with intensely bright nuclei and, in some cases, extremely broad emission lines. Although NGC 1068 was included in his sample, it is a Type 2 Seyfert, and its broad-line region was not observed directly but revealed decades later through spectropolarimetry.
Several components can be distinguished in different energy bands: (1) a starburst region in the spiral arms of the host galaxy; (2) a jet of kiloparsec size; (3) a sub-kiloparsec scale outflow; (4) the black hole surroundings (Padovani et al., 2024). Those components can be studied in different energy bands, offering a complementary description to the whole picture. However, none of the components mentioned before can be resolved in γ-rays, and the origin of this emission has not yet been disentangled (Padovani et al., 2024).
There are several reasons why an in-depth study of this source is crucial. A decade of data from the IceCube Neutrino Observatory (Collaboration et al., 2022; Abbasi et al., 2025) has claimed NGC 1068 as a possible neutrino emitter, with an observed TeV excess located $\sim 0.35^\circ$ from the galaxy's position, with a significance of 4.2σ inconsistent with

background expectations. The peculiarity of this source is that the gamma-ray emission should be of the same order of magnitude of the neutrino emission, but in this case we have no corresponding gamma-ray emission at similar energies. As noted by Eichmann et al. (2022), both the AGN and the circumnuclear starburst could be potential sites for the production of highly energetic CRs, potentially contributing to the observed extragalactic CR component. Observations with the *Fermi*-LAT and imaging atmospheric Cherenkov telescopes such as VERITAS have detected γ-ray emission from the galaxy, confirming that particles are being accelerated to very high energies, a central focus of this work.
To disentangle the active emission mechanisms, it is essential to distinguish between the various particle acceleration sites. For NGC 1068, numerous observations suggest the presence of multiple acceleration regions, implying that its multimessenger emission requires a multi-zone modeling approach to achieve a consistent interpretation. In Figure 1, adapted from Eichmann et al. (2022), a schematic view of such a multi-zone model is shown, illustrating the main components contributing to the observed signals.

1.4.1 Multimessenger view

In order to have a better overview of the different undergoing phenomena in NGC 1068, it is crucial to adopt a multimessenger view.
Here we will brifely explain the ongoing processes at different wavebands, and how these could be responsible for the observed (but also hidden) emission. In the review by Padovani et al. (2024), the multimessenger SED is presented (see Fig. 4), where several key features can be identified: the radio spectrum (with $L \propto \nu^{-0.7}$), the emission from the spiral host galaxy, the contributions from the accretion disk and corona, the gamma-ray regime (with data from Fermi-LAT and MAGIC), and the neutrino detection band (IceCube Observatory).

Radio band
Radio observations are used to investigate the inner region of NGC 1068, shown in Figure 5. The observations show the presence of a starburst disk region of about 2 kpc size and the presence of a 500-pc scale jet. The jet itself is quite small and the velocities are quite low (almost two orders of magnitude shorter and much slower than M87 jet, $< 0.005c$ versus $> 0.99c$, which leads to classify NGC 1068 as a non-jetted AGN (Padovani et al., 2024). The shape of the radio continuum in Figure 4 indicates synchrotron emission, the origin of which could be linked both to the starburst region and the jets.

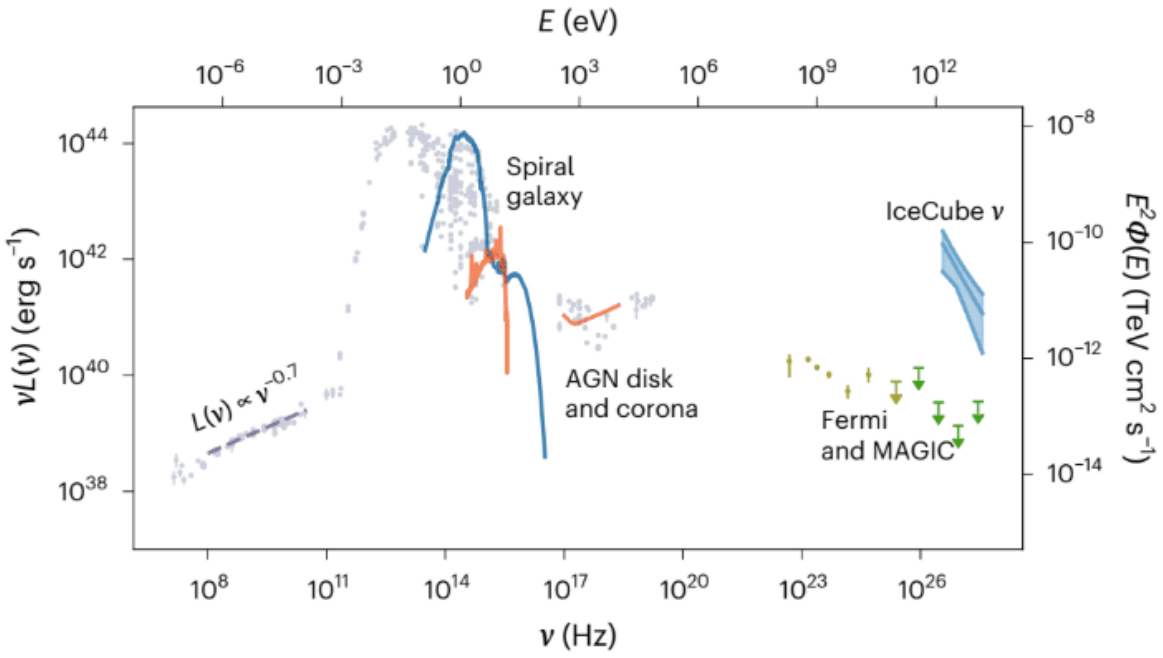

Figure 4: The spectral energy distribution of NGC 1068 illustrates the power emitted at different frequencies or energies. The units are as follows: frequency ν in Hz (bottom x-axis), energy E in eV (top x-axis), power νL in erg s^{-1} (left y-axis), and flux $E^2\Phi(E)$ in TeV cm^{-2} s^{-1} (right y-axis) (Padovani et al., 2024).

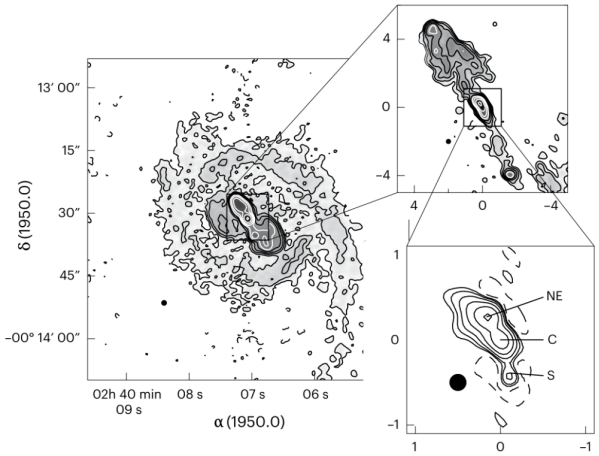

Figure 5: Image of NGC 1068 at 1.7 GHz. In the left panel it is shown the starburst (SB) disk (right ascension (α) and declination (δ) are given for the 1950 epoch). In the top right panel there is the radio jet. In the bottom right panel the central core is represented, where NE, C, and S indicate three distinct radio components. In the two right-hand panels, the axes show offsets from component C in arcseconds; each arcsecond corresponds to 48.9 pc (Padovani et al., 2024).

Sub - millimetre band

AGN not only accrete matter to feed their central supermassive black holes but also drive large-scale outflows and winds of matter. These outflows, which are generally less collimated and slower than relativistic jets (Padovani et al., 2024), play a crucial role

in galaxy evolution through the AGN feedback mechanism (e.g., Fabian, 2012). Such feedback can regulate or even quench star formation by expelling or heating the interstellar medium (ISM), and may eventually starve the AGN itself by removing its supply of infalling gas.
AGN-driven outflows may have different temperatures, compositions, and ionization states, including ionized, atomic, and molecular components. These outflow phases span over a broad range of velocities, from semi-relativistic speeds of $\sim 10^5\,\mathrm{km\,s^{-1}}$ for ultra-fast outflows (UFOs), to $\sim 10^2\,\mathrm{km\,s^{-1}}$ for warm absorbers, observed on spatial scales from sub-parsec to kiloparsec distances for the molecular component, as illustrated in the work of Cicone et al. (2018). For what concerns the ionized component, there are studies like e.g. Kubo et al. (2022) that show the detection of outflows in this state with velocities around $\sim 10^3\,\mathrm{km\,s^{-1}}$.
Most of the molecular gas in the ISM exists in the form of molecular hydrogen (H_2), which is invisible in the cold ISM where most of the molecular mass resides. Because H_2 transitions are only excited in warm regions accessible to infrared or ultraviolet observations, sub-millimetre studies rely on other tracers. The second most abundant molecule, CO, is the best tracer of the global molecular reservoir at these wavelengths. Currently, the Atacama Large Millimeter/submillimeter Array (ALMA) represents the most powerful tool for probing this molecular component.
A huge molecular outflow in NGC 1068 has been revealed by ALMA observations (Padovani et al., 2024), with molecular tracers such as CO and hydrogen cyanide (HCN) indicating strong AGN feedback activity. This outflow also induces molecular shocks within the circumnuclear disk, on scales of a few hundred parsecs (Viti et al., 2014; Huang et al., 2022).

Mid-IR band
The interferometer GRAVITY (Pfuhl et al., 2020) and the spectroscopic instrument MATISSE (Gámez Rosas et al., 2022) observed the presence of a dusty torus surrounding the accretion disk and located within the circumnuclear disk of a dimension of ~ 0.2pc, which is typical of Seyfert objects. In NGC 1068, the torus blocks the view of the inner regions, adding another layer of difficulty in studying this source.
The inner accretion disk is thought to have a temperature around 10^{4-6} K , with an emission in the optical/UV band, where dust absorption is particularly effective. The absorbed radiation is subsequently reprocessed by nearby dust grains and re-emitted in the mid-IR range. In this region, for column densities exceeding $N_{\mathrm{H}} > 10^{24}\,\mathrm{cm^{-2}}$, even hard X-ray photons become strongly attenuated.
The geometry of the torus remains under active investigation. Observational and theoretical studies suggest a complex, clumpy morphology rather than the originally assumed homogeneous, doughnut-like structure (Almeida et al., 2009; Markowitz et al., 2014; Marinucci et al., 2015).

X-ray band
X-ray observations are essential, as this radiation can penetrate large column densities of gas and dust that obscure the central regions of active galaxies. For this reason, they can offer a complementary vision to the IR regime.
The X-ray emission of AGN is believed to originate in the corona, a plasma of extremely hot electrons at temperatures of about 10^{8-9} K, which surrounds the accretion disk. In this region, ultraviolet photons emitted from the disk are up-scattered by the hot

electrons through the inverse Compton process, producing X-rays (Liang, 1979; Padovani et al., 2017, 2024).
These coronal X-ray photons can also interact with protons of energies around 100 TeV, triggering photomeson production and giving rise to 1-10 TeV neutrinos, such as those observed by the IceCube Neutrino Observatory (Padovani et al., 2024). Remarkably, NGC 1068 stands out as one of the X-ray brightest AGN in the sky (Marinucci et al., 2015; Ricci et al., 2017), making it a prime candidate for studying the link between high-energy photon and neutrino emission.

Gamma-ray band
This band has been observed by Fermi-LAT and MAGIC, and is currently observed by LST-1. The γ-ray emission has been associated mainly due to star formation activity, that leads to cosmic rays acceleration and consequent emission of photons in this energy range.
Most of the emission is associated with hadronic processes, like p-p collisions and pion decay, which will be described in depth in the Section 4.1.
The reason why the emission of γ-rays is believed to come principally from star-forming regions is that it has been reported a lack of variability in the process over 10 years of observations (Ajello et al., 2020). Other contributors (like jets, matter outflows) are not excluded, but are thought to be negligible(Padovani et al., 2024).

TeV neutrino band
Using 13.1 years of IceCube data, the analysis has revealed significant neutrino emission from the Seyfert galaxy NGC 1068, establishing it as the most prominent neutrino source among 110 preselected γ-ray emitters, defined a priori and located in a declination range covering the northern sky, $-3^\circ < \delta < 81^\circ$ (Ballet et al., 2020).
The detected flux exceeds its γ-ray counterpart by at least two orders of magnitude. The derived neutrino energy spectrum is well described by a power law with a spectral index of $\Gamma = 3.4 \pm 0.2$ (Abbasi et al., 2025), consistent with earlier analyses based on 9–10 years of data. The best-fit muon–neutrino flux normalization at 1 TeV is $\Phi^{\nu_\mu+\bar{\nu}_\mu}_{1\,\mathrm{TeV}} = 4.7^{+1.1}_{-1.3} \times 10^{-11}\,\mathrm{TeV}^{-1}\,\mathrm{cm}^{-2}\,\mathrm{s}^{-1}$ (Abbasi et al., 2025), corresponding to an all-flavor isotropic neutrino luminosity of $L_\nu = 10^{42.1\pm0.2}\,\mathrm{erg\,s}^{-1}$ in the 1.5–15 TeV range.
High-energy neutrinos are produced in the decay of charged pions, which result from hadronic (p–p) and photo-hadronic (p–γ) interactions between cosmic rays and ambient matter or radiation fields. The charged pion decay chain,

$$\pi^\pm \to \mu^\pm + \nu_\mu(\bar{\nu}_\mu), \qquad \mu^\pm \to e^\pm + \nu_e(\bar{\nu}_e) + \bar{\nu}_\mu(\nu_\mu), \tag{1}$$

produces electrons (or positrons) and neutrinos of multiple flavors, while neutral pions decay into two γ-ray photons, $\pi^0 \to \gamma + \gamma$. Because charged and neutral pions are produced in comparable amounts, a neutrino flux from astrophysical sources is inevitably accompanied by γ-ray emission with a comparable energy distribution, approximately following $F_\gamma \simeq 2F_\nu$ and $E_\gamma \simeq 2E_\nu$ (Berezinskii et al., 1984; Gaisser et al., 2016). The spectral energy distribution of NGC 1068 is represented in Figure 4.

2 Gamma-ray astronomy

The gamma-ray region of the electromagnetic spectrum spans photons with energies between 100 keV up to the PeV range. These extremely energetic photons cannot be explained by the thermal emission processes, particularly above the MeV energy range. Instead, their production requires non-thermal mechanisms, produced by particles that are accelerated to ultrarelativistic energies in extreme environments.
A wide variety of sources contribute to the gamma-ray sky. Within our Galaxy, we observe a diffuse, steady emission along the Galactic plane, as well as numerous discrete sources including pulsars, Pulsar Wind Nebulae (PWNe), Supernova Remnants (SNRs), novae, and binary systems. On extragalactic scales, the major contributors are AGN, Starburst (SB) Galaxies and Gamma-Ray Bursts (GRBs).
In this chapter, based on the work of Mas Aguilar (2025), we introduce the fundamental concepts of gamma-ray astronomy and provide a concise overview of its current state. We then describe the instruments relevant to this work. First, we present LST-1, part of the CTAO, for which we performed the full data reduction and analysis. Next, we discuss Fermi-LAT, whose data used were taken from existing catalogs, as well as the MAGIC and VLA, whose observations were gathered from the literature. Moreover, we summarize the characteristics of COSI, used in this study to compare its sensitivity (also taken from the literature) with our model, in Section 5.3, in order to give some predictive results.

2.1 Overview

The electromagnetic spectrum spans more than 20 orders of magnitude in frequency, yet only a very narrow band, corresponding to visible light, can be directly detected by the human eye. Visible radiation carries photon energies of just a few electronvolts (eV), followed by the Ultraviolet (UV) range extending up to ∼100 eV, beyond which radiation becomes ionizing and is fully absorbed by Earth's atmosphere. At higher energies, X-rays span from about 100 eV to 100 keV, divided into soft (around 100 eV–10 keV) and hard (around 10 keV–100 keV) components with distinct origins and properties. Photons above typically 100 keV are classified as gamma rays, the most energetic form of electromagnetic radiation in the Universe, from 100 keV up to several hundred PeV.
To account for this vast range, in the gamma-ray community we usually divide the gamma-ray window into several domains: Low Energy (LE, < 100 MeV), High Energy (HE, 100 MeV–100 GeV), Very High Energy (VHE, 100 GeV–100 TeV), Ultra High Energy (UHE, 100 TeV–100 PeV), and Extreme High Energy (EHE, > 100 PeV). Each of these regimes is associated with distinct interactions with matter, requiring different detection strategies and revealing specific classes of astrophysical sources.
Closely related to gamma-ray studies are CRs, high-energy particles of extraterrestrial origin that constantly bombard Earth (mainly protons and some heavier nuclei, plus a smaller fraction of electrons/positrons). Their energy spectrum (shown in Figure 6) spans from $\sim$ GeV to beyond 10^{20} eV, and it exhibits several spectral features: a power-law distribution, defined as $\frac{dN}{dE} \propto E^{-\Gamma}$, with slope $\Gamma \sim 2.7$ up to the knee at 4.5×10^{15} eV, a steepening to $\Gamma \sim 3$ beyond, a hardening around the ankle at 4×10^{18} eV ($\Gamma \sim 2.6$), marking the transition to an extragalactic component, and a strong suppression above 4×10^{20} eV.
Gamma rays are produced in interactions of relativistic particles with matter, radia-

tion fields, or magnetic environments, and propagate through the universe, allowing their sources to be identified. Thus, gamma-ray astrophysics provides information about these cosmic rays. As a result, observations of gamma rays contribute to three major fields of research: first, the determination of the origin of cosmic rays, by linking Galactic CRs to environments such as SNRs and constraining models of extragalactic accelerators beyond the ankle; second, the study of extreme astrophysical environments, where gamma-ray emission traces particle acceleration and relativistic outflows in objects like AGN, GRBs, and pulsars, providing direct information about physical conditions that cannot be probed at lower energies; and third, fundamental physics, where gamma rays serve as tools to test cosmological parameters such as the Hubble constant (Abbott et al., 2017), and investigate the nature of dark matter through indirect searches based on annihilation or decay signatures (Mas Aguilar (2025) and references therein).
Despite these opportunities, gamma-ray astronomy faces significant challenges. One of them is that the photon flux from astrophysical sources decreases sharply with energy, making detections statistically difficult. Another huge challenge is the fact that the Earth's atmosphere is opaque to gamma rays, requiring satellite detectors to access lower energies or indirect ground-based techniques such as Imaging Atmospheric Cherenkov Telescopes (IACTs) to capture the particle showers produced when gamma rays interact with the atmosphere.
As we have already mentioned, gamma-ray radiation originates from non-thermal emission mechanisms. Depending on the nature of the emitting particles, i.e., leptons or hadrons, two primary mechanisms can produce gamma rays. Leptonic processes, where high-energy electrons and positrons are accelerated in magnetic-field-dominated environments, can emit gamma rays through interactions such as synchrotron radiation, inverse Compton scattering or bremsstrahlung. On the other hand, hadronic processes (primarily protons), generate gamma rays through interactions involving high-energy hadrons, with target photons in the interstellar medium (ISM).
Each of these processes will be described in detail in Chapter 4.

2.2 Gamma-ray sources

Gamma-ray emission in the Universe arises from a wide variety of astrophysical objects, which can be broadly classified into Galactic and Extragalactic sources.

- Galactic Sources: within our Galaxy, several types of objects are established gamma-ray emitters. Pulsars are rapidly rotating neutron stars with extremely strong magnetic fields that accelerate electrons and positrons, producing gamma rays via curvature radiation and inverse Compton scattering. Supernova Remnants (SNRs) are expanding shells of gas and plasma left behind after supernova explosions; they are considered key sites for cosmic-ray acceleration, generating gamma rays through both hadronic interactions and leptonic processes. Pulsar Wind Nebulae (PWNe) form when relativistic winds from pulsars interact with surrounding material, creating high-energy emission regions. Other Galactic contributors include dense star clusters and a variety of binary systems, which can also accelerate particles to energies sufficient to emit gamma rays.

- Extragalactic Sources: located beyond the Milky Way, are responsible for some of the most energetic photons detected. Among these, AGN are the most prominent. Starburst galaxies exhibit exceptionally high rates of star formation, leading to

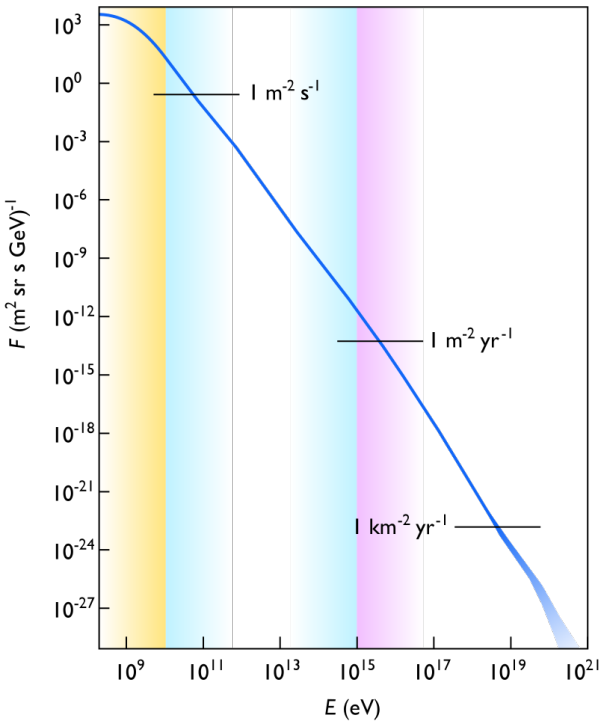

Figure 6: The cosmic ray energy spectrum, extending from approximately 10^9 eV to 10^{21} eV, has been measured through numerous extensive air shower experiments. The spectrum follows an overall power-law behavior but exhibits several distinct features. At around 10^{15} eV and 10^{17} eV, two structures known as the *knees* appear, where the spectrum steepens, indicating a softening of the flux with increasing energy. At higher energies, near 4×10^{18} eV, the spectrum shows another feature called the *ankle*, where it becomes harder again. These features are thought to reflect transitions in the dominant sources (associated to different colors in the plot) or acceleration mechanisms of cosmic rays. Yellow region is corresponds to Solar cosmic rays, blue to Galactic cosmic rays, and purple to extragalactic cosmic rays. As we are studying an extragalactic source, we are mainly interested in the higher end of the spectrum. Every colored region is also associated to Frequency of arrival of cosmic rays at Earth's surface (Vrtilek, 2022).

enhanced cosmic-ray populations and subsequent gamma-ray emission. Another important category is GRBs, brief but powerful flashes of gamma rays, which arise from catastrophic events such as the collapse of massive stars or mergers of compact objects.

2.3 Detection techniques

Gamma-ray astronomy faces unique challenges because the Earth's atmosphere is opaque to high-energy photons, preventing their direct detection from the ground. As a result, space-based telescopes are required to observe these photons. Gamma rays are particularly difficult to focus or reflect using conventional mirrors, which makes their detection more complex than at lower energies. In space telescopes, gamma rays are often detected through the pair-production process, as, for example, by the Fermi Large Area Telescope (Fermi-LAT). However, the combination of low gamma-ray flux and the limited collection area of space instruments reduces their sensitivity above a few tens of TeV, limiting the study of very-high-energy sources.
To overcome this limitation, ground-based gamma-ray astronomy has developed techniques that exploit the secondary particles produced when gamma rays interact with the atmosphere. These methods allow the detection of photons with energies extending up to the PeV range. Among ground-based instruments, IACTs are particularly effective. A notable example is the first Large-Sized Telescope (LST-1), which is the focus of this thesis. As part of the upcoming Cherenkov Telescope Array Observatory (CTAO), LST-1 represents a major advancement in VHE gamma-ray astronomy, offering enhanced sensitivity that is expected to significantly expand our understanding of the gamma-ray Universe in the coming years.

2.4 Space-based Telescopes

Space-based gamma-ray detectors rely on the physical interactions of gamma rays with detector materials resulting, as mentioned before, in low sensitivities above a certain energy threshold. Moreover, gamma-ray instruments must deal with the background of cosmic rays, which can be very similar to gamma-ray signals. Since the interaction processes vary with energy, different types of telescopes have been developed for distinct energy ranges.
One example of space-based telescopes detecting gamma rays are Compton Telescopes, which typically detect energies in the 100 keV to 10 MeV range. These instruments generally consist of two layers: the first, often a liquid scintillator, scatters the incoming gamma ray, while the second, a thick solid scintillator, absorbs the scattered photon (Murdin, 2001). An additional anti-coincidence scintillator typically surrounds the instrument to reduce the cosmic-ray background.
The most successful Compton telescope was COMPTEL (Schonfelder et al., 1993), launched in 1991. Due to limitations in efficiency, Compton telescopes have not been extensively developed in subsequent years. New proposed missions, such as e-ASTROGAM (De Angelis et al., 2018), AMEGO (Kierans, 2020), and the upcoming Compton Spectrometer and Imager (COSI) (Tomsick et al., 2023), aim to improve sensitivity in this energy range and further explore the MeV gamma-ray Universe.
Another kind of space-based telescopes are the pair production telescopes, based on

the detection of the electron-positron pair produced by the interaction of the incident gamma ray inside the detector, and they typically detect energies above 10 MeV. They are usually constituted by a tracker, basically silicon detectors that are able to detect the trajectory of the electron-positron pair; an anti-coincidence detector, that detects charged particles and is able to distinguish them from gamma-rays; a calorimeter, that provides accurate measurements thanks to the absorption of secondary particles at this level (Murdin, 2001). The most well known pair production telescope is Fermi-LAT (e.g., Ballet et al., 2024), which operates in the 30 MeV to 100 GeV (and above) range.

2.4.1 Fermi-LAT

The Fermi Gamma-ray Telescope in Figure 7 is a satellite launched on 2008 by NASA, exploring the 50 MeV - 1 TeV range of energies. It consists of a main instrument, the Large Area Telescope (LAT), and a secondary one, the Gamma-ray Burst Monitor (GMB), which has a larger field of view respect to LAT and provides spectral coverage of gamma-ray bursts.

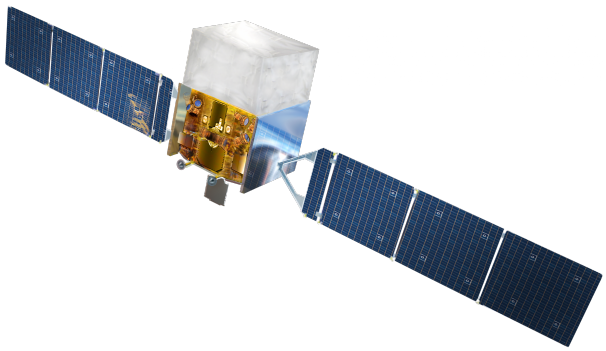

Figure 7: The Fermi Gamma-ray Space Telescope (Fermi-LAT) shown in orbit, with its large solar arrays extended for power. The central spacecraft bus houses the scientific instruments, including the Large Area Telescope (LAT) for detecting high-energy gamma rays from cosmic sources such as black holes, neutron stars, and supernova remnants. The white upper structure shields the instruments, while the golden lower section contains electronics, communication systems, and thermal control hardware (`https://fermi.gsfc.nasa.gov/`).
Source: `https://en.wikipedia.org/wiki/Fermi_Gamma-ray_Space_Telescope`

The mission objectives of the instruments have been related to investigating the high-energy phenomena, including black holes' jets, Dark Matter, solar flares, pulsars, and the origin of cosmic rays.
The LAT surveys the entire sky each day and the data are collected in catalogs. The catalog that has been used for this work is the 4FGL-DR4 (Ballet et al., 2024), which is a summary of 14 years of observations, from 2008 to 2022. It is composed by 7194 sources, all of them having a minimum of 4 sigma significance. Almost all of them (except for 82 sources) are assumed having point like emission. (`https://fermi.gsfc.nasa.gov/`)

2.4.2 MAGIC

The Major Atmospheric Gamma Imaging Cherenkov in Figure 8, also located at Roque de Los Muchachos, La Palma, Canary Islands, Spain, is a system of two IACTs of 17m of

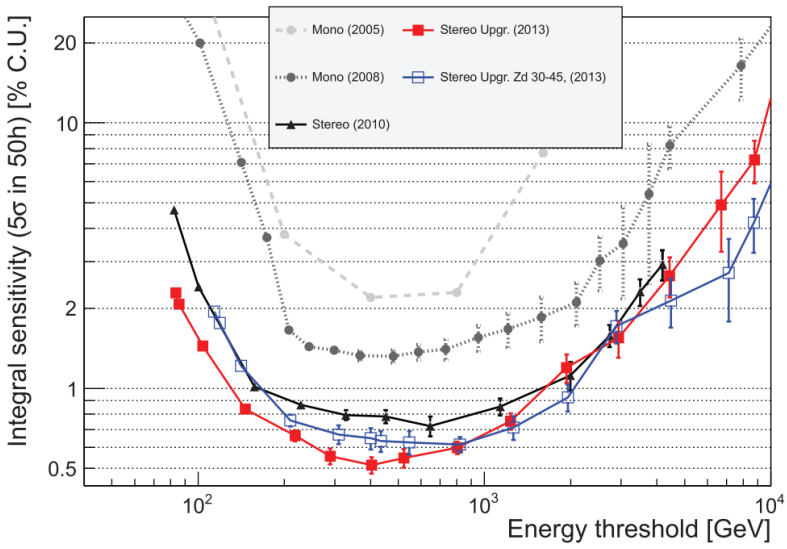

Figure 9: Comparison between integrated sensitivity of Magic-I only and MAGIC in stereo mode, taken from Aleksić et al. (2016).

diameter, and are dedicated to the observation of Galactic and extragalactic sources at VHE, which is currently ran by an international collaboration formed in 1998 consisting of 12 countries.
The main goal of the project was to build an instrument capable of observing in a range of energies traditionally considered as the classical domain of satellite instruments, which is below 100 GeV.
The two telescopes (MAGIC-I and MAGIC-II) usually operate in coincidence, in a so-called stereoscopic mode. Only events that trigger both telescopes are observed and analyzed. Clearly, this mode provided a significant increase of sensitivity compared to the time in which only MAGIC-I was operating (until 2009), as can be visualized in Figure 9. All the information can be found at `https://magic.mpp.mpg.de/`.

Figure 8: The two MAGIC telescopes. Image credits: Daniel Lopez/IAC. Source: `https://magic.mpp.mpg.de`

2.4.3 VLA

The Karl G. Jansky Very Large Array (VLA) in Figure 10 is a centimeter-wavelength radio astronomy observatory located in central New Mexico. It was constructed in the 1970s, and it consists of 28 radio telescopes, each with a 25-meter dish. The antennas are arranged in a Y-shaped configuration and mounted on double parallel railroad tracks, allowing their positions to be adjusted to modify the array's angular resolution and surface brightness sensitivity.
Operating as an interferometer, the VLA combines the signals from its individual antennas to simulate a single, large-aperture telescope. The array's arms extend 21 kilometers each, permitting a range of up to 351 independent baselines and achieving angular resolutions between 0.2 and 0.04 arcseconds. The facility stands at an elevation of 2,120 meters above sea level and is part of the National Radio Astronomy Observatory (NRAO), operated under the National Science Foundation.
Astronomers using the VLA have made significant discoveries, including observations of black holes, protoplanetary disks, magnetic filaments, and complex gas dynamics at the Milky Way's center. The VLA has also contributed to studies of cosmological parameters and the mechanisms behind radio emissions. As a versatile instrument, it supports investigations of radio galaxies, quasars, pulsars, supernova remnants, gamma-ray bursts, radio-emitting stars, the Sun, planets, masers, and hydrogen gas in both the Milky Way and external galaxies (`https://science.nrao.edu/facilities/vla/`). The data used in this work are taken from Wynn-Williams et al. (1985).

Figure 10: Very Large Array - National Radio Astronomy Observatory. Source: `https://public.nrao.edu/telescopes/vla/`

2.4.4 COSI

The acronym COSI stands for Compton Spectrometer and Imager, a NASA satellite mission in development, whose launch is due in 2027.
The wild-field gamma-ray space telescope, shown in Figure 11, is expected to investigate the energy range between 0.2 and 5 MeV. It is going to be a revolutionary instrument, since the low-energy part of the gamma-ray regime (called MeV gap because of the actual lack of data) has been poorly investigated due do observational issues.

This region of the electromagnetic spectrum contains signals of exceptional scientific interest, including nuclear lines from radioactive elements and the electron–positron annihilation line at 0.511 MeV. This region includes emission from accreting black holes, although they can also emit at higher energies, making it an important range for multimessenger astrophysics.
The upcoming COSI satellite mission will target all of these phenomena, with primary scientific goals focused on positrons, nuclear line emission, polarimetric studies of accreting black holes, and multimessenger astrophysics. COSI is a Compton telescope distinguished by its combination of high energy resolution, achieved through cryogenically cooled germanium detectors, and a wide field of view. This design makes it ideal for producing all-Galaxy and all-sky emission-line maps in the MeV range, thereby deepening our understanding of how matter is created and destroyed in our Galaxy (Tomsick et al., 2023).

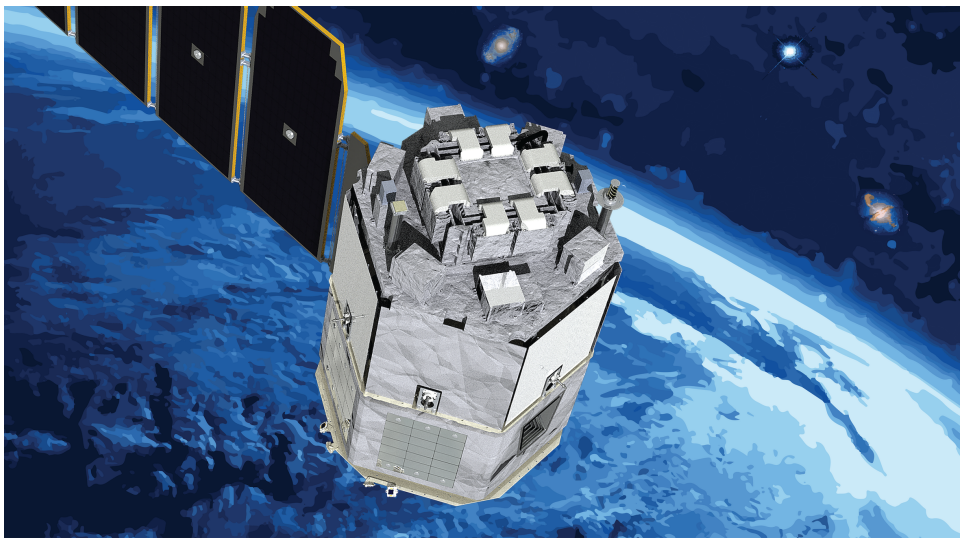

Figure 11: Artistic image of COSI satellite. Source: `https://science.nasa.gov/mission/cosi/`.

2.5 Ground-based Detectors

In order to overcome limitations of space-based telescopes, physicists in the 1960s proposed using the Earth's atmosphere itself as a detector to detect the VHE sky. When a gamma ray enters the atmosphere, it interacts with atmospheric nuclei and is rapidly absorbed, producing a cascade of secondary particles and electromagnetic radiation. This cascade, known as an Extensive Air Shower (EAS), can be detected from the ground as they spread over large effective detection areas. However, cosmic rays and other particles also generate showers that resemble those produced by gamma rays, creating a significant background that is difficult to eliminate.

Extensive Air Showers and Cherenkov Radiation:
When a gamma ray of energy E_0 interacts in the atmosphere, it initiates an electromagnetic cascade of secondary particles, such as electron-positron pair, at an average altitude around 25 km. These leptons subsequently radiate photons via bremsstrahlung, which in turn generate new electron-positron pairs. As each generation of particles carries roughly half the energy of its parent, the cascade continues until the particle energy falls below

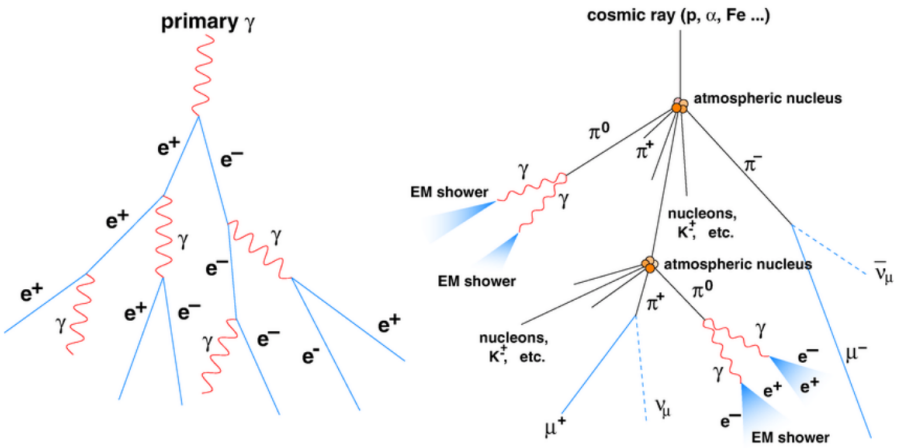

Figure 12: Comparison between the development of an electromagnetic shower generated by a gamma ray on the left, and a cosmic ray on the right (Mas Aguilar, 2025).

a critical value ($E_c \approx 81$ MeV), where ionization losses dominate over bremsstrahlung (Heitler, 1984; Sommers, 2004).
Electromagnetic showers represent only one type of Extensive Air Shower. The vast majority of showers are produced by cosmic rays, mainly protons, colliding with atmospheric nuclei, while only a very small fraction of the showers are produced by a gamma-ray primary particle (the 0.43% of the total for energies above 5.4×10^{16} eV, Fomin et al. (2013)). The hadronic interactions create various mesons, including neutral pions, which decay into photons that subsequently initiate electromagnetic cascades. Charged pions instead decay into muons and neutrinos. While some secondary particles can reach the ground, most of the energy is carried within electromagnetic subshowers. A comparison between a gamma-ray-induced and a hadron-induced shower is shown in Figure 12. In practice, the irregular development of hadronic showers makes them distinguishable in principle, but in reality, separating them from gamma-ray showers is challenging. Hadronic showers therefore constitute the dominant background for ground-based gamma-ray telescopes, and background rejection remains one of the central challenges in VHE astronomy.
A key observable from Extensive Air Showers is Cherenkov radiation (Cherenkov, 1934), generated when a charged particle travels faster than the speed of light in a medium, producing a coherent pulse of light.
The main features that describe Cherenkov light from atmospheric showers are: 1) the Cherenkov cone opening angle is $\sim 1°$, illuminating an area with a radius of about 120 m on the ground at few kilometers of altitude (between 2 km and 10 km); 2) the Cherenkov spectrum peaks around 300–350 nm, in the near-UV range; 3) the duration of Cherenkov pulses is extremely short, lasting only a few nanoseconds; 4) the total Cherenkov light yield is approximately proportional to the energy of the primary gamma ray, making it a useful energy estimator.

Imaging Atmospheric Cherenkov Telescopes (IACTs):
IACT is based on detecting the Cherenkov light produced by secondary particles in atmospheric showers. IACTs employ large parabolic reflectors that collect this faint light and direct it onto multi-pixel cameras. These cameras, typically composed of photomultiplier tubes (PMTs) due to their nanosecond response times and high gain. The resulting image traces the longitudinal development of the shower: gamma-ray-induced

events appear as elongated, elliptical images in the focal plane. From the orientation and geometrical parameters of these ellipses, combined with the total light intensity, it is possible to estimate the direction, energy, and type (gamma-ray or hadron) of the primary particle.
In Figure 13 it is possible to look at the calibrated camera image which is obtained after the calibration of the signals recorded in the individual camera pixels, and to appreciate the difference between a gamma ray-initiated shower on the left side and a proton-initiated shower on the right side. The latter generates a wider and more diffused image respect to the gamma-ray induced one.
IACTs must contend with two main sources of background. The first is the Night Sky Background (NSB), which limits observations to dark, moonless nights, thereby reducing the instruments' duty cycle. The second is the overwhelming background of hadronic cosmic rays, which also generate atmospheric showers. While the NSB can be mitigated by observing conditions, the hadronic background requires sophisticated data analysis techniques, including Monte Carlo (MC) simulations and advanced classification methods (Mas Aguilar, 2025).
Modern IACTs often operate in stereoscopic systems, where multiple telescopes observe the same shower simultaneously. Combining the images significantly improves reconstruction accuracy.

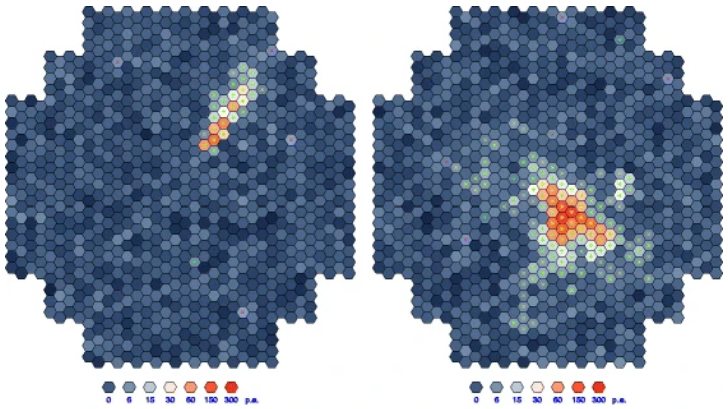

Figure 13: The figure presents camera images of the expected signals from simulations of a 1 TeV gamma-ray shower (left) and a 2.6 TeV proton shower (right). Signal strength in each pixel is shown in photo-electrons (p.e.) using a color scale (Völk and Bernlöhr, 2009).

2.5.1 CTAO- Cherenkov Telescope Array Observatory

Due to the remarkable progress in Very High Energy (VHE) (from 20 GeV to 300 TeV) gamma-ray astronomy, the need to construct an array of telescopes capable of further advancing this field has become evident. Enhancing the sensitivity of observations in this energy range is crucial for various astrophysical areas (a comparison plot between the sensitivities of different instruments is shown in Figure 14), including clarifying the origin of the highest energy cosmic rays within our Galaxy and beyond, understanding the physics of energetic particle generation in neutron stars and black holes, and probing the star formation history of the Universe. Furthermore, the CTAO will address critical questions in fundamental physics, such as the nature of quantum gravity and the identity

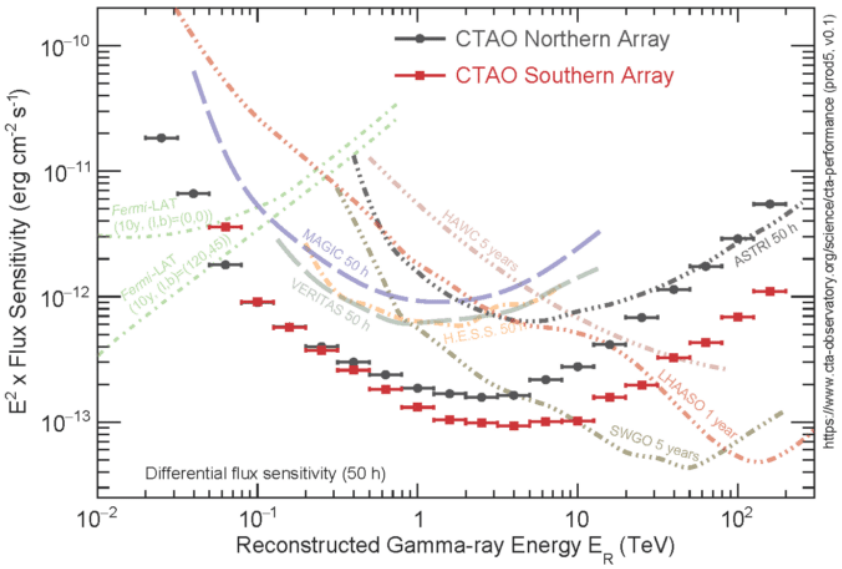

Figure 14: Sensitivity of CTAO-North and CTAO-South compared with current-generation gamma-ray telescopes, including HESS, Fermi-LAT, SWGO, VERITAS, MAGIC, HAWC, ASTRI, LHAASO, highlighting the improved performance across a broad energy range.

of dark matter particles.

As explained in Cortina (2019), the CTAO will operate on two sites: CTAO-North (Figure 16) in the Canary Islands, Spain, and CTAO-South in the Atacama Desert, Chile, with all telescopes employing IACT technology as their foundation. According to the Alpha Configuration (`https://www.ctao.org/news/ctao-releases-layouts-for-alpha-configuration/`), the observatory will include three types of telescopes to cover a broad energy range: four Large-Sized Telescopes (LSTs), each 23 meters in diameter, to observe the lowest energies (20–150 GeV); up to 23 Medium-Sized Telescopes (MSTs), 12 meters in diameter, distributed across both sites for the core energy range (150 GeV–5 TeV); and up to 37 Small-Sized Telescopes (SSTs), with diameters of 4.3 meters, located in the southern hemisphere to extend observations beyond 5 TeV (Figure 15) (Ambrosi et al., 2013).

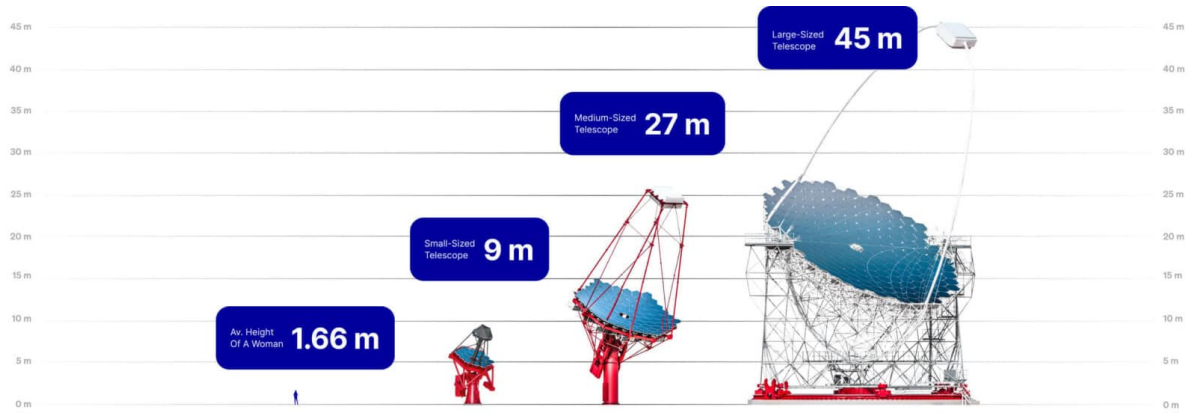

Figure 15: Comparison between the heights of Large-Sized Telescopes (LST), Medium-Sized Telescopes (MST), and Small-Sized Telescopes (SST), relative to the height of a person. Source: `https://www.ctao.org/`

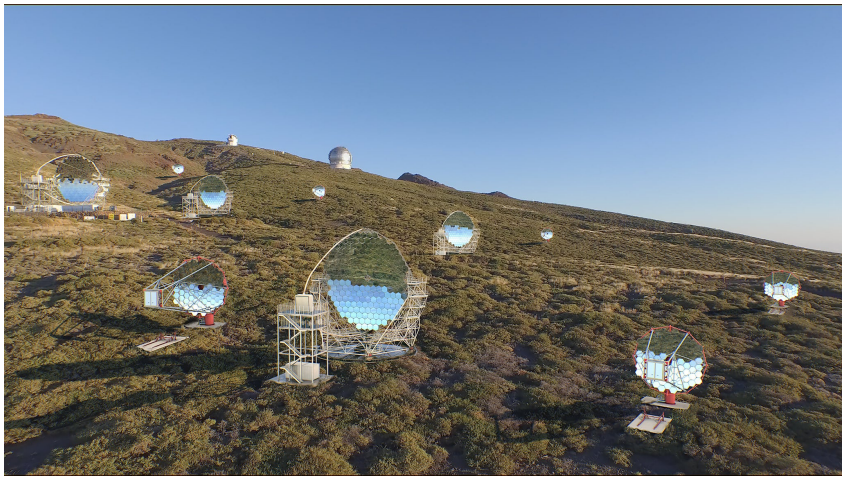

Figure 16: Artistic rendering of CTAO-North. Source: `https://www.ctao.org/`

2.5.2 Large-Sized Telescope - LST-1

LST-1 in Figure 17 is the only currently working telescope of the CTAO North array. It is situated at Roque de Los Muchachos in La Palma, Canary Islands, Spain, at an altitude of 2147 meters above the sea level. I present in the following an overview of the instrument:

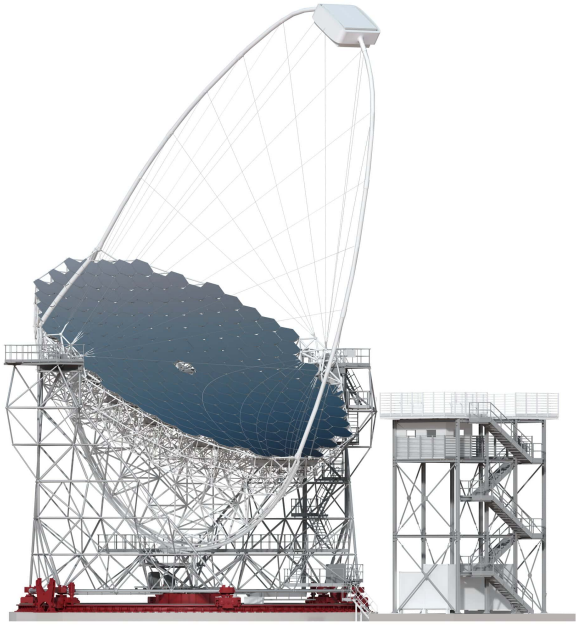

Figure 17: Image of the Large-Sized Telescope (LST-1), showing its main components: the compact, low-weight camera, the 23 m parabolic reflector supported by a reinforced carbon-fibre and steel structure, and the circular rail with bogies that allow the telescope to rapidly reposition across the sky. Credit: Gabriel Pérez Díaz, IAC. Source: `https://www.ctao.org/`

The geometry of the telescope is optimized to maximize the performance by Monte Carlo simulations. It is constituted by a light and compact camera that uses 1855 photomultipier sensors to convert light into electrical signals. It has a field of view of 4.3 degrees and it has been projected to be performant in the lower part of the VHE range.

The reflector has a parabolic shape and it is 23 meters wide, giving a total collection area of 400 m^2, composed by mirrors in honeycomb formation. The structure is supported by tubes made of steel and carbon fiber.
Finally, the whole structure is equipped with a circular 23 m diameter rail and six wheel bogies that it uses to quickly spin to any point to in the sky in less than 20 seconds. The foundations of the other LSTs will have a similar structure, but for each telescope it needs to be adapted based on the soil conditions, especially for CTAO-South ones.
All the fast and precise movements of LST-1 are coordinated by four synchronized motors used for the azimuth axis and two used for the elevation.
LST-1 will be part of a sub-array of four large-sized telescopes at CTAO-North and CTAO-South, targeting a range between $\sim$ 20 GeV and $\sim$ 100 GeV.
Thanks to its light architecture, LST-1 is suitable for observing transient events (both galactic and extragalactic) like GRBs. Other major physics drivers for LST-1 are pulsars and Extragalactic Background Light (Cortina and Teshima, 2015; Cortina, 2019).

Figure 18: Real picture of LST-1. Image credits : Irene Albanese.

3 LST-1 Data Analysis

The analysis of gamma-ray data is a multi-stage process, structured into several distinct data levels, each responsible for a specific part of the data reduction and calibration pipeline. In this chapter, we provide an overview of these data levels, highlighting their main characteristics and roles within the overall analysis framework. Particular emphasis is placed on Data Level 3 (DL3), which represents the starting point for the generation of the final scientific products, such as spectra, light curves, and sky maps.
Furthermore, we present the detailed analysis of the LST-1 observations of our target source, NGC 1068. This section discusses the adopted methodologies, the specific challenges encountered during the data processing (which are extensively described in Appendix A), and the final results obtained from the analysis.

3.1 Analysis pipeline

Once the data from the IACT has been acquired, it undergoes a series of processing steps aimed at extracting the physical properties of the primary gamma rays. The first stage involves filtering and calibration, which corrects for instrumental effects and removes spurious events. These calibrated data are then used for the reconstruction of key shower parameters, such as the estimated arrival direction of the gamma ray, its energy, and its time of arrival. This entire workflow is carried out using the dedicated data-reconstruction pipeline `cta-lstchain` (Moralejo et al., 2025; López-Coto et al., 2020), which provides the standard data reduction and analysis pipeline for the LST of the CTAO.
The workflow transforms raw telescope recordings into science-ready products through successive calibration, image reconstruction, and event classification stages. The final output consists of high-level data products that are suitable for astrophysical analyses with tools like `Gammapy`.

3.2 Data levels

In IACT experiments, observational data undergo a hierarchical framework of well-defined processing stages, referred to as data levels. A schematic representation can be visualized in Figure 19. These levels describe the transformation from raw detector output to final science-ready products. At the earliest stage, the system records unprocessed digitized signals from the telescope cameras, preserving the exact measurements for calibration and verification. Subsequent levels apply calibration procedures to correct instrumental effects, extract Cherenkov images from the background noise, and reconstruct the physical properties of the detected air showers, such as arrival direction and energy. The highest levels comprise high-level scientific products, such as sky maps, spectra, and light curves. A detailed description of the data levels is provided below, as established for the future CTAO. For LST-1 data at present, the levels begin at DL1.

- R0 – Raw Level 0: represents the direct output from the front-end electronics, which digitize the signals from the photomultiplier tubes selected by the trigger system of LST-1. The R0 data consist of high-frequency, uncalibrated waveforms that are not permanently stored but instead passed directly to the subsequent stages of processing.

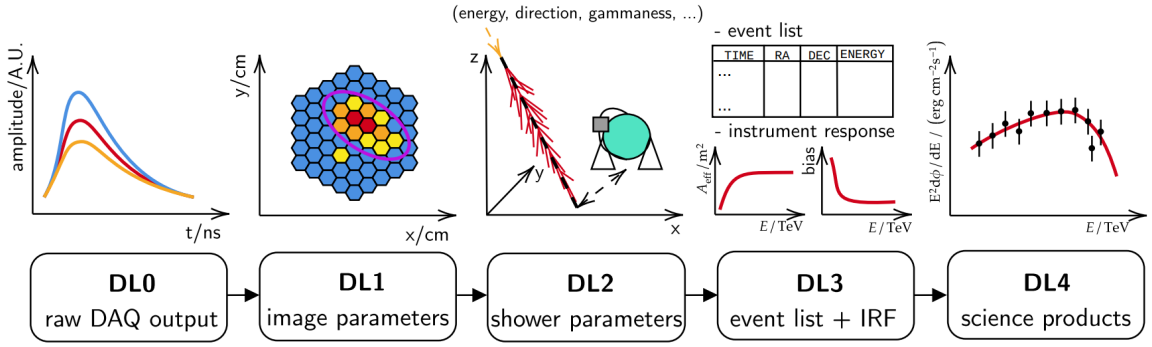

Figure 19: Data levels of IACTs of CTAO from Nigro et al. (2021), showing the general data reduction workflow. DL0: raw data acquisition (DAQ) output; DL1: image parameter extraction; DL2: shower reconstruction (energy, direction, particle type); DL3: event lists combined with instrument response functions (IRFs); DL4: final science products, such as energy spectra or flux measurements.

- R1 – Raw Level 1: data are obtained after minimal online processing by the Data Acquisition System (DAQ). In this stage, the DAQ builds complete events by collecting data from the previous level, assigning event numbers, and associating trigger and timing information. A fast calibration is performed to correct known distortions in the digitizing electronics.

- DL0 – Data Level 0: represents the first stage at which data are written to disk and stored permanently. The DL0 data are essentially R1 data organized into multiple data streams to enable efficient disk writing and, in some cases, compression. During this stage, signal amplitudes are integrated over the waveform samples and converted from Analog-to-Digital Converter counts to physical units (photoelectrons, p.e., per pixel).

- DL1 – Data Level 1: is divided into two sub-levels – DL1a and DL1b.
  In DL1a, the waveform data are analyzed and calibrated. The arrival time of the signal at each pixel is also estimated. The calibration process uses DL0 calibration data, which are obtained during dedicated calibration runs or as artificially triggered calibration events along with observational data. The output of DL1a consists of calibrated camera images in p.e. units along with corresponding timing maps.
  DL1b contains geometric parameters derived from cleaned camera images, where noise pixels have been removed. The most relevant features are the so-called Hillas' parameters (Hillas, 1985), which approximate the image shape as a two-dimensional ellipse (Figure 20) and from which we also extract the temporal information. At this stage, information from individual pixels is discarded, and only the event-level information are retained.

- DL2 – Event Classification and Reconstruction: This stage involves classifying events according to their probability of being induced by a gamma-ray primary particle or a cosmic ray, as well as reconstructing their energy and arrival direction. Machine learning techniques, in particular Random Forests (RFs), are employed using the features derived from DL1b. The RFs are generated with `lstmcpipe`

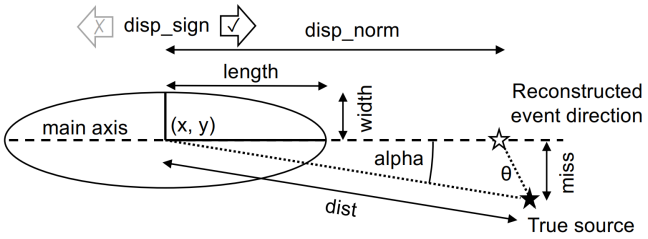

Figure 20: Illustration of Hillas' parameters used in the reconstruction of atmospheric shower images (Project et al., 2023). The main axis, defined by the elongated image shape, is characterized by its length and width. The image centroid is given by (x, y), while alpha describes the angle between the shower axis and the source position. The disp parameters (`disp_norm` and `disp_sign`) are used to estimate the displacement along the main axis toward the reconstructed event direction. Additional quantities such as dist, miss, and θ quantify the separation between the image centroid, the true source position, and the reconstructed direction, respectively.

(Garcia et al., 2022) and trained using Monte Carlo (MC) simulations: gamma-ray MCs for energy and direction reconstruction, and both gamma-ray and proton MCs for classifier training. Since using all MC data would be computationally too heavy, the simulations are produced at specific pointing nodes along different declination lines, visible in Figure 21.

- DL3 – User-Delivered Data: represents the data products delivered to end-users. Each DL3 dataset contains two main components: (i) a list of gamma-like events selected from DL2 after background rejection, and (ii) the Instrument Response Functions (IRFs), which are derived from Monte Carlo simulations processed with identical reconstruction and selection criteria as the observational data. The IRFs include the effective collection area, the point-spread function (PSF), and the energy migration matrix, that links the reconstructed and true energies of gamma rays. DL3 data also include pointing and livetime information, as well as metadata describing observation conditions.
  These datasets are stored in FITS format, indexed by observation, and are compatible with open-source high-level analysis tools such as `Gammapy`.

- DL4 – Binned Data: the DL3 event lists are binned according to their reconstructed energy and position on the sky, assuming a geometry and coordinate system. The binned data provide the basis for subsequent scientific analysis.

- DL5 – Final Science Products: contains the final science products derived from modeling and fitting the DL4 datasets. These products include flux and Test-Statistic (TS) sky maps, light curves, and spectral energy distributions (SEDs). DL5 products can be compiled to generate source catalogs and sky survey maps.

3.3 High level analysis

This section describes the analysis process starting from the DL3 data level, following Morcuende Parrilla (2023). It covers calculating the signal's significance, creating sky maps, and producing the light curve and spectral energy distribution (SED). As our

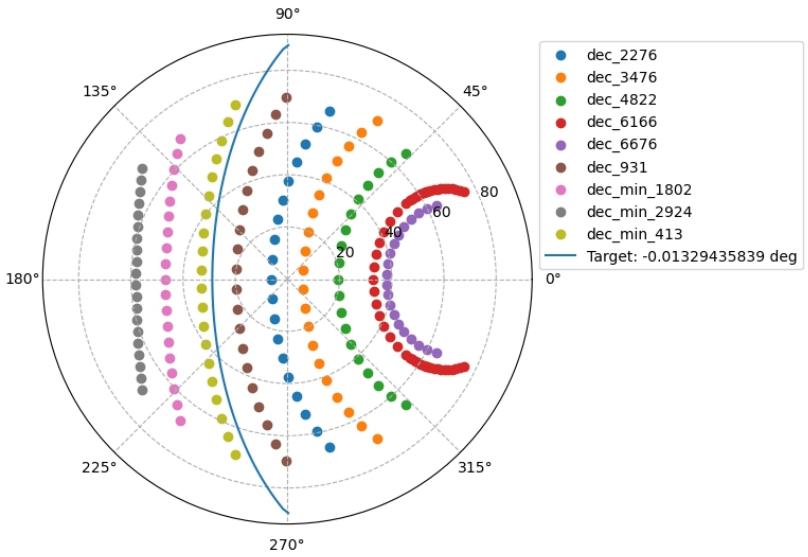

Figure 21: Declination lines used for generating MC simulations to train the RF, and pointing nodes where the RF training is performed.
Plot by S. Menon (sweta.menon@inaf.it) for NGC 1068.

analysis has been performed for a point-like source, we did not produce the sky maps as they are of low interest for our kind of source.

3.3.1 Detection Significance and Sky Maps

There are two main strategies for estimating the signal and subtracting the background: **ON/OFF mode** and **wobble mode**.

ON/OFF mode: The telescope points directly at the source (ON region, which contains both the source and the background emission), therefore gamma rays from it are recorded in the center of the field of view (FoV). To figure out how many of those events actually come from the source, we also observe a nearby control region with no expected gamma-ray emission to measure the background (OFF region). The downside is that we need to spend an amount of observation time looking at an "empty" part of the sky.

Wobble mode: To use observation time more efficiently, the telescope points slightly off from the source, typically by about 0.4° for LST-1 in its current observation scheme, so that the same FoV contains both the on-source region and several off-source regions for background estimation (Figure 22). The pointing direction is shifted between different positions around the source during the observation to reduce systematic effects that might affect a single position.

To measure how strong a gamma-ray signal is from a given source, we use a statistical test called a likelihood ratio test. This compares two scenarios: one where there's no gamma-ray source and one where there is a source producing an excess of gamma rays. For this, we apply the method by Li and Ma (1983), which calculates the detection significance using the number of events recorded in the on-source region and in separate off-source control regions. This method is reliable when each region contains at least

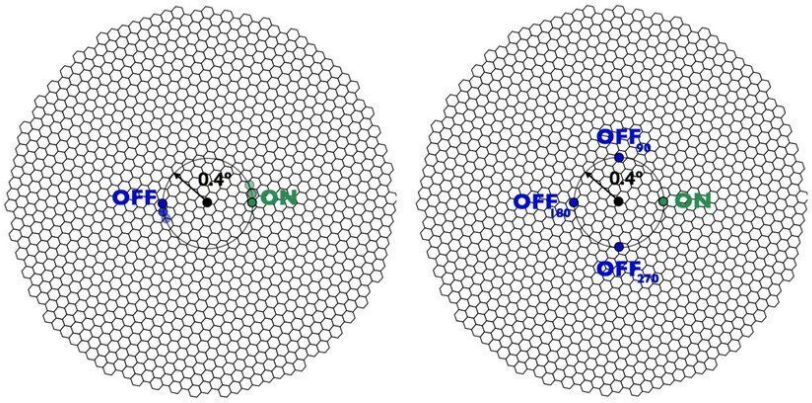

Figure 22: Schematic view of the wobble pointing mode (López Coto, 2015). The black point represents the center of the camera, then a region at 0.4° of distance is defined. The on region is where the source is. In this particular case two situations are represented: case of 1 OFF region (on the left), the background is taken from a region oppositely as the ON region; case of 3 OFF regions (on the right), the background is taken from regions equally spaced and respectively at 90°, 180° and 270° from the ON region. Even if those configurations are commonly used, it is possible to shift the OFF regions at different position angles.

about ten events. The Li & Ma formula for the significance S is:

$$S = \sqrt{2\left[N_{\text{on}} \ln\left(\frac{(1+\alpha)N_{\text{on}}}{\alpha(N_{\text{on}}+N_{\text{off}})}\right) + N_{\text{off}} \ln\left(\frac{(1+\alpha)N_{\text{off}}}{N_{\text{on}}+N_{\text{off}}}\right)\right]} \tag{2}$$

where:

- N_{on} = number of events in the on-source region,
- N_{off} = number of events in the off-source region,
- α = ratio of observation time between ON and OFF regions.

Sky maps are another key product of high-level gamma-ray analysis. They show the reconstructed arrival directions of gamma-ray–like events, either in the telescope's camera coordinates or, more commonly, in a celestial coordinate system (equatorial or horizontal). The accuracy of each reconstructed position, relative to the true source location, is determined by the point-spread function (PSF), the response of a focused imaging system to a point source. Sky maps are especially valuable for studying extended sources, as they reveal the source's spatial morphology beyond the telescope's PSF size.

3.3.2 Spectrum and Light Curve

The gamma-ray flux, which describes the rate of detected photons per unit area,

$$\Phi = \frac{d^2N}{dA\,dt} \quad [\text{cm}^{-2}\,\text{s}^{-1}], \tag{3}$$

can be characterized either as a function of photon energy (spectrum) or as a function of time (light curve). Its determination requires three key ingredients: the number of detected gamma-ray events attributed to the source, the effective collection area of the

instrument, and the effective observation time. This last quantity is obtained from the total elapsed observation duration, corrected for the readout system's dead time, under the assumption of a Poissonian distribution. The effective collection area is estimated through MC simulations in which gamma rays are uniformly generated over a large area with random impact points. These simulated events are processed with the same reconstruction and selection criteria as the real data, and the effective area is computed from the ratio of events surviving all cuts to the total number generated. Since this quantity depends strongly on energy and zenith angle, it is necessary to evaluate it across the relevant parameter space. Background-rejection cuts further affect its value, making it important that the Monte Carlo simulations provide sufficient coverage of energy and angle to correctly estimate it.

To estimate the number of gamma-ray events originating from the source, the background contribution is evaluated using the OFF regions. For each reconstructed event, we calculate the angular distance θ from the center of the ON or OFF region. Assuming a radially symmetric background, the θ^2 distributions of background events in the ON and OFF regions are expected to be identical, apart from statistical fluctuations. From the measured excess, defined as the difference between the ON counts and the OFF counts, and the instrument response, the differential energy spectrum is derived as

$$\frac{d\Phi}{dE} = \frac{d^3N}{dA\,dt\,dE} \quad [\mathrm{cm}^{-2}\,\mathrm{s}^{-1}\,\mathrm{TeV}^{-1}], \tag{4}$$

or expressed in the form of SED,

$$E^2\,\frac{d\Phi}{dE}.$$

Initially, the event list is expressed as a function of the estimated photon energy; however, to recover the distribution in true energy, the finite energy resolution of the instrument (typically $\sim 15\%$ for current IACTs) must be taken into account, as it leads to spillover between energy bins and can distort the spectral shape. This effect is described by the migration matrix. The matrix is derived from Monte Carlo gamma-ray simulations, where both quantities are available.

The temporal evolution of the source emission is captured through the light curve, obtained by dividing the observations into time bins and, assuming a fixed spectral shape with only the normalization allowed to vary, calculating the integrated flux over a chosen energy range in each bin. This yields the gamma-ray flux as a function of time.

3.3.3 `Gammapy`

In the context of CTAO, the high-level analysis outlined before is carried out using dedicated science tools such as `Gammapy` (Acero et al., 2025), which take as input the DL3 data files containing the list of selected gamma-ray events along with the corresponding IRFs.

The procedure begins with the creation of a `DataStore` object, which stores the set of observation blocks to be processed. These blocks contain the selected gamma-ray events, each characterized by its arrival time, reconstructed energy, and sky coordinates. From this information, `Gammapy` can compute the statistical significance of the gamma-ray excess using its built-in statistical functions.

The first reduction step involves binning the event list in energy, corresponding to the transition from DL3 to DL4 data. An ON region, centred on the source position, is defined to extract the signal spectrum. The aperture of this region can be constant

across all energies or vary with energy, depending on how the angular cut θ was applied to select the events in both the observational (DL3) and simulated datasets (used for IRF computation). Likewise, reflected OFF regions are specified for background estimation, positioned symmetrically opposite to the ON region (Figure 22). At this stage, a `SpectrumDatasetOnOff` object is created, containing the gamma-ray counts from the ON region and the background counts from the OFF regions, both binned in energy and stacked over all observations.
Next, in general a spectral shape is chosen to be used in the forward-folding method for extracting the source spectrum. and a maximum-likelihood fit is performed to the observed counts, adopting the previously defined spectral model. In addition, `Gammapy` can compute spectral flux points using the `FluxPointsEstimator`, which fits the model normalization independently in each energy bin. Finally, the light curve is derived from the reduced dataset via the `LightCurveEstimator`.
The extraction of the SED and light curve constitutes the transition from DL4 to DL5 data.
A complete scheme of the whole high level analysis process can be visualized in Figure 23.

3.4 Results from the analysis of NGC 1068

3.4.1 Data quality

A crucial first step in data analysis is to select only runs (observations of the duration of $\sim$20 minutes) that were taken under stable and well-understood conditions. Poor data quality, caused by instrumental problems, variable atmospheric transparency, or high night-sky background (NSB), can introduce systematic uncertainties that compromise flux, spectral, or timing studies.
The default cuts applied here are optimized for low-NSB data and are intended to provide a reliable sample for flux and spectrum analyses.
The selection relies on the intensity spectra of cosmic-ray showers, dR/dI, measured in (events/s/p.e.), where I is the image intensity, representing the total number of photoelectrons (p.e.) in selected pixels. Cosmic rays provide a stable reference signal: at large intensities, the rate should depend mainly on pointing and remain stable if the telescope and atmosphere are behaving nominally.
If throughput is reduced (e.g. due to atmospheric absorption), the same showers will be reconstructed with lower intensity. This shifts the dR/dI distribution to smaller values. To quantify this effect, we fit the high-intensity part of the spectrum (316–562 p.e.) with a power law. After correcting for zenith-angle dependence, two parameters are extracted:

- the power-law index,
- the rate at a reference intensity of 422 p.e.

These serve as proxies for the stability and efficiency of the run.
Because these quantities are measured for each subrun, we can also assess stability within a run. Significant variations with time may indicate changing observation conditions. To quantify this, we compute a Lomb–Scargle periodogram of the reference rate versus time. The maximum amplitude provides a simple instability measure; runs with unusually large values are rejected.
A run is considered "good" if it meets the following conditions:

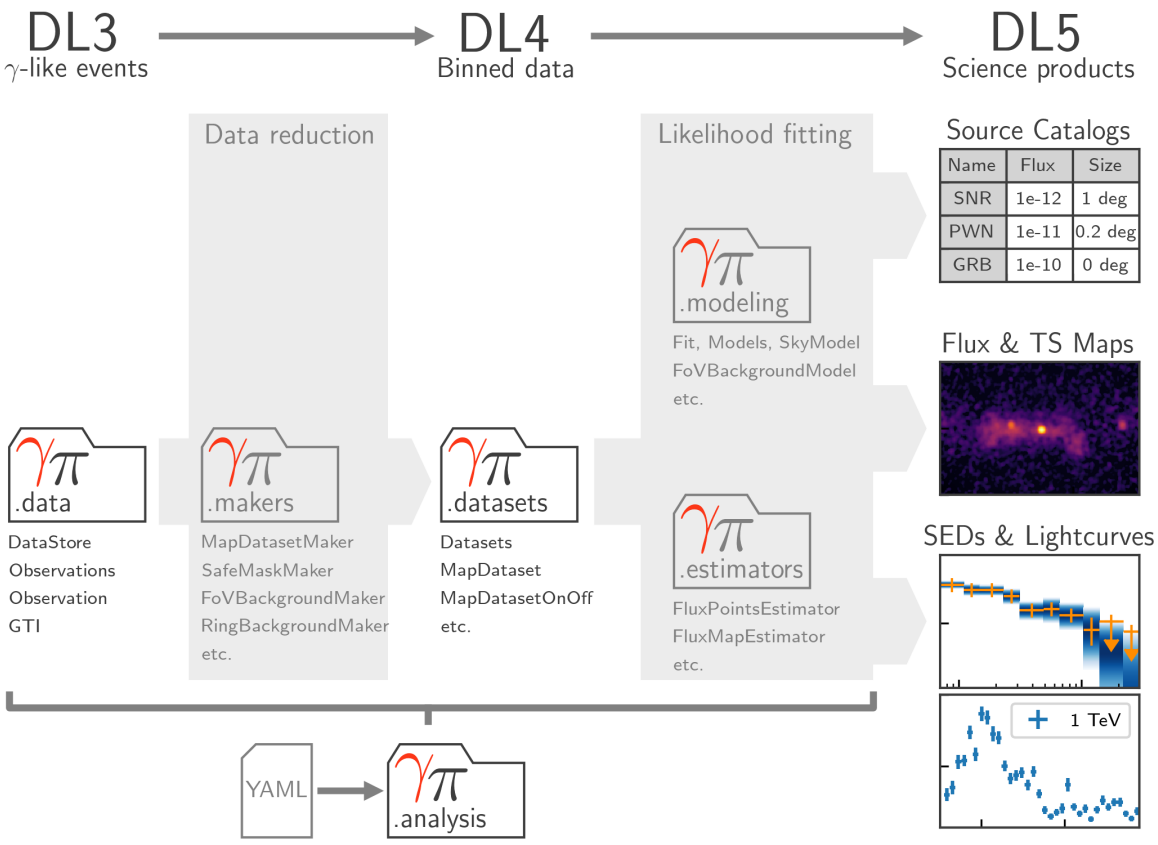

Figure 23: Gammapy sub-package structure and data analysis workflow. The top row illustrates the successive levels of data reduction, starting from lists of γ-ray-like events on the left (DL3) and progressing to high-level scientific products on the right (DL5). The direction of the data flow is indicated by gray arrows. White folder icons represent the different Gammapy sub-packages, with their names corresponding to the respective Python code suffixes (e.g., gammapy.data). Below each icon, the most relevant objects defined in the sub-package are listed. Light gray folder icons denote sub-packages that provide the fundamental data structures, such as maps and IRFs. At the bottom of the figure, the high-level analysis sub-module is shown together with its dependency on the YAML file format. Taken from Donath et al. (2023).

```
Number of runs (% is w.r.t. those in Sky region & zenith range):

    In the requested Sky region and range of dates:      203
  + zenith in requested range:                           135
  + NSB in requested range:                              135 (100.0%)

  + FF and pedestal interleaved events are present:      133 (98.5%)
  + Stable pointing:                                     131 (97.0%)
  + dR/dI fit P-value ok:                                128 (94.8%)
  + dR/dI LS periodogram ok:                             122 (90.4%)
  + dR/dI index ok:                                      114 (84.4%)
  + dR/dI rate ok:                                       74 (54.8%)
  + intensity threshold ok:                              74 (54.8%)
```

Figure 24: Numbers and percentage of surviving runs after the application of each selection cut, along with the final number of runs after applying all cuts in the Data Quality selection.

- Interleaved calibration events (flatfield and pedestal) are present.
- Pointing is stable throughout.
- The mean P-value of the spectral fits exceeds a threshold (to reject poor fits).
- The Lomb–Scargle variability amplitude is below a maximum value.
- The mean power-law index is within an acceptable range.
- The intensity threshold (where dR/dI falls to half its peak) is below a maximum allowed value.

These criteria ensure that the retained runs have stable pointing, well-behaved intensity spectra, and reasonable thresholds, providing a consistent dataset for physics analysis. For this work, we selected observations of the source NGC 1068, located at coordinates $(\mathrm{RA}, \mathrm{Dec}) = (40.670°, -0.013°)$. The dataset was restricted to runs taken between 2022 and 2025, with a zenith distance in the range 0°–50°. Starting from the complete set of available DL1 files, we applied the data quality selection criteria described above and extracted the subset corresponding to this source. After the application of all the cuts, a total of 74 runs were retained, corresponding to an effective observation time of 20.02 hours Figure 24.

3.4.2 DL1-DL2

Until few months ago, it was necessary to generate the DL2 files directly from the DL1 data (contain the calibrated and cleaned event images). Producing DL2 therefore required selecting the appropriate list of runs, choosing a declination line for the random forest models, and defining additional parameters needed for an eventual advanced-level analyses. At present, DL2 files are already available and can be used directly, as done in this work. Nevertheless, it remains possible to produce custom DL2 files from the DL1 data if one wishes to apply specific options or parameter choices.

3.4.3 DL2-DL3

Once we have all the proper run IDs from the data quality selection, we associate the corresponding DL2 data and the matching IRFs for each run. Then we simply convert the DL2 to DL3 files through `cta-lstchain`, obtaining a number of FITS file ready to be analysed using `Gammapy`.

3.4.4 Post DL3 analysis

Initially we perform a 1D spectral analysis following the ON–OFF forward-folding method, but due to low statistics the fit was not converging, hence we decided to use the Fermi spectral shape in our analysis without performing the fit, and compute the light curve and SED for point-like source observations in wobble mode using point-like IRFs. Fermi-LAT data were taken from the latest version of the catalog, 4FGL-DR4 (Ballet et al., 2024), released on 24 July 2024. From these data, the spectral model parameters (Table 1) for NGC 1068 were extracted.
In the initial stage of the work, we conducted an analysis following the usual approach and parameters commonly used by the LST Collaboration, which we will refer to as standard analysis, the details of which are reported in the Appendix A as it constituted a huge part of the work.
While this approach provided a useful starting point, it also revealed issues particularly concerning the background that have been analyzed and reported to the LST Collaboration during the LST Analysis Meeting. During the meeting we have been suggested by other members to treat this source with a different approach and to perform the analysis at higher values than usual of the reconstructed energy minimum value (*e_reco_min*). The often used values are around $0.05 - 0.1$ TeV. After numerous attempts, we selected 0.6 TeV as the best value for the *e_reco_min* due to the fact that the result no longer showed the issues related to the background.
In Figure 25, the excess as a function of livetime shows the expected behavior. Instead of fluctuating, it steadily increases with livetime, which is exactly the trend we would expect for a real signal.

Parameter	**Value**
Spectral index Γ	2.35
Normalization amplitude A	$1.2 \times 10^{-13}\,\mathrm{cm^{-2}\,s^{-1}\,TeV^{-1}}$
Reference energy	1 TeV

Table 1: Fermi spectral parameters.

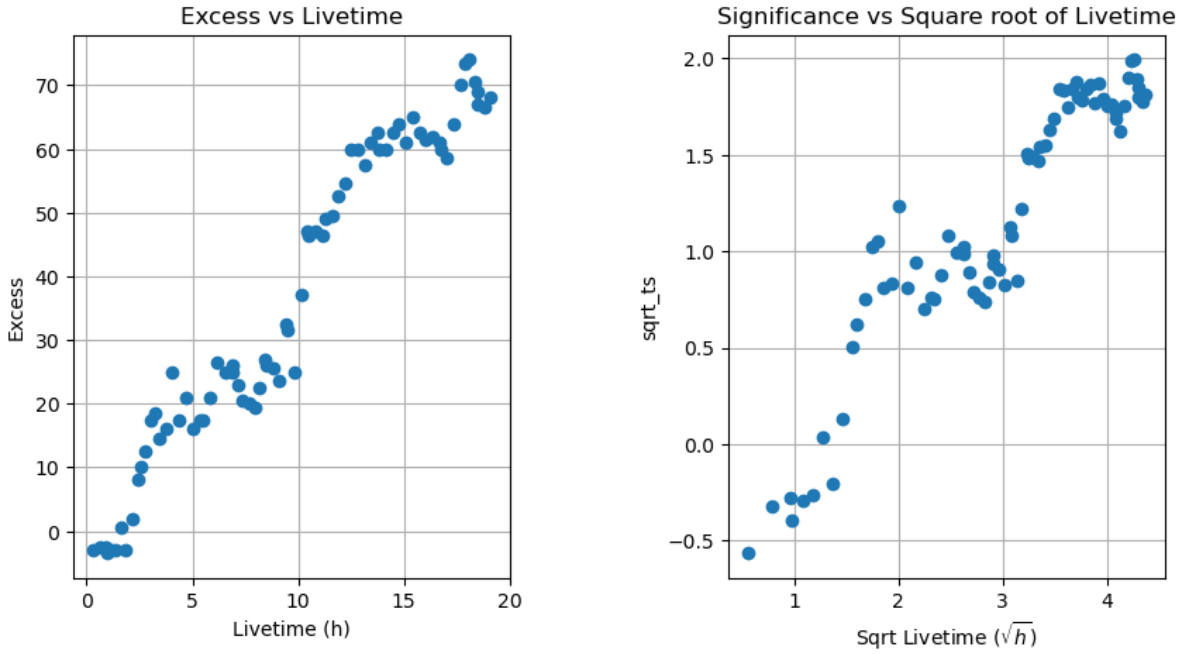

Figure 25: Temporal evolution of excess events and significance value for *e_reco_min* = 0.6.

The choice of a threshold at 0.6 TeV was motivated by the fact that already at 0.5 TeV the excess (shown in Figure 26) starts to show some fluctuations due to background non-uniformity, making 0.6 TeV a safer lower limit for the analysis.

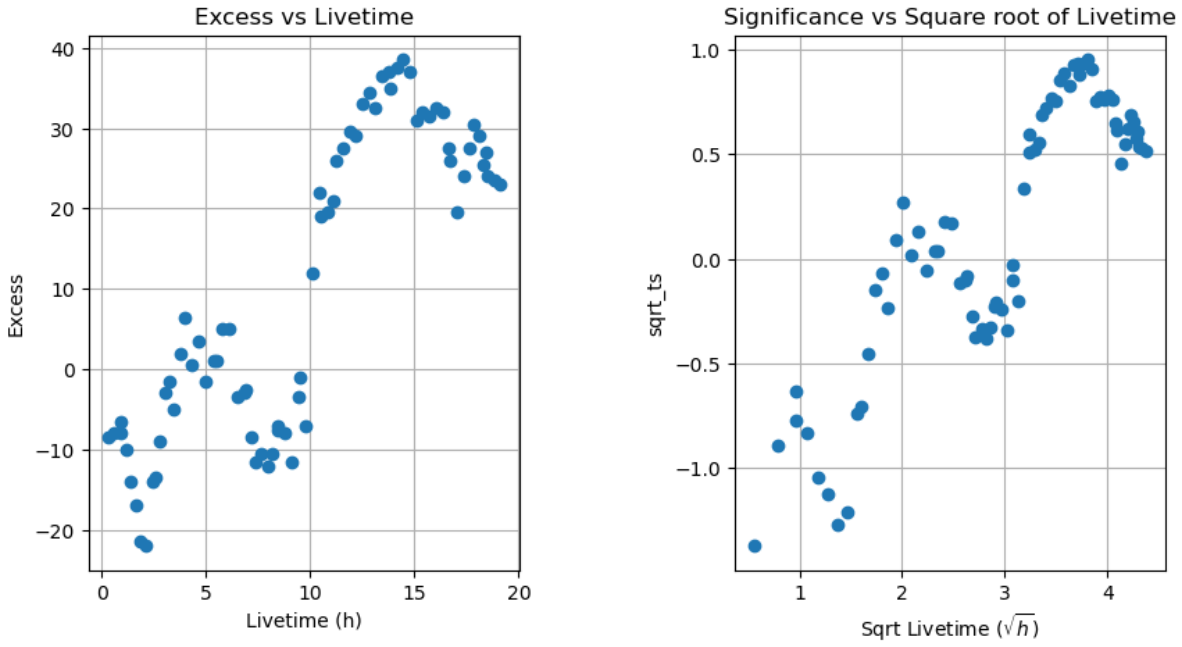

Figure 26: Temporal evolution of excess events and significance value for *e_reco_min* = 0.5.

From the list of flux points, we decided to remove the four at the highest energy, as they were based on very low statistics (only 1–3 photons) and therefore not significant enough to be included. With this selection, we obtained the final SED, shown in Figure 27.

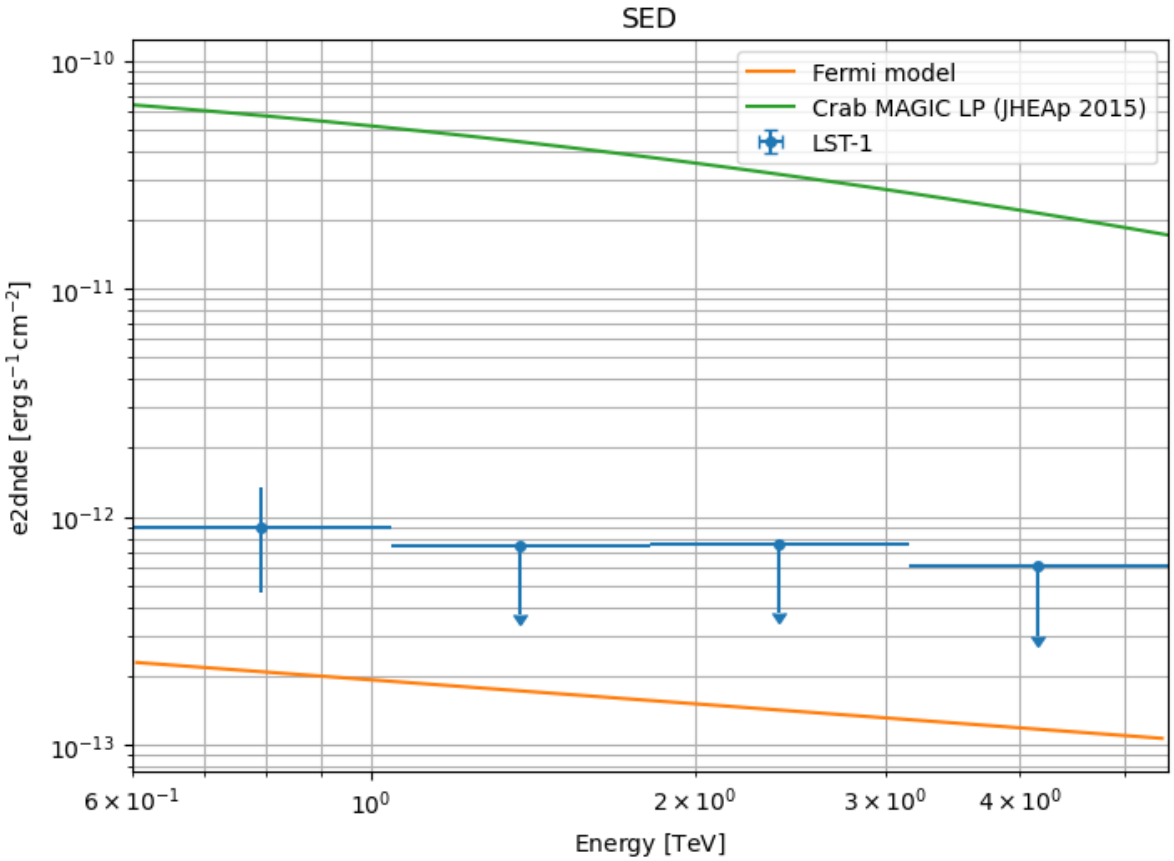

Figure 27: Spectral energy distribution for *e_reco_min* = 0.6.

The resulting SED now contains three upper limits and one flux point. The flux point is retained because, in this case, the significance exceeds the 2σ generally set in the community for this kind of analysis.
Finally, the light curve is shown in Figure 28.
While identifying a suitable solution for the present analysis is important, the primary objective of the LST is to extend the sensitivity of observations toward lower energies. In this regard, the dataset for NGC 1068 appears to exhibit inconsistencies with respect to the excess in the low-energy range (0.01–0.6 TeV). These issues may be related to background subtraction, limited statistics, or challenges in the energy reconstruction at such low energies. Consequently, this energy band requires further dedicated investigation in order to better understand the systematics involved and to ensure reliable results.

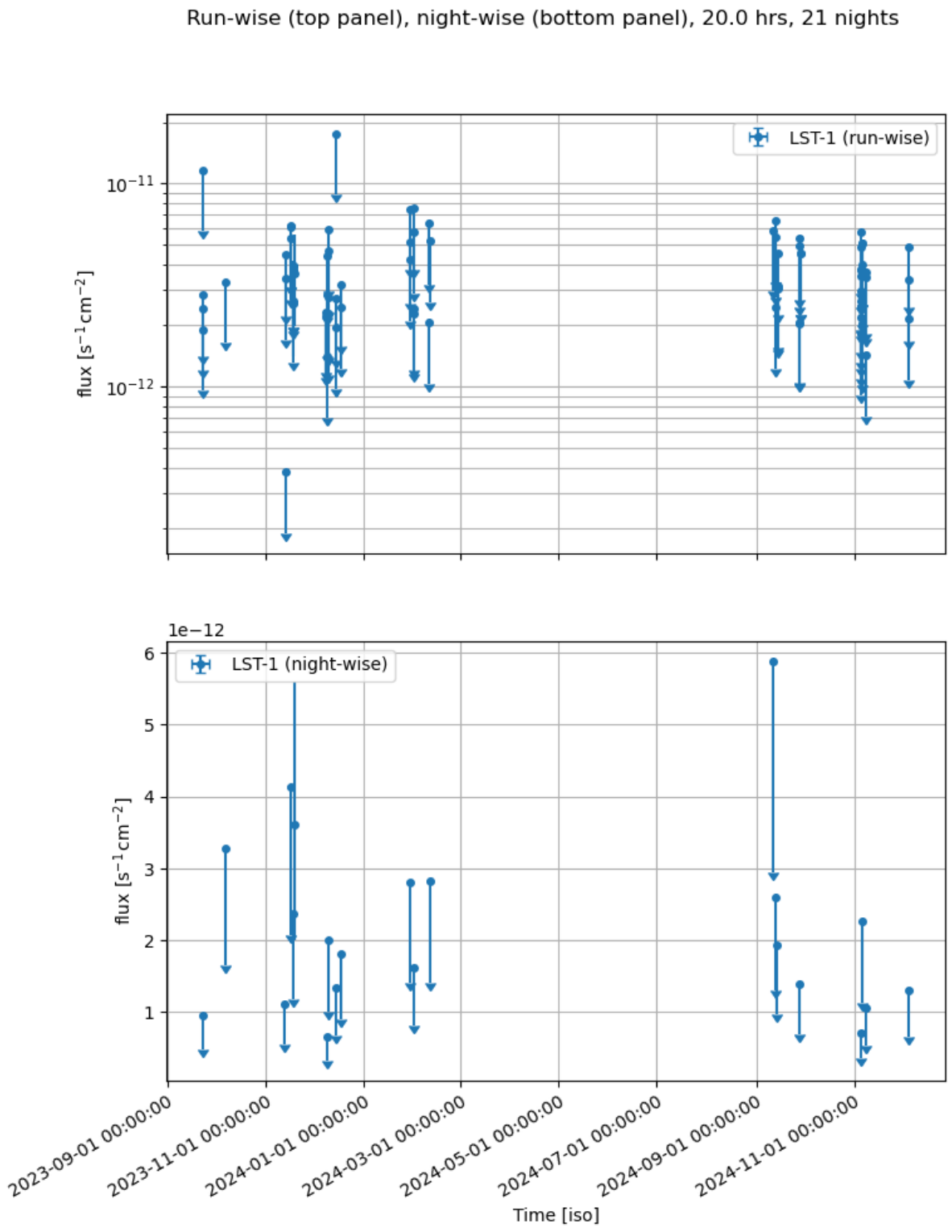

Figure 28: The top panel presents the light curve with run-by-run binning, where each run spans approximately 20 minutes. The bottom panel shows the light curve binned by night, with all observations from a given night combined into a single data point. Both light curves were generated using *e_reco_min* = 0.6.

4 Model of the starburst region of NGC 1068

In this chapter we present a one-zone model of the non-thermal emission of the starburst region of NGC 1068, where both hadronic and leptonic particle populations are treated self-consistently. The choice of a one-zone description allows us to capture the dominant physical processes within a compact region while keeping the model analytically and numerically tractable. The steady-state transport equation is solved including the main energy loss and interaction processes: for protons, ionization and inelastic *pp* collisions; and for electrons, synchrotron emission, inverse Compton scattering, bremsstrahlung, and ionization. By computing the resulting steady-state particle distributions and their associated radiative outputs, we obtain a multiwavelength spectral energy distribution that directly reflects the interplay of hadronic and leptonic mechanisms. Additionally, we take into account the absorption of high-energy photons through $\gamma\gamma$ pair production, which affects the SED.
The predicted emission is then compared with observational data across radio, X-ray, and gamma-ray bands available in the literature and with data obtained from the LST-1 Analysis, a process that has been extensively explained in Chapter 3 . This comparison not only provides constraints on key physical parameters such as the gas density, magnetic field strength, and radiation energy density in the starburst environment, but also offers insights into the relative importance of different non-thermal processes operating in NGC 1068. Ultimately, this analysis contributes to a deeper understanding of the high-energy phenomenology of active galaxies and the role of starburst regions as potential cosmic-ray accelerators.
This chapter will focus on the theoretical explanation of all the radiative and non-radiative processes taken into account with a focus on the energy loss mechanisms that are fundamental to explain the final emission signal, and on the assumptions that we used to build up the model. To ensure the readability of this chapter, the results will be presented separately.

4.1 Radiative and non radiative mechanisms

4.1.1 Proton-proton collisions (p-p)

When relativistic protons interact with low energy protons in a p-p collision there is production of mesons, in particular pions π that can be neutral (π^0) or charged (π^+, π^-). The possible reactions resulting from a collision are:

$$p + p \rightarrow p + p + \pi^0 + a\pi^0 + b(\pi^+ + \pi^-) \tag{5}$$

$$p + p \rightarrow p + n + \pi^+ + a\pi^0 + b(\pi^+ + \pi^-) \tag{6}$$

$$p + p \rightarrow n + n + 2\pi^+ + a\pi^0 + b(\pi^+ + \pi^-) \tag{7}$$

with multiplicity a and b.
The average life of a neutral pion π^0 is around 10^{-17}s. After that it decays in two photons:

$$\pi^0 \rightarrow \gamma + \gamma \tag{8}$$

On the other side, the charged pions decay more slowly (after $\sim 10^{-8}$), producing muons μ and neutrinos ν:

$$\pi^+ \to \mu^+ + \nu_\mu \tag{9}$$

$$\pi^- \to \mu^- + \bar{\nu}_\mu \tag{10}$$

The emissivity injected from neutral pion decay produced from inelastic p-p collision is given by:

$$q_\pi(E_\pi) = c\, n_H \int_{E_p^{\min}}^{E_p^{\max}} N_p(E_p)\, \frac{d\sigma_\pi}{dE_\pi}(E_p, E_\pi)\, dE_p \tag{11}$$

in which n_H is the gas density, c is the speed of light, $N_p(E_p)$ represents the energy distribution of the relativistic protons that interact with low-energy protons, and $\frac{d\sigma_\pi}{dE_\pi}(E_p, E_\pi)$ is the differential cross section needed for the production of π^0 with energy E_π, through a proton of energy E_p.
The the differential cross section can be function of the p-p cross section, defined as:

$$\sigma_{pp}(E_p) = \left[34.3 + 1.88L + 0.25L^2\right] \left[1 - \left(\frac{E_p^{\rm th}}{E_p}\right)^4\right]^2 \text{ mb} \tag{12}$$

where $L = \ln\left(\frac{E_p}{1\,\text{TeV}}\right)$, $\quad E_p^{\rm th} = T_p^{\rm th} + m_p c^2 \approx 1.22\,\text{GeV}$.
Once the emissivity of neutral pions in known, it is possible to calculate the one of γ-rays as:

$$q_\gamma(E_\gamma) = 2 \int_{E_\pi^{\min}}^{\infty} q_\pi(E_\pi)\, \frac{dE_\pi}{\sqrt{E_\pi^2 - m_{\pi^0}^2 c^4}}, \tag{13}$$

where

$$E_\pi^{\min}(E_\gamma) = E_\gamma + \frac{m_{\pi^0}^2 c^4}{4E_\gamma},$$

with E_γ being the energy of gamma-rays and m_{π^0} the mass of neutral pions.
An example of spectral energy distribution is shown in Figure 29.

The energy loss rate of a relativistic proton due to inelastic p-p collisions with target protons of number density n_H is given by:

$$-\left.\frac{dE_p}{dt}\right|_{pp} = c\, n_H\, K_{pp}\, E_p\, \sigma_{pp}(E_p)\, \Theta(E_p - E_p^{\rm th}), \tag{14}$$

where:

- $K_{pp} \approx 0.5$ is the inelasticity parameter representing the average fraction of proton energy lost per collision,
- $\Theta(x)$ is the Heaviside step function, defined as

$$\Theta(x) = \begin{cases} 1, & x \geq 0, \\ 0, & x < 0, \end{cases}$$

which ensures that energy losses occur only when E_p is above the threshold energy $E_p^{\rm th}$ required for pion production, which is 280 MeV.

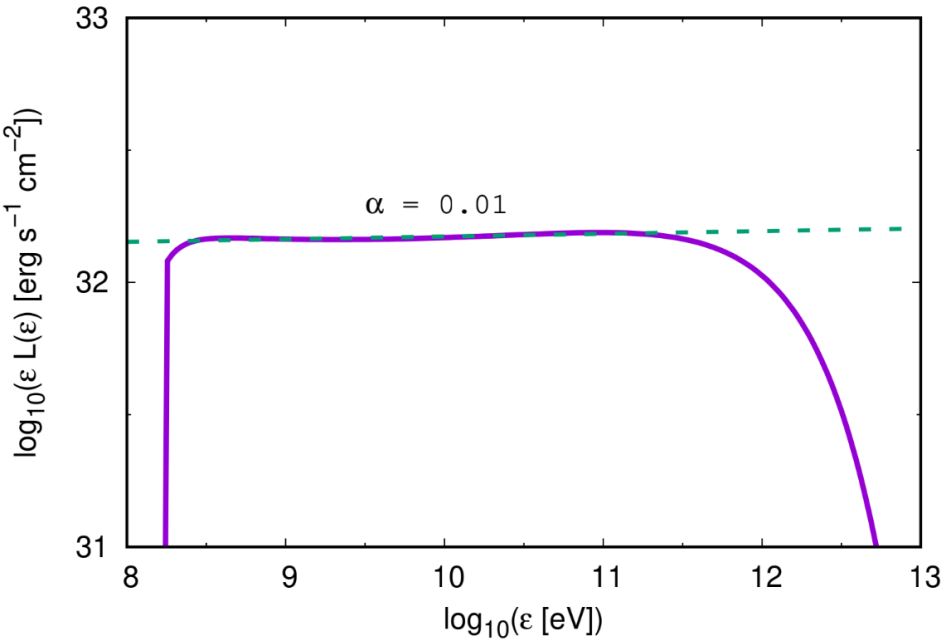

Figure 29: SED generated by a power-law distribution of protons in a homogeneous matter field for a proton distribution like $N_p(E_p) \propto E_p^{-2}$. Given the initial particle distribution in the power law form ($n = K \cdot E^{-p}$) the final SED will have a slope corresponding to $\alpha = -(p-2)$ (Romero, 2021).

4.1.2 Bremsstrahlung

Relativistic bremsstrahlung is the radiation produced when a relativistic electron is accelerated in the electrostatic field of a nucleus or another charged particle.
If we consider the production of a photon with energy E_γ by a relativistic electron with energy $E_e \gg m_e c^2$, which is scattered by a nucleus of charge Ze, then the differential cross section for this interaction is:

$$\frac{d\sigma_{\rm Br}}{dE_\gamma}(E_e, E_\gamma) = 4\alpha r_e^2 Z^2 \frac{1}{E_\gamma}\,\phi(E_e, E_\gamma), \tag{15}$$

where $r_e = e^2/(m_e c^2)$ is the classical electron radius and $\alpha \approx 1/137$ is the fine-structure constant. ϕ is a function that depends on the ionization state of the target.
In the case of a fully ionized gas, it is given by:

$$\phi(E_e, E_\gamma) = \left[1 + \left(1 - \frac{E_\gamma}{E_e}\right)^2 - \frac{2}{3}\left(1 - \frac{E_\gamma}{E_e}\right)\right]\left[\ln\left(\frac{2E_e(E_e - E_\gamma)}{m_e c^2 E_\gamma}\right) - \frac{1}{2}\right], \tag{16}$$

The emissivity of the radiation produced is:

$$q_\gamma^{\rm Br}(E_\gamma, \vec{r}) = \frac{c n_a(\vec{r})}{4\pi}\int_{E_\gamma}^{\infty} \frac{d\sigma_{\rm Br}}{dE_\gamma}(E_e, E_\gamma) n_e(E_e, \vec{r})\, dE_e \quad [\mathrm{erg}^{-1}\,\mathrm{cm}^{-3}\,\mathrm{s}^{-1}\,\mathrm{sr}^{-1}], \tag{17}$$

where n_a is the target density and n_e the spectrum of relativistic electrons.
The energy losses by bremsstrahlung for electrons can be very large, allowing them to radiate photons with energies $E_\gamma \sim E_e$. In the case of an ionized plasma, these losses are:

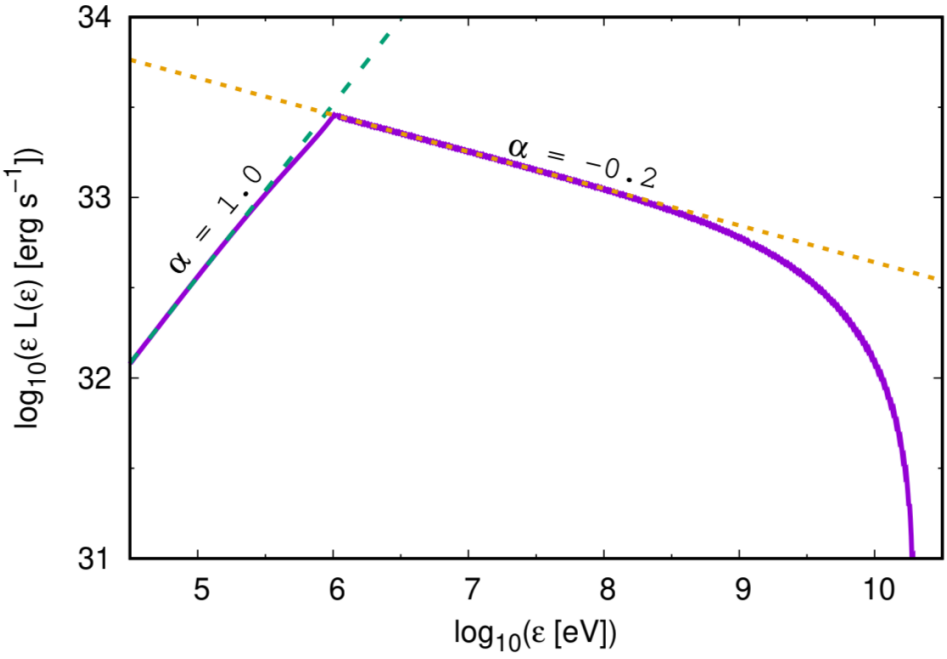

Figure 30: SED generated from a power-law distribution of electrons ($N_e(E_e) \propto E_e^{-2.2}$) in a homogeneous matter field due to bremsstrahlung emission process (Romero, 2021).

$$-\left(\frac{dE_e}{dt}\right)_{\rm Br} = 4n_a Z^2 r_e^2 \alpha c \left[\ln(\gamma_e) + 0.36\right] E_e. \tag{18}$$

Figure 30 shows an example of SED generated from relativistic bremsstrahlung for a power-law electron distribution.

4.1.3 Synchrotron

Many astrophysical sources are magnetized and contain relativistic leptons. The presence of a magnetic field and relativistic particles provides the necessary conditions for the production of synchrotron radiation. This radiation arises due to the Lorentz force, which causes charged particles to gyrate around magnetic field lines. This acceleration causes the emission of electromagnetic radiation in the form of photons.
This kind of motion is represented in Figure 31, where it is also represented the beamed emission with an opening angle of $\sim \frac{1}{\gamma}$. Assuming a power law particle distribution of the form:

$$N(E) = KE^{-p}, \tag{19}$$

where K is a constant and p is the spectral index, the synchrotron spectrum (in this case with units $[\mathrm{s}^{-1}\,\mathrm{cm}^{-3}]$) is given by:

$$P(E_{ph}) = a(p)\frac{4\pi K e^3 B^{\frac{p+1}{2}}}{hmc^2}\left(\frac{3he}{4\pi m^3 c^5}\right)^{\frac{p-1}{2}} E_{ph}^{\frac{-(p-1)}{2}} \tag{20}$$

where B is the magnetic field, h is the Planck constant, E_{ph} is the photon energy and $a(p)$ is a function of the spectral index:

$$a(p) = \frac{2^{\frac{(p-1)}{2}}\sqrt{3}\Gamma(\frac{3p-1}{12})\Gamma(\frac{3p+19}{12})\Gamma(\frac{p+5}{4})}{8\sqrt{\pi}(p+1)\Gamma(\frac{p+7}{4})} \tag{21}$$

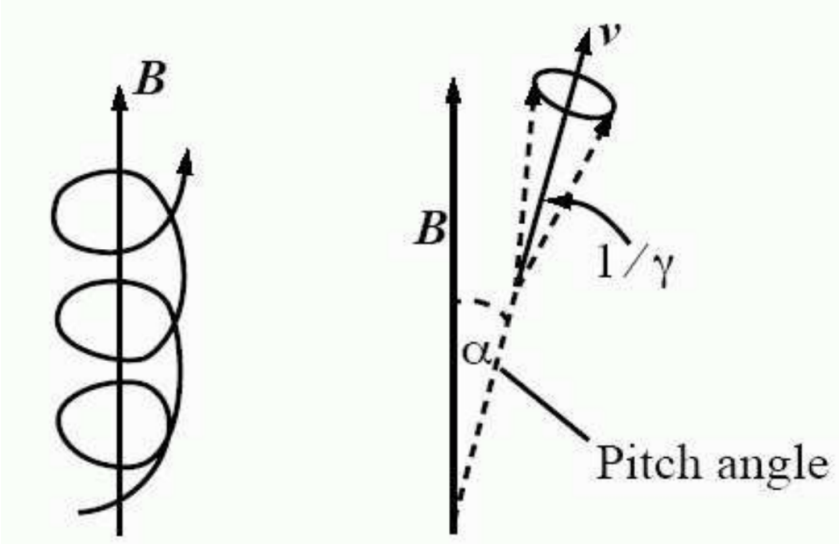

Figure 31: Movement of a particle spiraling around magnetic field lines with a velocity v, Lorentz factor γ, and pitch angle α angle between the particle's velocity vector and the direction of the magnetic field (Romero, 2021).

The spectrum of synchrotron emission is proportional to the photon distribution $P(E_{ph}) \propto E_{ph}^{-\delta}$ where $\delta = (p-1)/2$.
An example of SED generated by synchrotron emission is shown in Figure 32. According to Ghisellini (2013), the synchrotron cooling time of a population of electrons with an isotropic pitch angle distribution, which is connected to the loss of energy as $t_{cool}^{-1} = -\frac{1}{E}\frac{dE}{dt}$, is given by

$$t_{syn} \sim \frac{7.75 \times 10^8}{B^2 \gamma} \tag{22}$$

therefore it is inversely proportional to the squared value of the magnetic field and the Lorentz factor γ, meaning that the stronger the magnetic field the shortest it takes to particles to cool down.

4.1.4 Inverse Compton

When an electron is not at rest and has an energy higher than that of a typical photon, it can transfer part of its energy to the photon through a process known as inverse Compton scattering. This is distinguished from direct Compton scattering, where the electron is initially at rest and gains energy from the photon.
Inverse Compton scattering can occur in two regimes: the Thomson regime and the Klein-Nishina regime. To determine the applicable regime, we consider the reference frame in which the electron is at rest and compute the energy of the incoming photon in this frame. If the photon energy in the electron rest frame is much less than the electron rest mass energy ($m_e c^2$), the interaction occurs in the Thomson regime, where the electron recoil, although always present, is negligible. Conversely, if the photon energy in this frame is comparable to or higher than $m_e c^2$, the scattering occurs in the Klein-Nishina regime, where the recoil of the electron becomes significant and affects the scattering cross section and energy distribution of the scattered photons. Assuming a power law distribution of particles, the emission (in units of $[\mathrm{erg}^{-1}\mathrm{cm}^{-3}\mathrm{s}^{-1}]$) is given by:

$$q_\gamma(E_\gamma) \propto E_\gamma^{-(p+1)/2} \int dE_{ph} E_{ph}^{(p-1)/2} n_{ph}(E_{ph}) \tag{23}$$

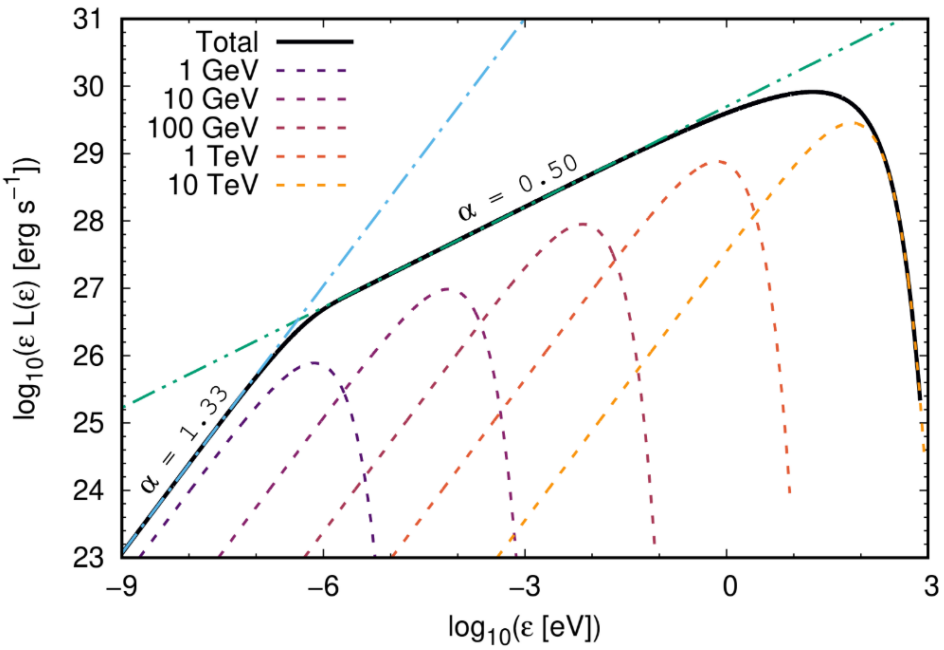

Figure 32: Example of the SED of synchrotron generated from a power law particle distribution with spectral index of 2. In the plot, $L(\epsilon)$ corresponds to $P(E_{ph})$ (Romero, 2021).

Here,

- E_γ is the energy of the upscattered photon, that is, the gamma-ray photon produced by inverse Compton scattering;
- $E_{\rm ph}$ is the energy of the initial (seed) photon before scattering;
- p is the spectral index;
- $n_{ph}(E_{ph})$ is the photon distribution.

Again, from Ghisellini (2013), the cooling time due to inverse Compton in the Thomson regime is:

$$t_{IC} \sim \frac{3m_e c^2}{4\sigma_T c \gamma U_r} \tag{24}$$

with U_r being:

$$U_r = \frac{L}{4\pi R^2 c} \tag{25}$$

where,

- σ_T is the Thomson cross section;
- The quantity $U_{\rm r}$ represents the radiation energy density, expressed in erg cm^{-3}, of the photon field. It quantifies the amount of energy per unit volume stored in the photon field surrounding the electrons within the starburst region of the AGN. This energy density determines the effectiveness of inverse Compton (IC) scattering in cooling the particles, as it sets the energy reservoir available for up-scattering by relativistic electrons;
- R is the radius of the emission region;

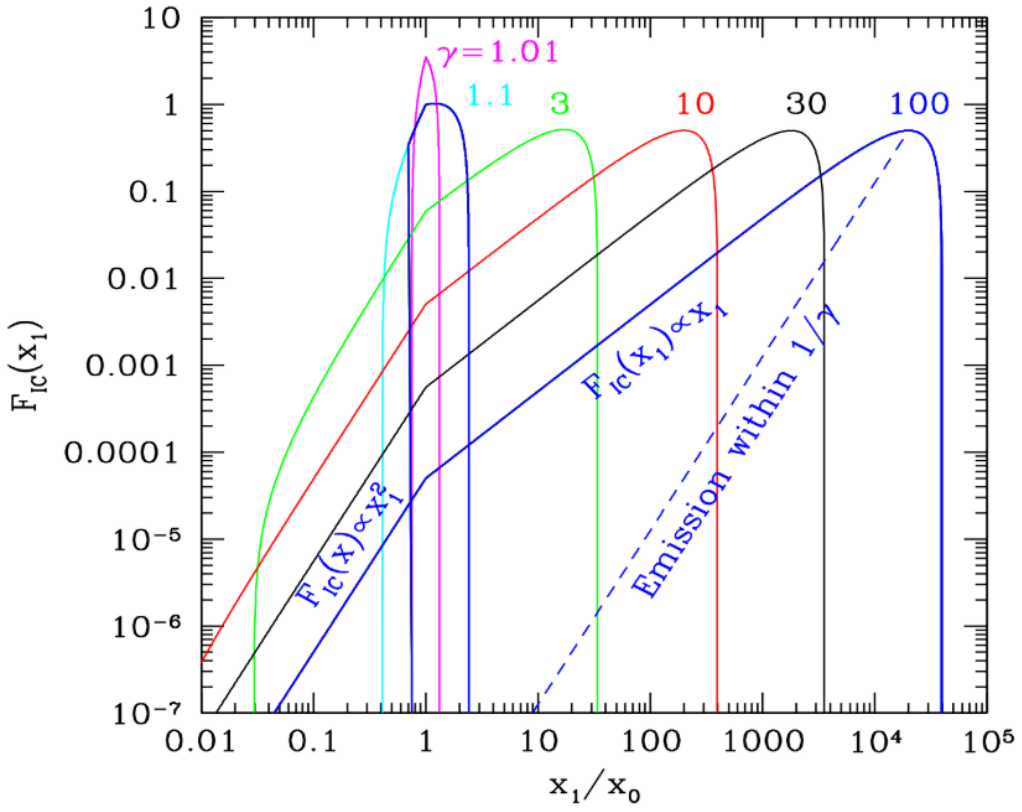

Figure 33: Spectrum emitted by the inverse Compton process by electrons of different γ scattering an isotropic monochromatic radiation field as function of the lab-frame frequency x_1 over dimensionless frequency $x_0 = \frac{x_1}{2\gamma^2}$ ratio (Ghisellini, 2013).

- L is the luminosity of the source.

In Figure 33 an example of SED generated by a distribution of electrons scattered by inverse Compton is shown.

4.1.5 Ionization

When a proton or a nucleus (with charge Ze and mass M) passes through a medium, it interacts primarily with the electrons of the atoms in that material. These interactions cause ionization and excitation of the atoms, which leads to a continuous loss of energy by the incoming particle.
The cooling time for this process can be approximated to:

$$\tau_{ion} \sim 4.8 \times 10^7 (\frac{n}{\mathrm{cm}^{-3}})^{-1} (\frac{E}{\mathrm{GeV}})\mathrm{yr} \tag{26}$$

taken from Thompson and Lacki (2013).

4.1.6 Absorption

High-energy γ-rays produced by relativistic particles in an astrophysical source can be absorbed either within the source itself or along their path to the observer. The main absorption mechanisms include pair production in the Coulomb field of nuclei and photon-photon annihilation,

$$\gamma + \gamma \rightarrow e^+ + e^-, \tag{27}$$

as well as, at very high energies and in the presence of strong magnetic fields, magnetic pair production,

$$\gamma + B \to e^+ + e^-. \tag{28}$$

If the initial intensity of γ-rays is $I_\gamma^0(E_\gamma)$ and the photons traverse a medium of target density n over a distance x, the attenuated intensity is

$$I_\gamma(E_\gamma) = I_\gamma^0(E_\gamma)\, e^{-\tau}, \tag{29}$$

where τ is the optical depth. In general, the optical depth is obtained by integrating the cumulative absorption along the line of sight, and the mean free path of a photon in a uniform medium is $\lambda_\gamma = 1/(\sigma n)$. For pair production in a radiation field, assuming an isotropic distribution of target photons, the optical depth can be expressed as a line-of-sight integral:

$$\tau_\gamma(E_\gamma) = \int_0^R \int_{E_{\rm th}(E_\gamma)}^\infty n_{\rm ph}(E_{\rm ph}, r)\, \sigma_{\gamma\gamma}(E_\gamma, E_{\rm ph})\, dE_{\rm ph}\, dr, \tag{30}$$

where R is the size of the region, $n_{\rm ph}(E_{\rm ph}, r)$ is the photon density at energy $E_{\rm ph}$ and position r, $\sigma_{\gamma\gamma}$ is the $\gamma\gamma$ cross section, and $E_{\rm th} = (m_e c^2)^2/E_\gamma$ is the threshold energy of the target photons.
For the cross section the following approximation is valid(Vila et al., 2009):

$$\sigma_{\gamma\gamma}(s_0) = \frac{3\sigma_T}{2s_0^2}\left[\left(s_0 + \tfrac{1}{2}\ln s_0 - \tfrac{1}{6} + \tfrac{1}{2s_0}\right)\ln\left(\sqrt{s_0} + \sqrt{s_0 - 1}\right) - \left(s_0 + \tfrac{4}{9} - \tfrac{1}{9s_0}\right)\sqrt{1 - \tfrac{1}{s_0}}\right] \tag{31}$$

The parameter

$$s_0 = \frac{E_\gamma E_{\rm ph}}{(m_e c^2)^2} \tag{32}$$

determines the energy of the injected leptons in the center-of-mass frame. Absorption is most efficient when target photons have energies near $E_{\rm th}$, and in compact sources with high photon densities, $\gamma\gamma$ absorption can significantly attenuate the intrinsic γ-ray luminosity, making it an essential effect to include when modeling high-energy emission.

4.2 Transport equation

A population of cosmic rays evolves as a result of interactions with magnetic fields, matter, and radiation, as well as due to transport phenomena such as diffusion and advection.
The population of relativistic particles can be described by the distribution function

$$n(\vec{r}, E, t) = \frac{dN}{dE\, dV}, \tag{33}$$

which represents the number of particles at time t and position $\vec{r}$ per unit volume dV, with energies within the interval dE around E.
The time evolution of this distribution is governed by the transport equation (Ginzburg and Syrovatskii, 1964), given by

$$\frac{\partial n}{\partial t} - \nabla \cdot (D\nabla n) + \frac{\partial}{\partial E}(b\, n) + \frac{n}{T} = Q(E, \vec{r}, t), \tag{34}$$

where $D = D(E, \vec{r})$ denotes the diffusion coefficient, $b = b(E, \vec{r}, t) = dE/dt \leq 0$ is the total energy-loss rate of the particles due to various processes, $T = T(E, \vec{r})$ is the escape timescale of the particles from the region of interest, and $Q(E, \vec{r}, t)$ is the source term describing particle injection.
Equation 34 expresses the balance between the processes that inject and remove particles per unit time and per unit volume in phase space, defined by position (and possibly direction of motion) and energy. The second term on the left-hand side represents spatial transport of particles via diffusion.
The third term accounts for continuous energy losses, that is, interactions producing small changes in the particle energy compared to its initial value. The function b represents the total energy-loss rate; if several (N) cooling processes act on the particles, then b is given by the sum of the individual energy-loss rates:

$$b(E, \vec{r}, t) = \sum_{i=1}^{N} b_i = \sum_{i=1}^{N} \left(\frac{dE}{dt} \right)_i \tag{35}$$

The fourth term on the left-hand side describes the escape of particles from the region of interest. In this context, T represents the escape timescale, which may effectively include escape by convection or diffusion. If the particles are unstable, this term can also account for their disappearance by decay.
Finally, the right-hand side term corresponds to the source term, encompassing all phenomena that inject particles into the region of interest. For instance, injection by an acceleration mechanism can be incorporated through an appropriate choice of the injection function.

4.3 Model description and assumptions

The model that we realized is based on the following assumptions:

- To explain the observed neutrino and gamma-ray spectra, we decide to adopt a model based on the model of Eichmann et al. (2022). Some studies have shown that it is difficult to explain the gamma-ray emission of this galaxy and its neutrino emission with a one-zone model (Yoast-Hull et al., 2013; Eichmann and Tjus, 2016). However, there is general agreement that the gamma-ray emission observed in the Fermi band is produced by the star-forming component (Eichmann et al., 2022). For the sake of simplicity, we will consider only the starburst component of this galaxy and calculate its multiwavelength emission spectrum. In the chapter 6, we will discuss how the additional contribution from the AGN component would affect our results;

- When solving the transport equation in our model, we consider the simple case of a particle system in a stationary state, within a homogeneous region, where particle escape is negligible. Peretti et al. (2019) and Kornecki et al. (2020, 2022) applied this simplified model to SFGs and starburst regions, and their results are also consistent with observations. They found that the escape in galaxies with high SFR is not expected to have a significant impact.
  Let us consider a region where relativistic particles are injected with a spectrum of the form

$$Q(E) = KE^{-p}, \quad p > 0. \tag{36}$$

The equation 34 for $n(E)$ becomes

$$\frac{d}{dE}\left[b(E)\, n(E)\right] = Q(E). \tag{37}$$

For $p \neq 1$, and assuming that $b(E)n(E) \to 0$ as $E \to \infty$, the solution becomes

$$n(E) = \frac{K}{p-1}\, E^{-(p-1)}\, \frac{1}{|b(E)|}. \tag{38}$$

- In the case of the modeling of the hadronic population, we assume a constant cooling time for what concerns the pion decay;
- From the work of Kornecki et al. (2022), the ratio between the injection rate of protons and the one of electrons is:

$$\frac{Q_{0,p}}{Q_{0,e}} = 50. \tag{39}$$

- Eichmann et al. (2022) consider the emitting region as ring-shaped. We approximated the region as a cylinder with a volume equivalent to the one of the ring.
- When modeling the inverse Compton, we consider only the Far-IR photon field and we approximate it as a black body of $T = 20K$ (Kornecki et al., 2020);
- When we model the absorption we consider two main issues:
  1. NGC 1068 is almost face on, so the medium that needs to be crossed by the particles is equivalent to the height of the cylinder we considered as a starting point;
  2. when we model the absorption, we consider the attenuation of gamma-ray emission within an absorbing medium of cylindrical geometry, as represented in Figure 34. The total volume of the cylinder is expressed as:

$$V = \pi R^2 h \tag{40}$$

and the infinitesimal contribution from a thin slice of thickness dz is given by

$$dV = \pi R^2 dz \tag{41}$$

Assuming that the total intrinsic luminosity L is homogeneously distributed throughout the volume, the fraction of luminosity associated with this slice is proportional to its relative volume, yielding

$$dL = \frac{L}{V} dV = L\frac{dz}{h} \tag{42}$$

The surviving intensity is reduced by a factor of $e^{-\alpha z}$, where α is the linear absorption coefficient, such that the observable contribution becomes

$$dL_{obs} = dLe^{-\tau} = dLe^{-\alpha z} \tag{43}$$

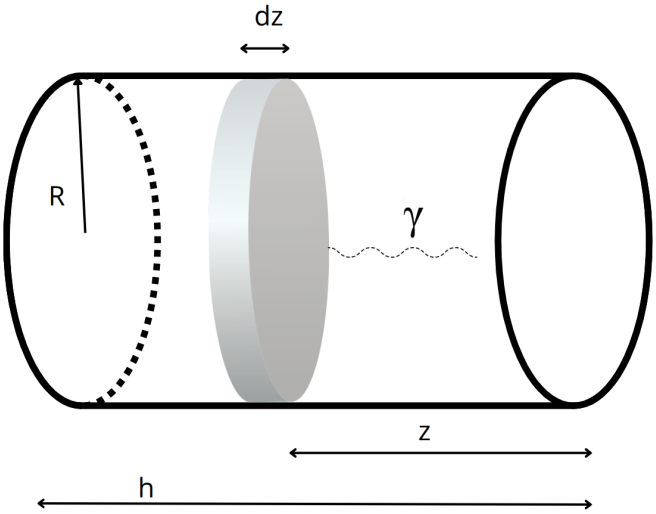

Figure 34: Schematic representation of gamma-ray absorption in a uniformly emitting cylindrical medium. The cylinder has radius R and height h, and is divided into differential slices of thickness dz. Each slice contributes a fraction of the total luminosity, but the photons emitted at a depth z are attenuated by a factor $e^{-\alpha z}$ as they cross the material. The integration of these contributions over the entire height yields the observed luminosity.

The total observed luminosity at the boundary of the cylinder is then obtained by integrating these contributions over the full height of the medium,

$$L_{obs} = \int_0^h dL_{obs} = \int_0^h Le^{-\alpha z}\frac{dz}{h} = L\frac{1}{\alpha h}\, e^{-\alpha z}\Big|_0^h \tag{44}$$

Carrying out the integration leads to the compact expression

$$L_{obs} = L\frac{1}{\alpha h}(1 - e^{-\alpha z}) = L(\frac{1 - e^{-\tau}}{\tau}) \tag{45}$$

where the dimensionless parameter $\tau = \alpha h$ denotes the total optical depth of the cylinder. For optically thin media ($\tau \ll 1$), attenuation is negligible and nearly the entire luminosity is detectable ($L_{\rm obs} \approx L$), while for optically thick media ($\tau \gg 1$), only a fraction of the order L/τ emerges, as most of the emission from deeper layers is exponentially suppressed.

- The star formation rate of the galaxy is assumed to be $22.7 \pm 8.1 M_{\odot} yr^{-1}$ (Kornecki et al., 2020).

In order to compute the complete model, we made use of the `naima` package (Zabalza, 2015).
`naima` takes as input the particle distribution amplitude (number of particles per unit of energy), which is calculated separately for protons and electrons.
In the case of protons, we start from the proton (cosmic-ray) luminosity defined as the energy integral of the injection function (Kornecki et al., 2020):

$$L_{\rm CR} = \int_{E_{\rm min}}^{E_{\rm max}} E\, Q_p(E)\, dE. \tag{46}$$

Assume a power-law injection spectrum

$$Q_p(E) = k_{pr} \left(\frac{E}{E_0} \right)^{-p}, \tag{47}$$

where k_{pr} is the normalization E_0 is a reference energy, and p is the spectral index. Substitute Q_p into the integral:

$$L_{\rm CR} = k_{pr} \int_{E_{\rm min}}^{E_{\rm max}} E \left(\frac{E}{E_0} \right)^{-p} dE = k_{pr} E_0^p \int_{E_{\rm min}}^{E_{\rm max}} E^{1-p}\, dE. \tag{48}$$

Evaluate the power-law integral (for $p \neq 2$):

$$\int_{E_{\rm min}}^{E_{\rm max}} E^{1-p}\, dE = \frac{E^{2-p}}{2-p}\bigg|_{E_{\rm min}}^{E_{\rm max}} = \frac{E_{\rm max}^{2-p} - E_{\rm min}^{2-p}}{2-p}. \tag{49}$$

Therefore

$$L_{\rm CR} = k_{pr} \cdot \frac{E_{\rm max}^{2-p} - E_{\rm min}^{2-p}}{2-p}. \tag{50}$$

Solve for the normalization k_{pr}:

$$k_{pr} = L_{\rm CR} \cdot \frac{2-p}{E_{\rm max}^{2-p} - E_{\rm min}^{2-p}}. \tag{51}$$

The number of particles is given by:

$$N_{\rm pr}(E) = \frac{1}{b} \int_{E}^{E_{\rm max}} k_{pr} (\frac{E'}{E_0})^{-p}\, dE', \tag{52}$$

where the parameter b in this case depends solely by the Pion Decay cooling time, being the only process we consider for the hadronic component :

$$b = \frac{E}{t_{cool,PD}} \tag{53}$$

In the case of electrons it has been calculated in the following way:

$$b = \frac{E}{t_{\rm cool}} \tag{54}$$

where b is the energy loss rate. t_{cool} is given by the sum of the inverse of every process involved (inverse Compton, bremsstrahlung, synchrotron and ionization):

$$t_{\rm cool} = \frac{1}{t_{\rm syn}^{-1} + t_{\rm IC}^{-1} + t_b^{-1} + t_{{\rm ion},e}^{-1}} \tag{55}$$

We assume electrons are injected with a power-law distribution:

$$Q(E) = k_{\rm el} \left(\frac{E}{E_0} \right)^{-p} \tag{56}$$

Here:

- k_{el} is the normalization constant,
- E_0 is a reference energy,
- p is the spectral index.

In steady state, the number of particles at energy E results from the balance between injection and energy losses. The general solution is:

$$N_{\mathrm{el}}(E) = \frac{1}{b} \int_{E}^{E_{\max}} Q(E')\, dE'. \tag{57}$$

5 Results

In this chapter, we present the results of our modeling. We begin by introducing the initial set of parameters and discussing the corresponding results, including the cooling times, particle distributions, and the resulting SED. Next, we show the outcomes of the parameter-space exploration, remaining within the ranges of values reported in the literature from previous studies. Finally, we present the best set of parameters obtained from our model and compare them with both literature data and the results previously obtained from LST-1. Moreover, we compare our model predictions with the sensitivities of future ground- and space-based instruments, to assess what can be expected from upcoming observations.

5.1 Results with the benchmark parameters

In this section, we test the physical model and explore its dependence on the free parameters. To compute the proton and electron distributions, we built a numerical code in Python following the procedure described in Section 4.3. For the calculation of the non-thermal emission, we used the Python package `naima`, which includes non-thermal radiative processes such as synchrotron, inverse Compton, Bremsstrahlung, and pion production through pp interactions. As a starting point, we adopt the average physical values from the literature, which are representative of the astrophysical environment under study. In particular, referring to Eichmann et al. (2022) and Kornecki et al. (2020), we consider the set of parameters summarized in Table 2. They provide the baseline conditions for evaluating the relevant radiative and collisional processes. In particular they are: the spectral index of the injection function s, the magnetic field B, the gas density $n_{\rm gas}$, the injection efficiency ϵ_{inj} and the height of the absorption region h.
The benchmark parameters were selected based on a review of the literature, representing average values across the reported ranges. Moreover, these parameters were selected either because they represent the main dependencies of the cooling times for certain processes (e.g., B and $n_{\rm gas}$), have a significant impact on the particle distribution (e.g., s), strongly influence the total SED (e.g., ϵ_{inj}), and can be useful for setting constraints (e.g., h).
Based on these parameters, we compute the characteristic cooling timescales for both hadronic and leptonic populations, represented in Figure 35. For the hadronic component, we evaluate the energy losses due to Pion production (via proton-proton collisions) and Ionization. For the leptonic component, we consider the dominant processes of inverse Compton, bremsstrahlung, synchrotron radiation, and Ionization. These cooling timescales allow us to determine which processes dominate the overall energy budget and emission at different energy ranges.
After, we solved the transport equation, obtaining the distributions for protons and electrons (in Figure 37), whose shapes and values are affected by the most important process (the ones with the smaller cooling time) at different energy ranges.
For both protons and electrons, the injected particle distribution follows a power law. As shown in the distribution plots, the proton distribution ultimately maintains the same power-law form and spectral index as the injection function. This occurs because the final proton distribution is primarily influenced by pion decay, which is characterized by a constant cooling time and therefore does not alter the shape of the original power-law distribution. The resulting spectrum exhibits a cut-off corresponding to the maximum

proton energy ($\sim 10^{16}$ eV).
The case of electrons is slightly more complex due to the larger number of physical processes involved. These processes produce a cooling function, $t_{\rm cool}$, that is more intricate than the constant one found for protons. Consequently, the resulting electron distribution is described by a broken power law. At lower energies ($\sim 10^6$–10^9 eV), the original power law experiences significant energy losses dominated by ionization, resulting in an increasing behavior. Beyond 10^9 eV, the distribution decreases again until it reaches the cut-off at $\sim 10^{13}$ eV, corresponding to the maximum electron energy.
To conclude, we present the SED obtained from the model evaluated using the benchmark parameters, including the contribution from each individual process as well as the total curve (Figure 38).

Table 2: Benchmark parameters for NGC 1068.

Parameter	**Value**
Spectral index, (s)	2.2
Gas density, ($n_{\rm gas}$)	500 cm^{-3}
Magnetic field, (B)	250 μG
Injection efficiency, ($\epsilon_{\rm inj}$)	0.1
Height of the absorption region , (h)	300 pc

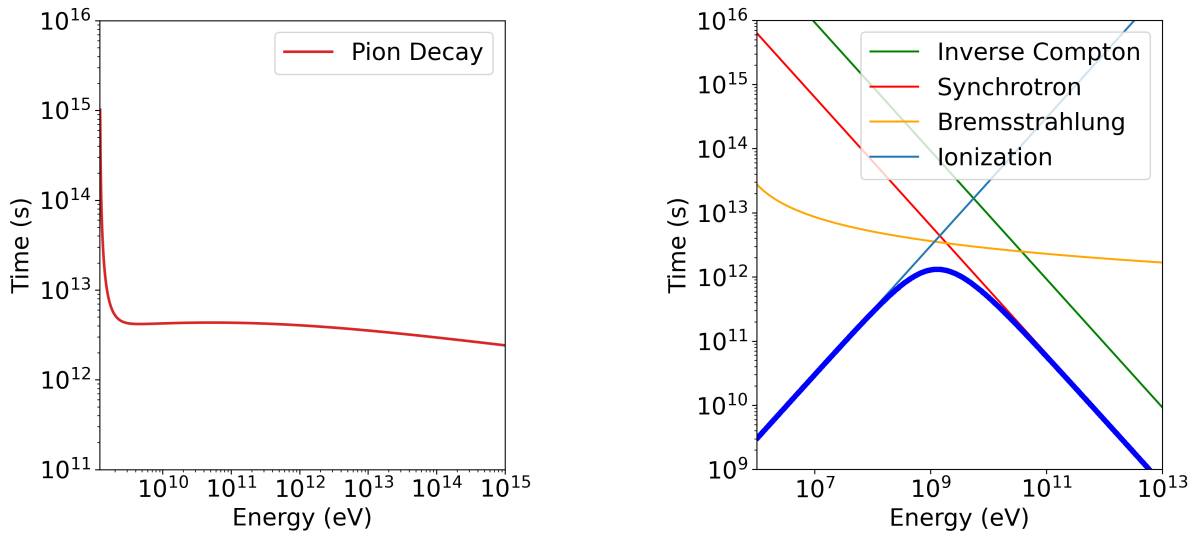

(a) (b)

Figure 35

Figure 36: Cooling times as function of energy for (a) protons and (b) electrons calculated using the benchmark values.

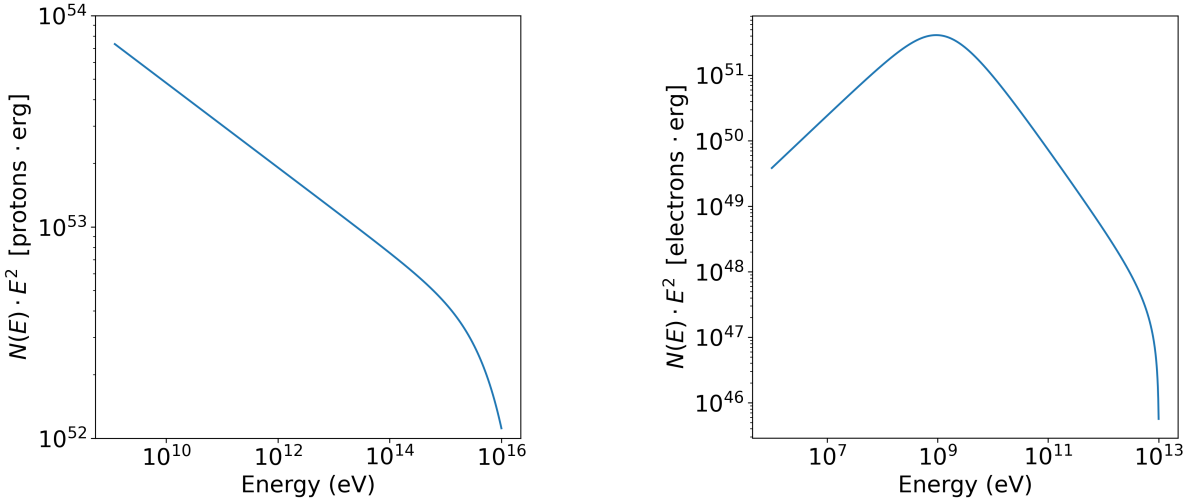

(a) (b)

Figure 37: Particles distributions obtained after solving the transport equation for protons (a) and electrons (b), using the benchmark parameters.

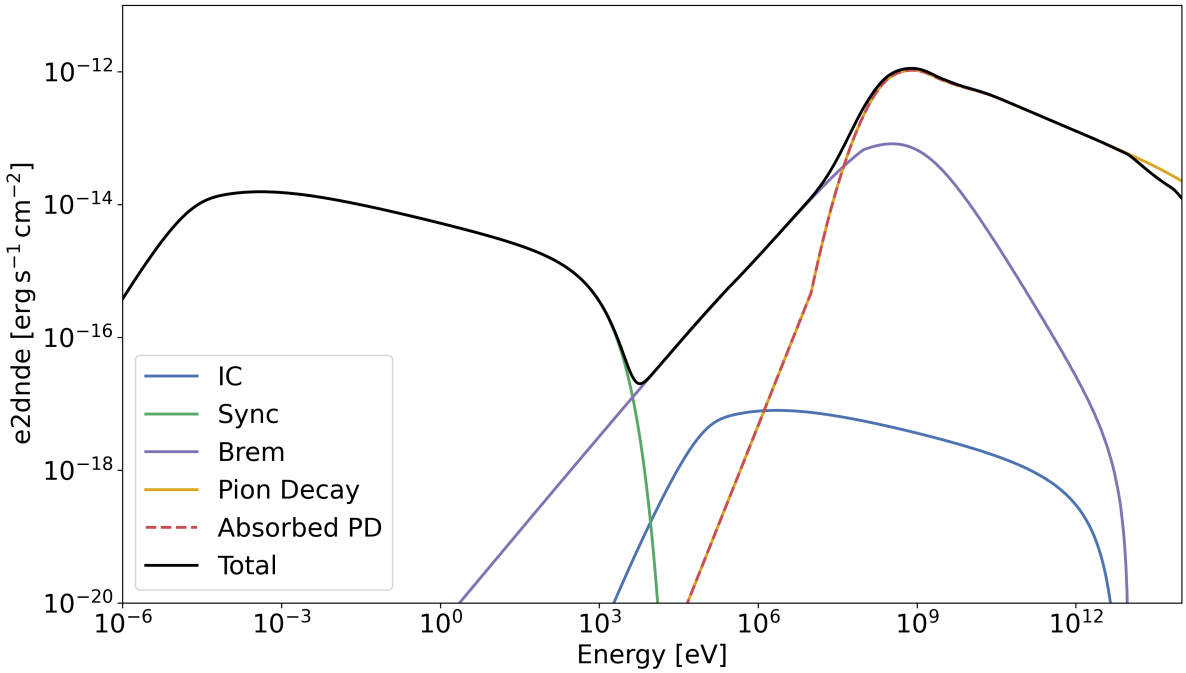

Figure 38: SED of NGC 1068 obtained from the benchmark parameters, including the contribution of every process.

5.2 Exploration in the space of parameters

Here we present the parameter-space exploration, illustrating how each individual physical process responds to variations of a single parameter. The goal is to identify the optimal combination of parameters that allows the model to reproduce the observed data as accurately as possible.

For comparison, the total SED is also shown in each case. Regarding the hadronic processes, only the absorbed pion decay component is displayed, in order to simplify the interpretation and focus on the most relevant contribution to the overall emission.

The parameter exploration was performed by varying each free parameter introduced in Section 5.1 within the ranges of values reported in literature (Kornecki et al., 2020; Eichmann et al., 2022). These intervals are summarized in Table 3, which also includes additional parameters used in the model but kept fixed during the process. All parameter values were selected to remain physically consistent with previous studies.

Table 3: The set of parameters that characterize the starburst region of NGC 1068 (Eichmann et al., 2022; Kornecki et al., 2020).

Parameter	**Value**
Spectral index, (s)	1.5–2.5
Gas density, (n_{gas})	10–1000 cm^{-3}
Magnetic field, (B)	10–500 μG
Radius, (R)	970.8 pc
Infrared luminosity, (L_{IR})	$1.5 \times 10^{11}\, L_{\odot}$
Star formation rate, (SFR)	$22.7\, M_{\odot}\, \mathrm{yr}^{-1}$
Injection efficiency, (ϵ_{inj})	0.02–0.3
height of the absorption region, (h)	150–600 pc

The **first variation** concerns the magnetic field B, while the other parameters are kept fixed.
In Figure 39 we can observe how the change of the parameter B affects the leptonic processes (synchrotron, inverse Compton, and bremsstrahlung). This can be explained as the cooling time of the synchrotron depends on B ($t_{\mathrm{syn}} \propto B^{-2}$) which directly affects the leptonic particle distribution, hence all the leptonic particle distribution will change according to B. The SED of the hadronic processes (pion decay and absorbed pion decay) stays constant for different values of B since they have no dependence on the magnetic field.
In Figure 40 the total curve is shown. The overall model changes only in the lower energy range associated with the synchrotron emission, while at higher energies, bremsstrahlung, inverse Compton and pion decay are present, the model remains the same since the absorbed pion decay contributes more.
In this case, we can directly exclude low values of B, as it would make the resultant synchrotron contribution too small. On the other hand, it is evident that the difference between $B = 250\,\mu$G and $B = 500\,\mu$G is not that big.

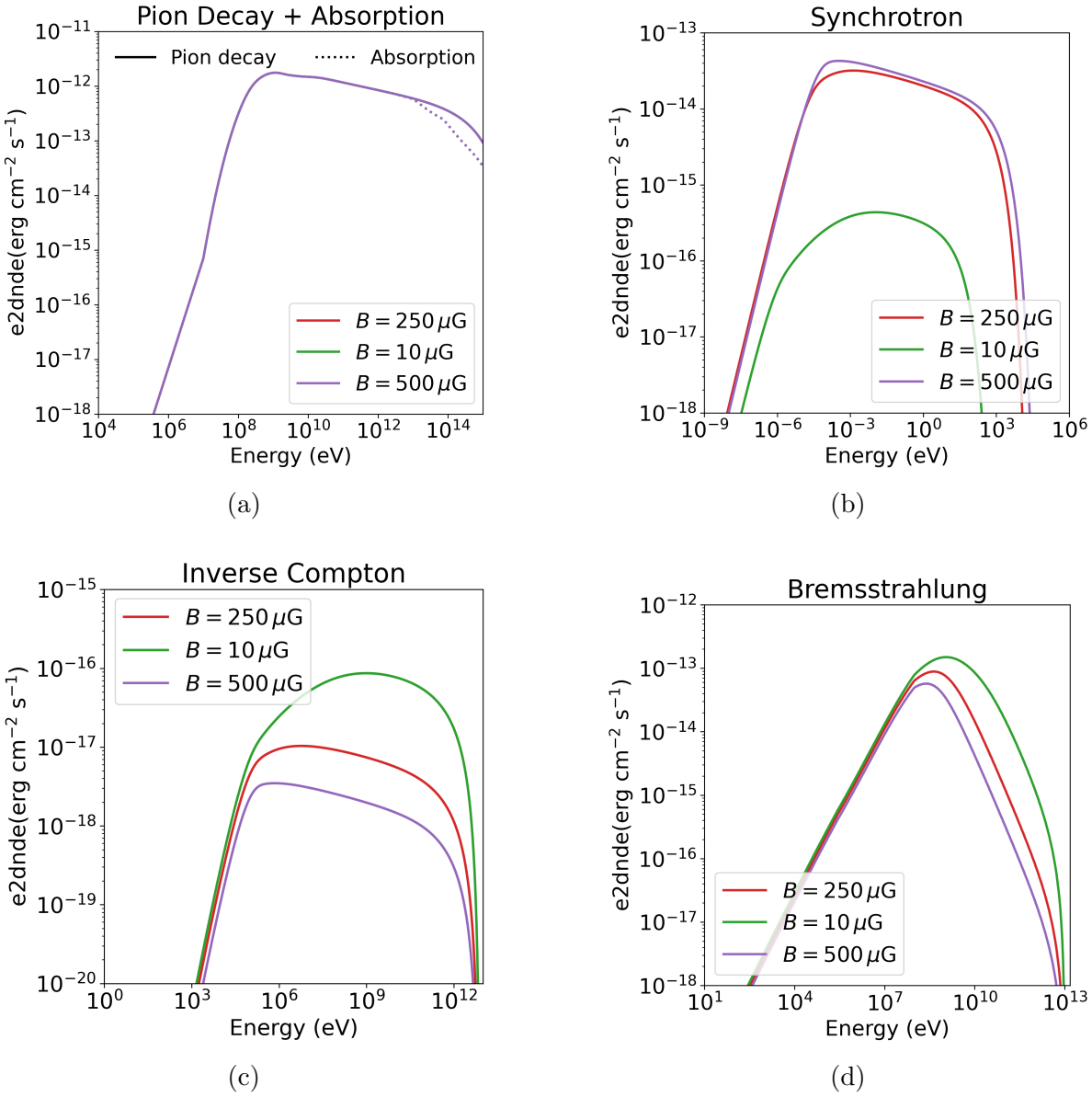

Figure 39: SEDs for different emission processes as a function of energy, shown for three magnetic field strengths: $B = 10\,\mu$G, $B = 250\,\mu$G, and $B = 500\,\mu$G. The panels display (a) normal and absorbed pion decay, (b) synchrotron emission, (c) inverse Compton scattering, and (d) bremsstrahlung. Each curve illustrates how the corresponding process varies with changes in the magnetic field.

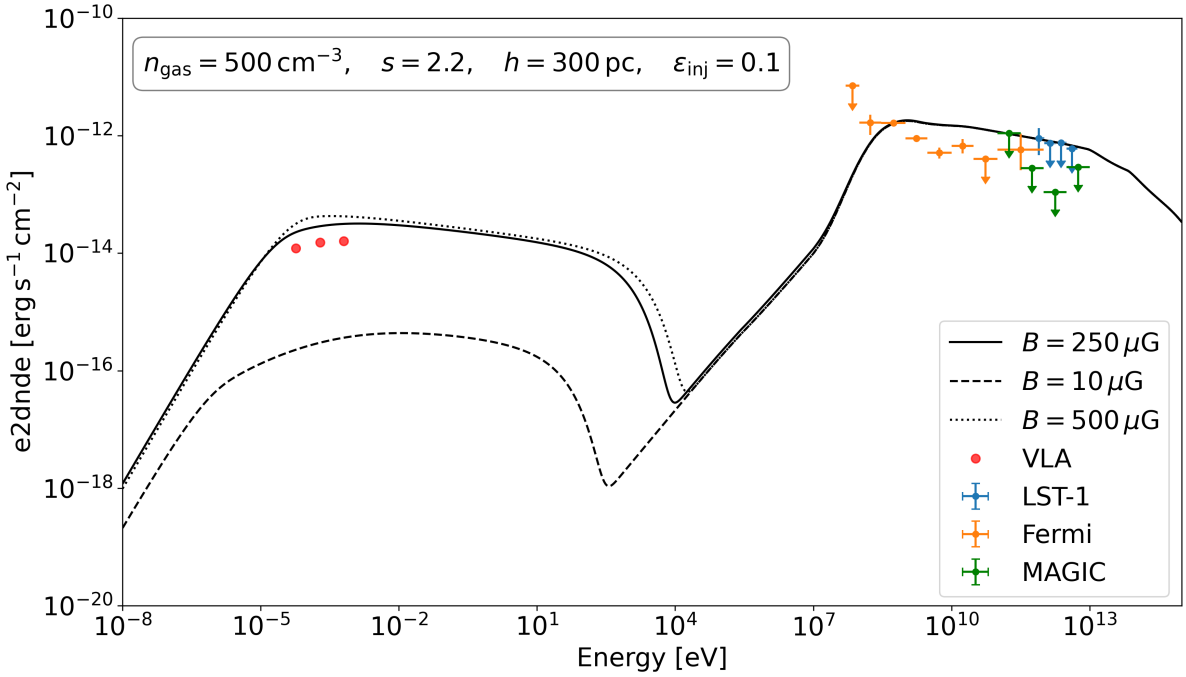

Figure 40: Total SED for NGC 1068 obtained varying the value of the magnetic field B between 10 μG and 500 μG, and keeping particle density n_{gas}, spectral index s, height of the absorption region h and injection efficiency ϵ_{inj} fixed.

The **second variation** involves the gas density. When analyzing each process, we observe (Figure 41) that, although both particle distribution and proton SED depend on n_{gas}, variations in this parameter do not affect the shape of the SED itself, due to the fact that the average lifetime of a pion is so short ($\sim 10^{-17}$) that it cannot interact with the matter, so the SED is not dependent on environmental changes.
In this case, synchrotron and inverse Compton show the same behavior: the SED increases for decreasing density, while the bremsstrahlung contribution increases for higher n_{gas} values. The explanation is straightforward: while the bremsstrahlung emission increases with gas density due to the higher number of target nuclei, synchrotron and inverse Compton emissions behave oppositely, rising at lower gas densities because electrons lose less energy to collisions and thus more energy is available for radiation in magnetic and photon fields.
In Figure 42 the total curve gets slightly affected at $\sim 10^{-5}$ eV, in correspondence with the lower energy tail of the synchrotron curve, and between 10^4 and 10^7 eV, where the contribution of both inverse Compton and bremsstrahlung is dominant. From the plot, we evince that the most likely value for the gas density is in the higher range, as it seems to reproduce better the VLA data.

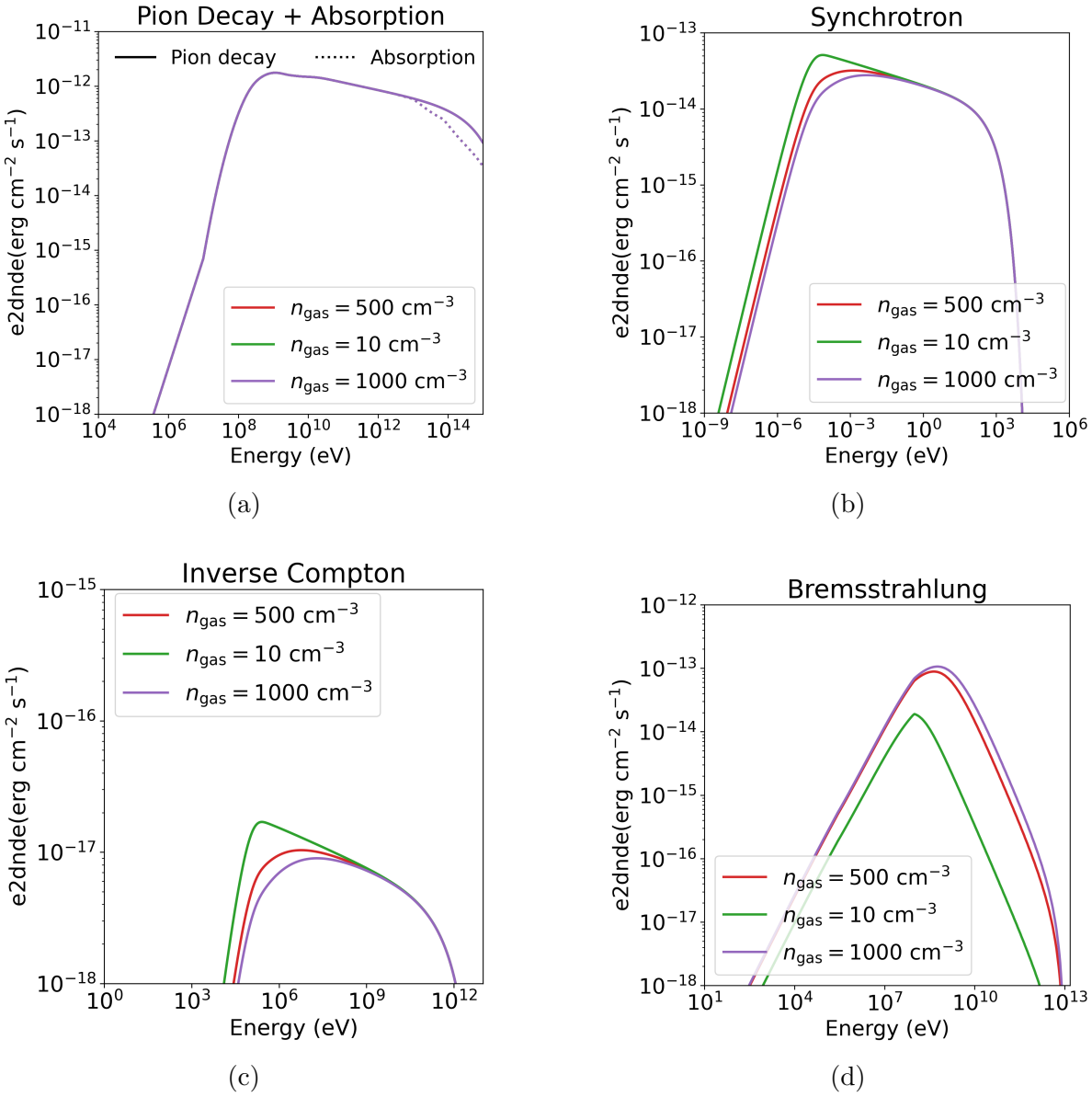

Figure 41: SEDs for different emission processes as a function of energy, shown for three particle densities: $n_{gas} = 10\,\mathrm{cm}^{-3}$, $n_{gas} = 500\,\mathrm{cm}^{-3}$, and $n_{gas} = 1000\,\mathrm{cm}^{-3}$. The panels display (a) normal and absorbed pion decay, (b) synchrotron emission, (c) inverse Compton scattering, and (d) bremsstrahlung. Each curve illustrates how the corresponding process varies with changes in the gas density.

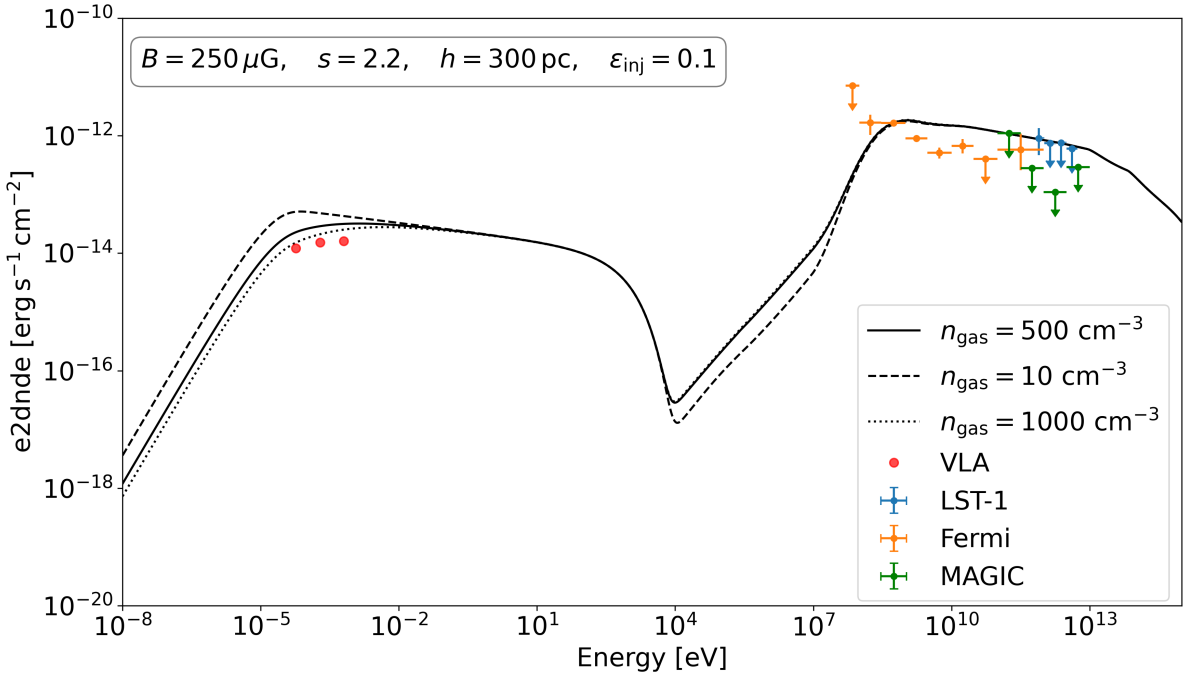

Figure 42: Total SED for NGC 1068 obtained varying the value of the particle density $n_{\rm gas}$ between 10 cm^{-3} and 1000 cm^{-3}, and keeping magnetic field B, spectral index s, height of the absorption region h and injection efficiency ϵ_{inj} fixed.

The **third variation** concerns the spectral index s of the injection function (Equation 36). In this case, every single process' SED (Figure 43) changes drastically when changing the value of this parameter. The reason is that any variation in the injection function, expressed as a power law characterized by the spectral index s, leads to changes in both the hadronic and leptonic particle distributions, ultimately influencing the contribution of all the involved processes. In Figure 44, the whole model at every energy range is altered with the variation of the spectral index. At first sight, we can directly exclude the hypothesis of a spectral index s = 1.5 as it produces a behavior of the curve in the energy range between $\sim 10^8$ and $\sim 10^{13}$ eV completely opposite to the data.

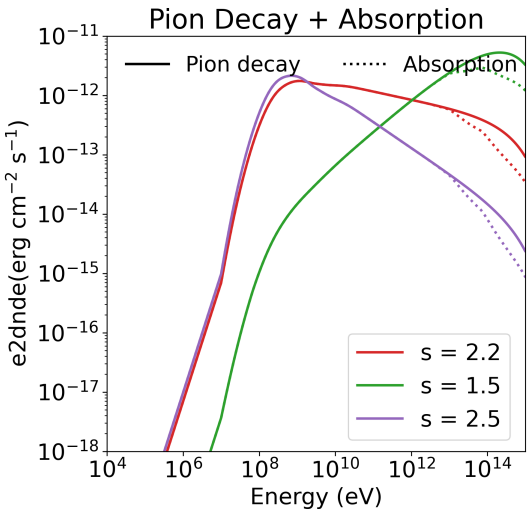

(a)

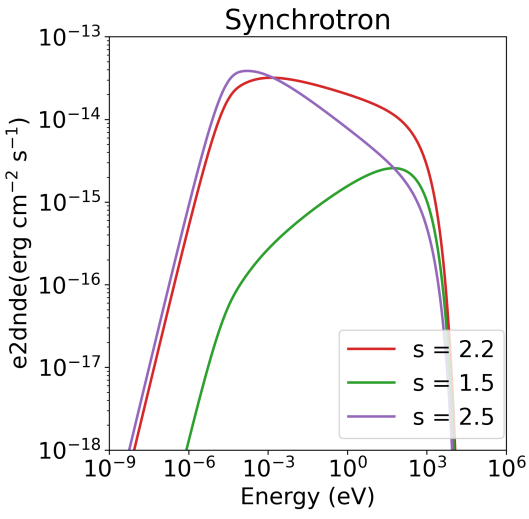

(b)

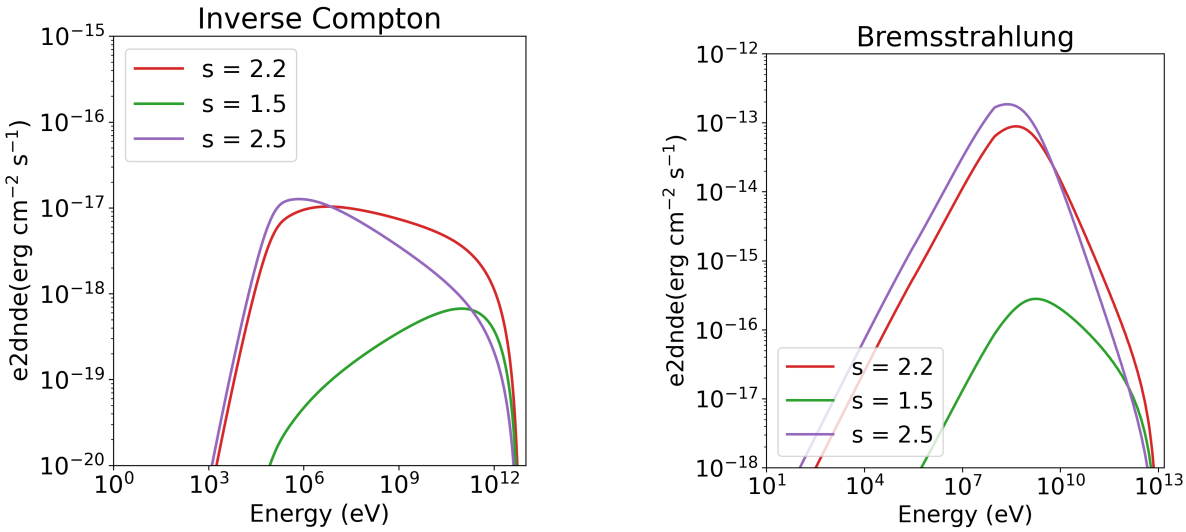

(c) (d)

Figure 43: SEDs for different emission processes as a function of energy, shown for three spectral indices: $s = 1.5$, $s = 2.2$, and $s = 2.5$. The panels display (a) normal and absorbed pion decay, (b) synchrotron emission, (c) inverse Compton scattering, and (d) bremsstrahlung. Each curve illustrates how the corresponding process varies with changes in the spectral index of the injection function.

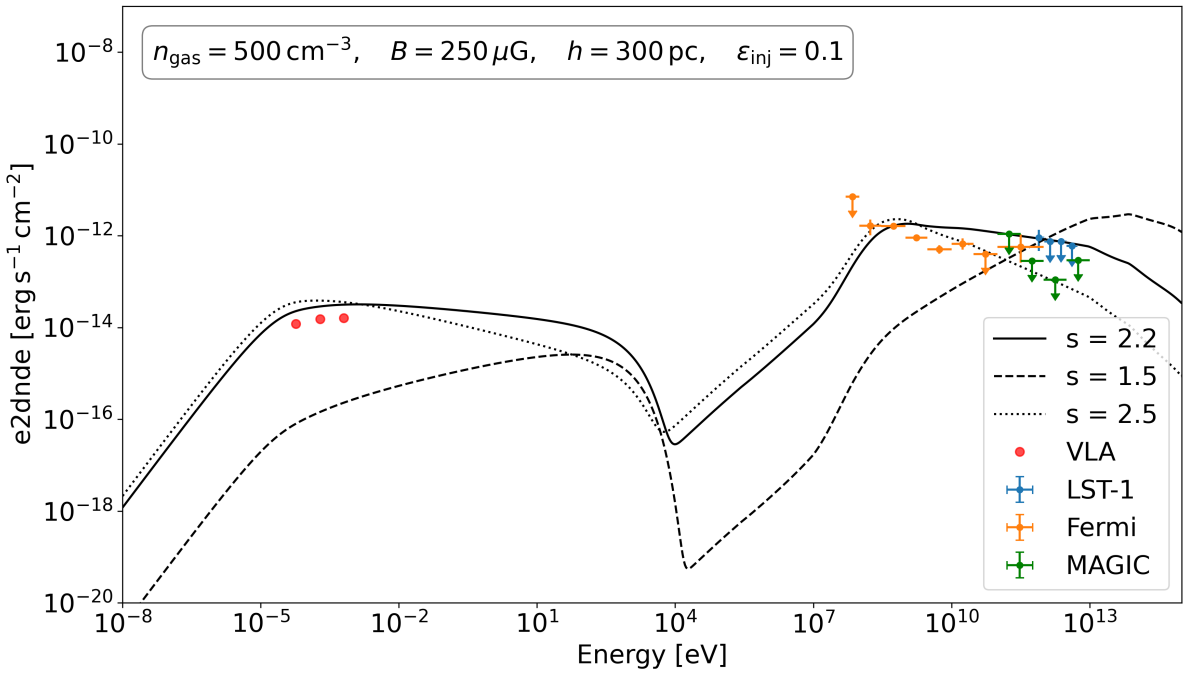

Figure 44: Total SED for NGC 1068 obtained varying the value of the spectral index s between 1.5 and 2.5, and keeping magnetic field B, particle density $n_{\rm gas}$, height of the absorption region h and injection efficiency ϵ_{inj} fixed.

The **fourth variation** is about the injection efficiency ϵ_{inj}. As can be noted both for every single process in Figure 45 and for the whole model in Figure 46, this parameter has the only effect to either increase or decrease the normalization of the SED, without modifying the shape of it. This occurs because $\epsilon_{\rm inj}$ controls the number of particles injected into the system; increasing it raises the total number of radiating particles,

enhancing the overall emission, while decreasing it reduces the emission. However, since the energy distribution of the particles and the physics of the radiation processes remain unchanged, the shape of the SED is unaffected, and only its normalization varies.
From the complete SED, we can exclude an efficiency of 0.3 which is likely unphysical, since it brings the normalization to a value which is too high.

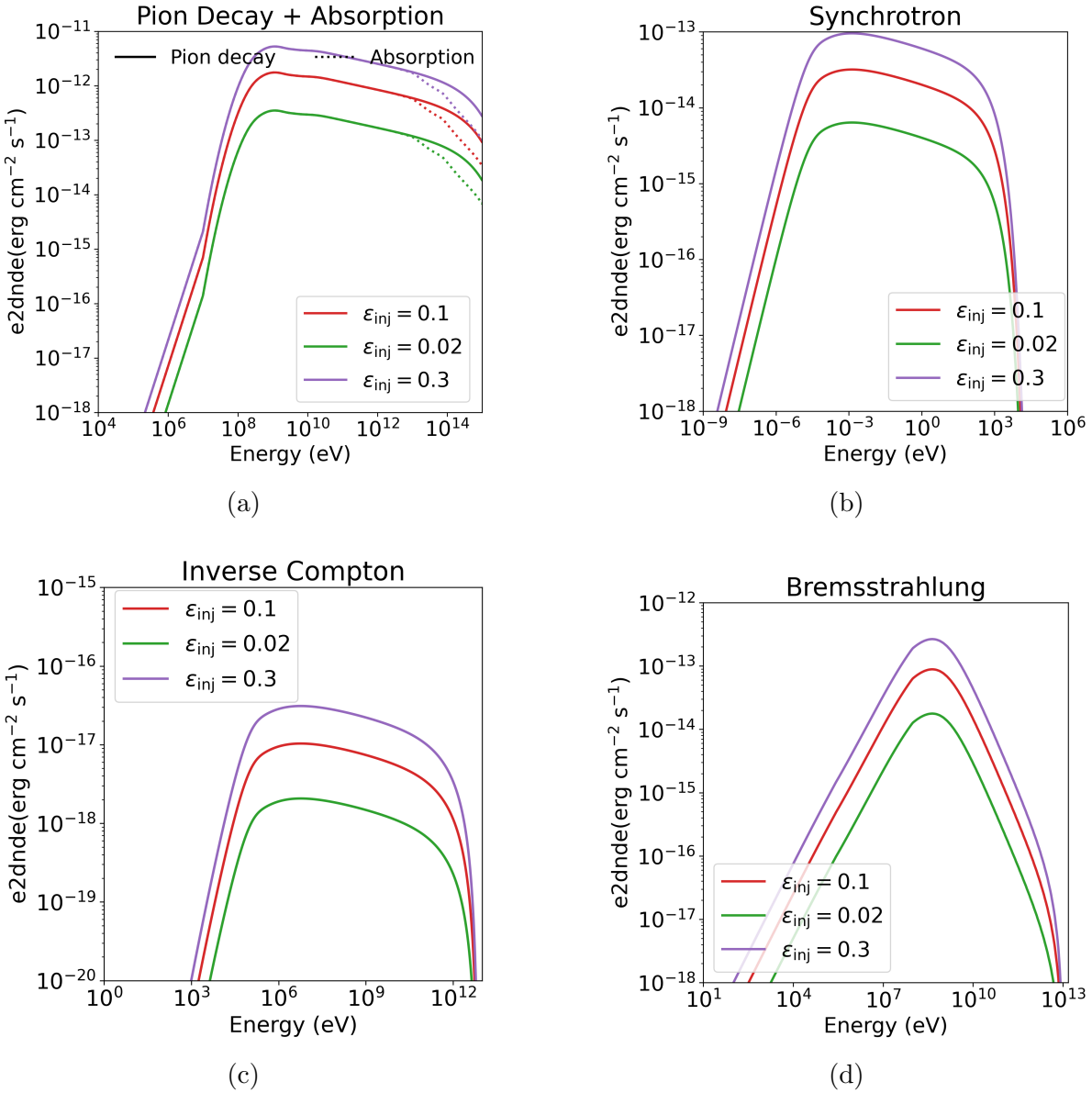

Figure 45: SEDs for different emission processes as a function of energy, shown for three injection efficiencies: $\epsilon_{inj} = 0.02$, $\epsilon_{inj} = 0.1$, and $\epsilon_{inj} = 0.3$. The panels display (a) normal and absorbed pion decay, (b) synchrotron emission, (c) inverse Compton scattering, and (d) bremsstrahlung. Each curve illustrates how the corresponding process varies with changes in the injection efficiency.

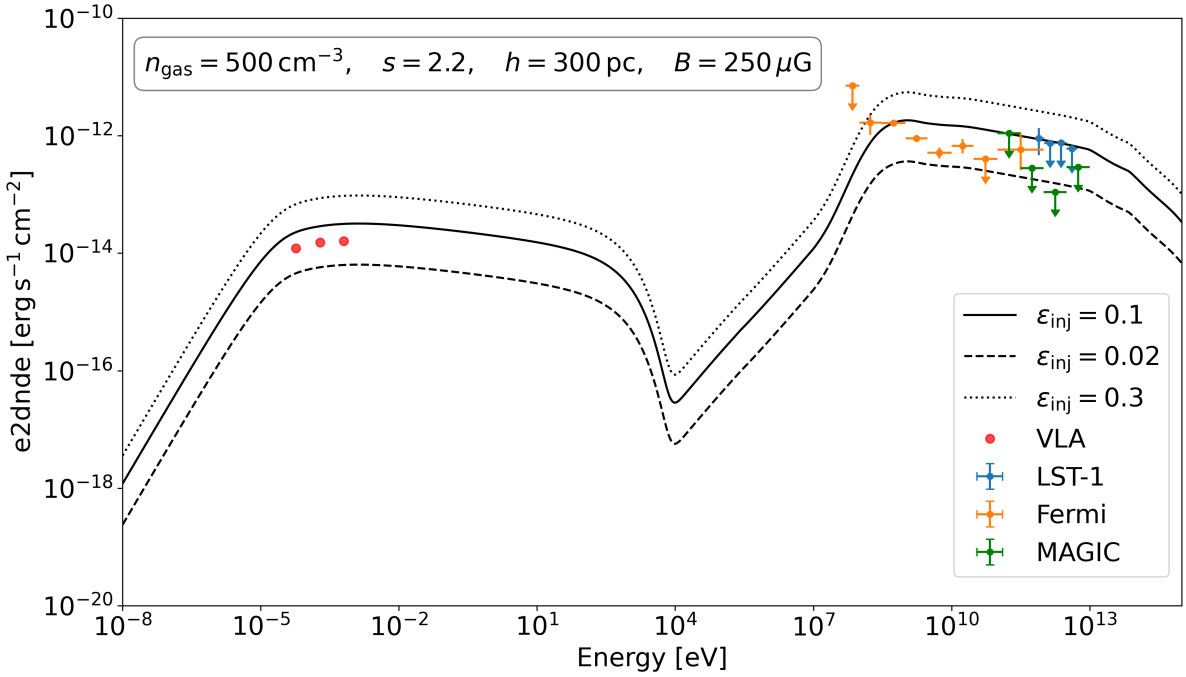

Figure 46: Total SED for NGC 1068 obtained varying the value of the injection efficiency ϵ_{inj} between 0.02 and 0.3, and keeping particle density $n_{\rm gas}$, spectral index s, height of the absorption region h and magnetic field B fixed.

The **last variation** is about the height of the absorption region h, which represents the size of the region through which the gamma rays travels and get absorbed. For this reason, the only process affected is the absorption shown in Figure 47, producing a steeper cut-off for increasing values of h. All the other processes are not influenced by this parameter variation.
This variation produces a general curve (Figure 48) with noticeable changes only above $\sim 10^{13}$ eV. While the lack of data prevents us from having strong constraints in this range, the result provides valuable insight into the model behavior at very high energies and helps characterize the IR field absorption in this galaxy.

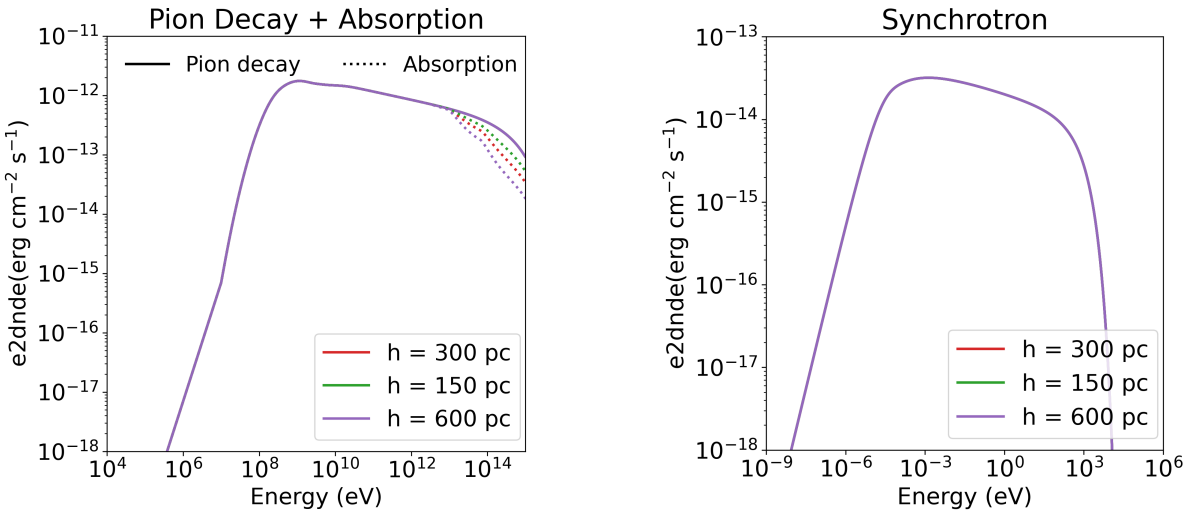

(a) (b)

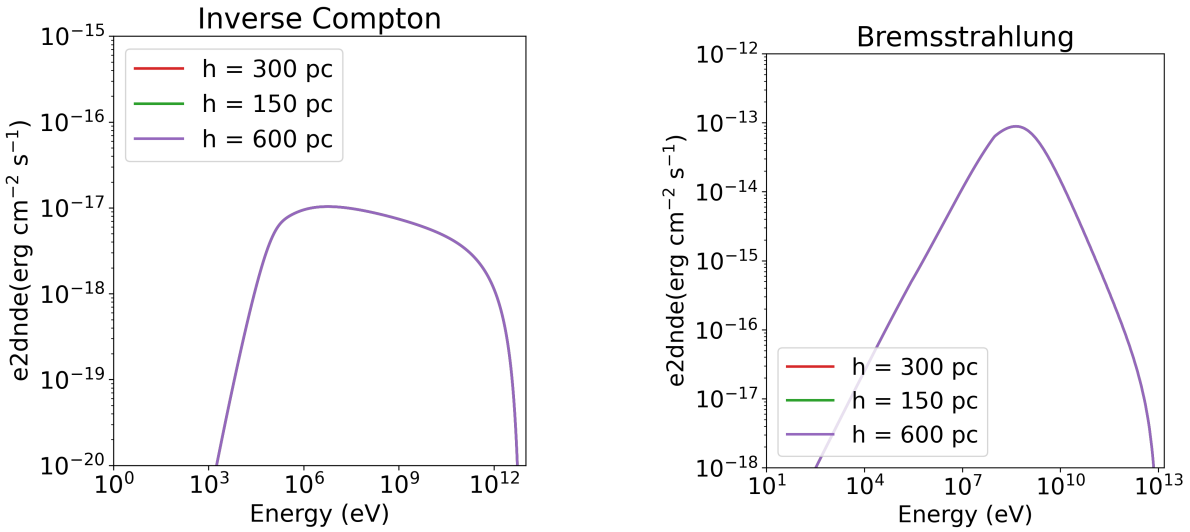

(c) (d)

Figure 47: SEDs for different emission processes as a function of energy, shown for three different heights of the emission region: $h = 150\,pc$, $h = 300\,pc$, and $h = 600\,pc$. The panels display (a) normal and absorbed pion decay, (b) synchrotron emission, (c) inverse Compton scattering, and (d) bremsstrahlung. Each curve illustrates how the corresponding process varies with changes in the size of the absorption region.

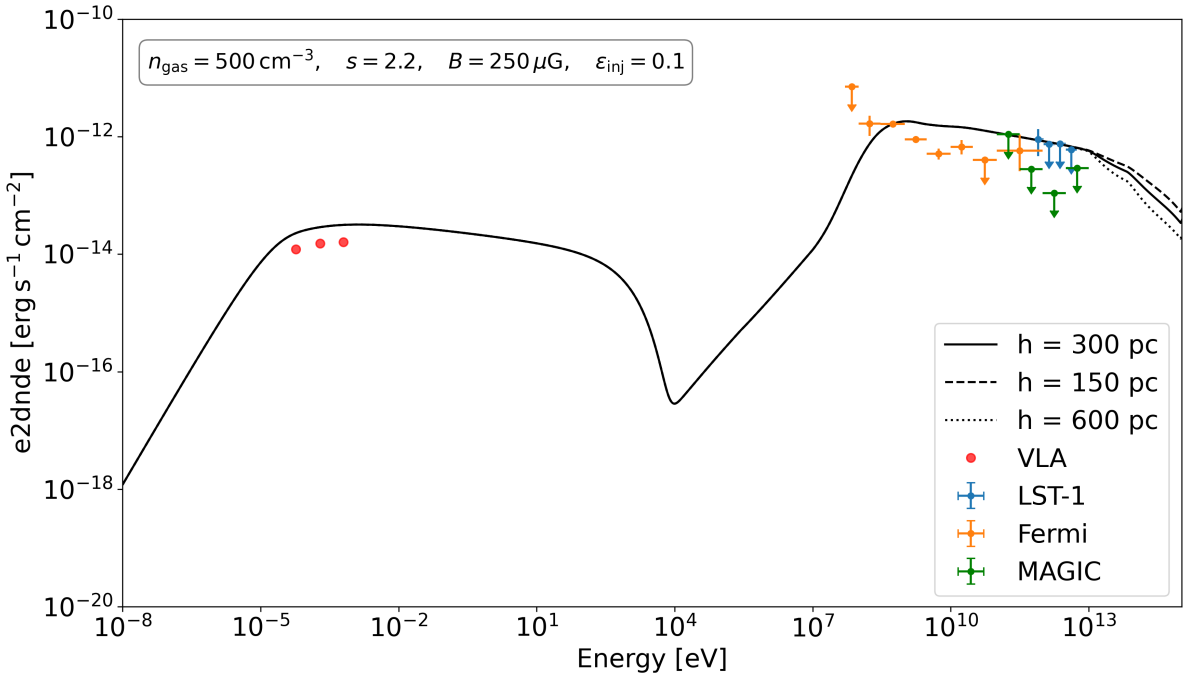

Figure 48: Total SED for NGC 1068 obtained varying the value of the height of the absorption region h between 150 pc and 600 pc, and keeping particle density $n_{\rm gas}$, spectral index s, injection efficiency ϵ_{inj} and magnetic field B fixed.

After performing the exploration of parameters, we chose the set of parameters summarized in Table 4 that generates a model that better represents the data.
Below, we show the cooling plots (Figure 49), the particle distributions (Figure 50) and the final model (Figure 51) obtained with the chosen set of parameters that better reproduce these data.

Table 4: Best set of parameters for NGC 1068.

Parameter	**Value**
Spectral index, s	2.4
Gas density, $n_{\rm gas}$	500 cm^{-3}
Magnetic field, B	200 μG
Injection efficiency, $\epsilon_{\rm inj}$	0.05
height of the absorption region , h	300 pc

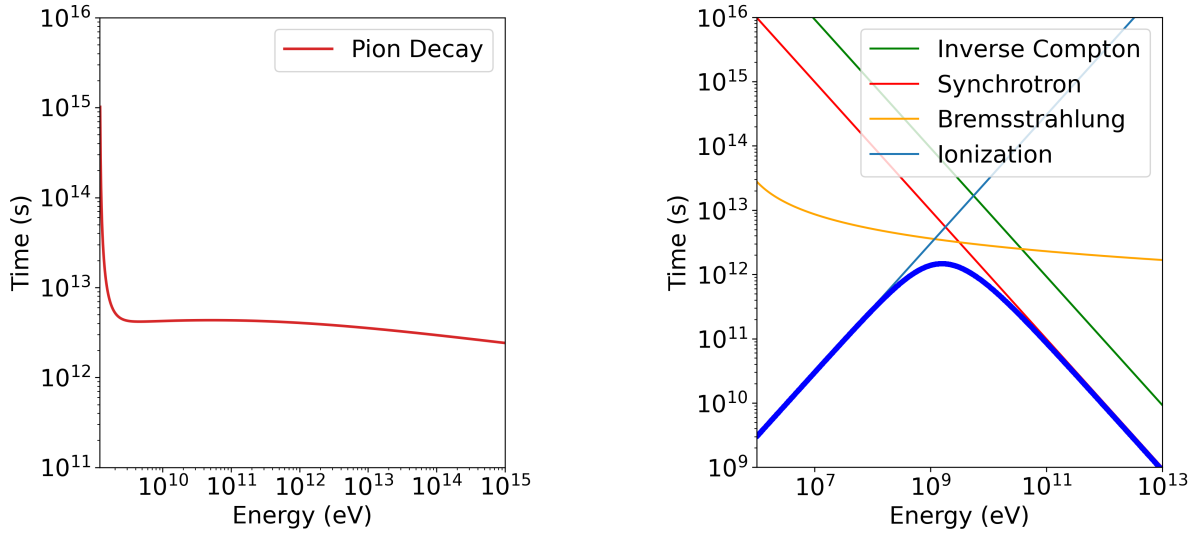

(a) (b)

Figure 49: Cooling times as function of energy for (a) protons and (b) electrons calculated using the best set of parameters.

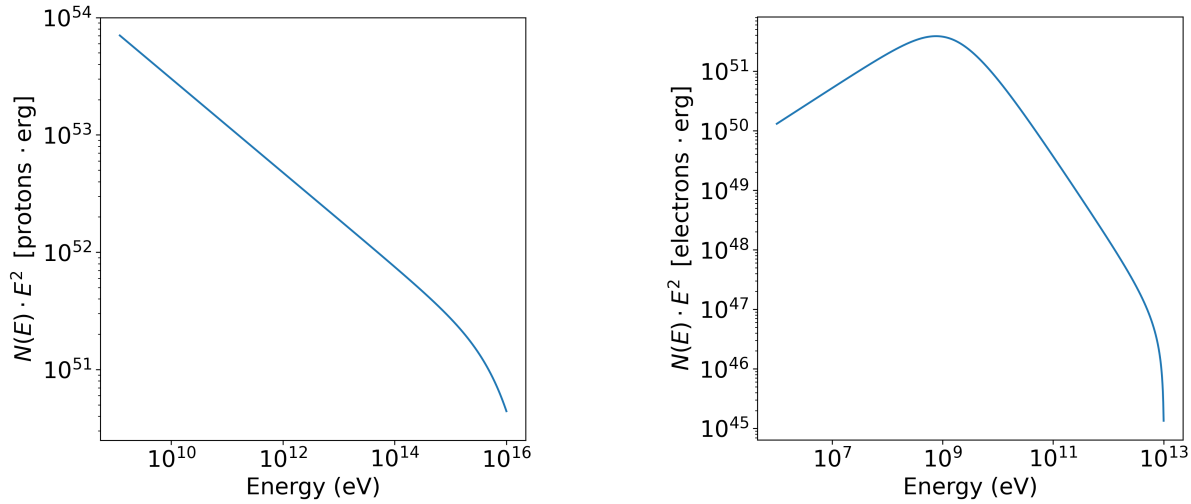

(a) (b)

Figure 50: Particles distributions obtained after solving the transport equation for protons (a) and electrons (b), using the best set of parameters.

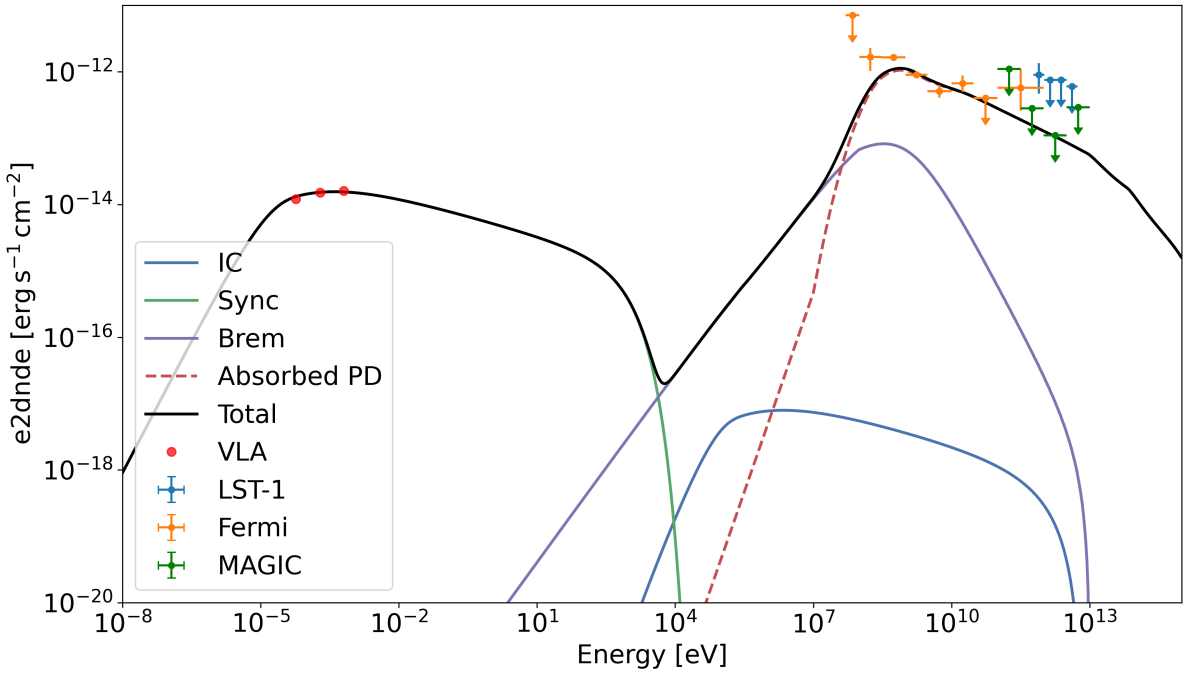

Figure 51: Complete model of NGC 1068 obtained from the best set of parameters.

In the final model in Figure 51 there is a good agreement with VLA data in the low-energy range. At higher energies, starting from 10^7 eV, the total curve reproduces the Fermi-LAT data reasonably well; similarly for LST-1 and MAGIC, the model respects the constraints imposed by the upper limits.

5.3 Sensitivity curves

Finally, we compare the results obtained above with the the analysis and from the model, with the efficiencies of both ground-based (CTAO) and space-based (COSI) future facilities.

For what concerns CTAO, it will deliver unprecedented performance in very-high-energy gamma-ray astronomy, providing both a very wide energy range and excellent angular resolution and sensitivity compared to any existing detector. With coverage from ~ 20 GeV up to 300 TeV, CTAO will be capable of probing the most distant gamma-ray sources while simultaneously exploring the extreme end of the electromagnetic spectrum, opening a new observational window on the Universe. The sensitivity curves quantify the minimum gamma-ray flux detectable by CTAO as a function of energy and are derived from detailed Monte Carlo simulations. A power-law input spectrum with photon index 2.62 was assumed, though the resulting instrument response functions (IRFs) do not depend on the assumed source spectral shape. Background cosmic-ray spectra of protons and electrons/positrons were modeled using recent cosmic-ray measurements (Observatory and Consortium, 2021).

The differential sensitivity is defined as the minimum flux required to achieve a 5σ detection for a point-like source in non-overlapping logarithmic energy bins (five per decade). In addition, each energy bin must contain at least ten detected gamma rays and satisfy a minimum signal-to-background ratio of 1/20. This criterion ensures that the detected signal is at least 5% of the background, which means maximizing meaningful detections and minimizing systematic uncertainties.

The analysis cuts are optimized per bin to maximize flux sensitivity, and since optimal cuts depend on the exposure time, IRFs are provided for three observation times: 0.5, 5, and 50 hours. Performance estimates are available for three zenith angles (20°, 40°, and 60°), with azimuthal variations included to account for geomagnetic effects.
The current publicly available IRFs correspond to version `prod5 v0.1`, telescope model `prod5-model`, and were released in September 2021 (Observatory and Consortium, 2021).
What we did was computing the sensitivity curves of both CTAO North and CTAO South through `Gammapy`, using the IRFs for 20° zenith angle for 50 hours, for an averaged azimuthal angle.
For what concerns the future space-based mission, in this work we focus on the MeV Gap. The energy band between 0.02 MeV and 100 MeV has not been really explored until now, so there is a lack of observations in this range. The MeV energy band is particularly significant because it allows the most direct study of the fundamental physical properties of high-energy astrophysical objects. This range also exhibits spectral signatures characteristic of gamma-ray emission resulting from pion decay, providing strong evidence for hadronic acceleration processes. Consequently, the MeV domain is essential for investigating radiating, non-thermal particles and for distinguishing between leptonic and hadronic mechanisms. Furthermore, this energy region encompasses key nuclear gamma-ray lines produced through radioactive decay, nuclear collisions, positron annihilation, and neutron capture. Thus, it holds a role in high-energy astrophysics comparable to that of optical spectroscopy in the study of atomic phenomena (De Angelis et al., 2021).
The MeV domain has historically lagged behind the other energy ranges (X-rays and high- or very-high-energy gamma rays) in terms of detection sensitivity. This limitation arises from instrumental challenges unique to this energy region. In particular, below a few MeV, the absence of a distinct electron–positron pair-creation signature hinders the ability to effectively discriminate gamma rays from charged particles and to determine the incident direction of photons. Additionally, although this range includes numerous nuclear gamma-ray lines that are of great astrophysical interest, it also introduces substantial instrumental background caused by the activation and subsequent deactivation of irradiated materials in space. Recent advances in silicon detector technology and readout microelectronics now make it possible to design new space instruments with a sensitivity improvement of nearly two orders of magnitude compared to COMPTEL.
This is why we took one of the next and most promising space missions (COSI) and compared its sensitivity from Tomsick et al. (2023) with our model and our data. In Figure 52 we present the general picture. The plot includes more than 10 hours of VLA data, 14 years of Fermi-LAT data, 125 hours of MAGIC data, 20 hours of LST-1 data, the model, and the sensitivity curves for COSI (2 years) and CTAO North and CTAO South (50 hours).
From the plot, it is evident that the full CTAO arrays, in particular CTAO South, will significantly improve the performances of current ground-based gamma-ray instruments in this energy range. In several energy intervals, CTAO South reaches sensitivities comparable to, or even better than, those achieved by MAGIC, but with substantially shorter observation times. This shows how the larger number of telescopes and the optimized array layout lead to higher photon statistics, improved background rejection, and consequently lower minimum detectable fluxes.
The LST-1 results shown here represent only the performance of a single Large-Sized Telescope. Once the full CTAO North array becomes operational, the LSTs will benefit from stereoscopic observations together with the MSTs. This will result in a improve-

ment in sensitivity as well as an extended effective energy coverage. Accordingly, the flux points currently obtained with LST-1 will be reachable with reduced exposure times and with smaller statistical uncertainties.
Regarding COSI, its expected sensitivity in the MeV band does not reach the flux level predicted by our model for this source. Under the present assumptions, COSI would therefore not be able to detect the modeled emission. However, as discussed in Section 6, plausible modifications to the model, could increase the predicted flux in the COSI energy range. In such scenarios, COSI might provide valuable constraints in the MeV energy range.

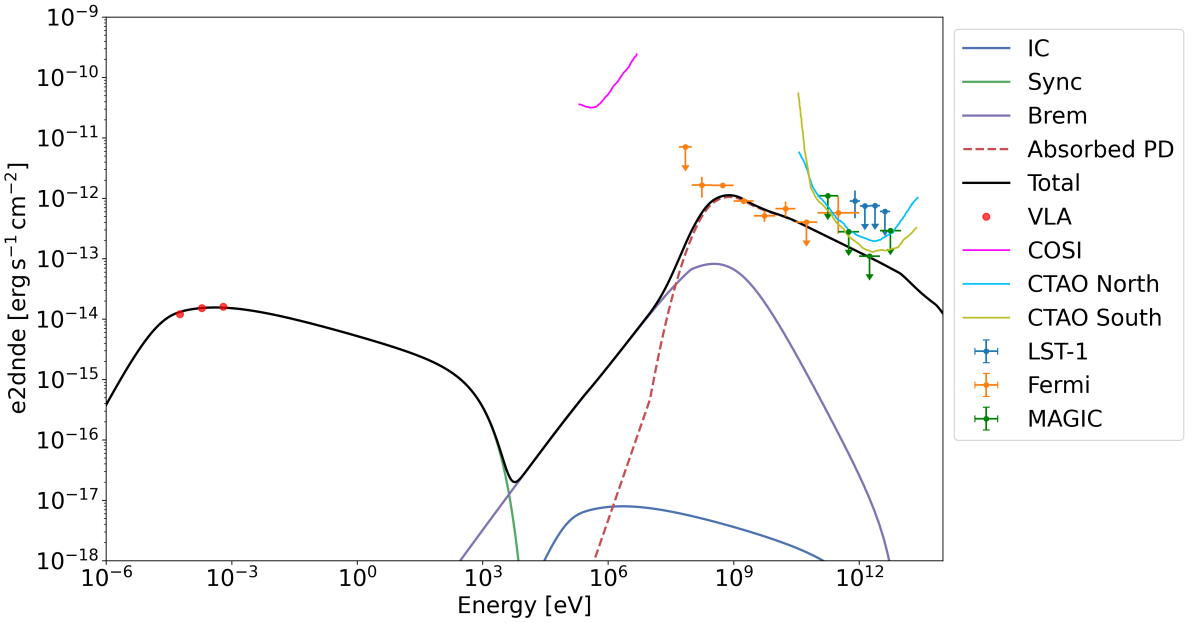

Figure 52: Final model compared with data and sensitivity curves of CTAO North, CTAO South and COSI.

6 Discussion and conclusion

The Seyfert galaxy NGC 1068 has been identified as one of the most significant neutrino-emitter sources, selected among more than 100 sources using about 13 years of IceCube data.
These neutrinos are believed to arise from interactions between high-energy protons and the surrounding matter or radiation fields which are present within the galaxy. Such interactions produce both charged and neutral pions, whose subsequent decays yield neutrinos and gamma rays. While gamma-ray emission may also result from purely leptonic processes, neutrinos can only emerge from hadronic interactions. Consequently, their detection is expected to coincide with accompanying gamma-ray production (Halzen and Hooper, 2002), which is the focus of this work.
A comprehensive study of the non-thermal emission, alongside the source properties such as the emission region, magnetic field, and matter density, is essential not only to understand the origin of its detected gamma-ray emission, but also to develop self-consistent models capable of reproducing the observed neutrino excess from this galaxy.
Gamma rays represent the highest-frequency form of electromagnetic radiation within the electromagnetic spectrum. They are generated through interactions between relativistic particles, known as cosmic ray, and the interstellar medium. This emission arises in some of the most extreme astrophysical environments, such as active galactic nuclei and supernova remnants.
The study of gamma rays provides valuable insights into non-thermal and high-energy processes in the universe, reaching energies far beyond those attainable by terrestrial particle accelerators. Being electrically neutral, gamma rays do not undergo electromagnetic deflection, allowing researchers to trace them back to their sources.
My work has been structured in two parts: the first part focuses on the Data Analysis LST-1 data, starting from some raw data (DL1) that have been transformed into some user-delivered data (DL3), suitable to produce the final science products, specifically SEDs and lightcurves; the second part describes the building of a model for the non-thermal radiation of the starburst region of the galaxy, taking into account the effects of both primary hadrons and leptons, including the contribution of synchrotron emission, inverse Compton, bremsstrahlung, pion decay, and the absorbed pion decay. The final SED is obtained starting from a set of parameters consistent with values reported in the literature. The parameter space, including the spectral index of the injection function, magnetic field, gas density, injection efficiency, and the height of the absorption region, was explored with the goal of assessing the sensitivity of the model to variations in each of these parameters. The best set of parameters was then selected using observational constraints, and the resulting spectrum was compared with previously analyzed data from LST-1 as well as with data from other experiments, including VLA, Fermi-LAT, and MAGIC.
Finally, the model was compared with the sensitivity curves of some future facilities to place some constraints on what we would be able to observe. The future facilities taken into account are CTAO North and South for the ground-based facilities, and COSI for the space-based facilities. COSI has been chosen in the perspective of investigating the MeV band. This energy band has been rarely explored during the years due to several instrumental challenges, resulting in a gap in the multiwavelength spectra (the MeV Gap).

Below we present the main results obtained from this work:

- For what concerns the LST-1 analysis, after applying all the necessary cuts, 74 runs for a total of 20.02 hours have been retained, corresponding to the 54.8% of the original raw data, in the period between 09/01/2023 and 11/01/2024. The excluded data are characterized by excessive noise of the night sky and/or have too high zenith angles, which would be problematic because high Night Sky Background conditions lead to poorly cleaned images and higher reconstruction uncertainties, while large zenith angles increase atmospheric absorption, which degrades energy and direction reconstruction in LST-1.

- The standard analysis approach revealed certain issues: the excess of source signal with respect to the background showed a decreasing and fluctuating behavior, resulting in a steadily negative value that becomes more pronounced with increasing observation livetime. This behavior contrasts with what is expected for a real astrophysical source, which should instead show positive values that increase with exposure time, or at least remain roughly constant around zero; the cumulative Counts Map showed a void, associated with some stars in the field of view or some atmospheric related problem. Both issues are related to the background calibration.

- Detailed investigation of this source, particularly the θ^2 plots (i.e., the difference between the on-source and off-source regions with the same angular cut), reveals that the background problem is particularly relevant in the $0.01 - 0.1$ TeV energy range; we carried out additional tests like verifying the Counts Map for each run and obtaining the number of counts versus the background for different pointing positions, confirming the background-related problems.

- A solution was found after bringing the problem to the LST Collaboration through the LST Analysis Meeting of June 16th 2025, where various solutions have been discussed, among which setting a higher value of the minimum reconstructed energy, whose value has been set to 0.6 TeV, leading to obtaining 1 flux point with a significance of 2.1 σ and 3 upper limits, between $6 \cdot 10^{-1}$ and 5.5 TeV.

- For what concerns the model, based on Eichmann et al. (2022) and Kornecki et al. (2020, 2022), the best set of free parameters which is able to reproduce the observations is the following: spectral index s = 2.4, gas density $n_{gas} = 500\text{cm}^{-3}$, magnetic field B = 200$\mu$G, injection efficiency $\epsilon_{inj} = 0.05$, height of the absorption region h = 300pc.
  The spectral index of the injected function s, even if it is compatible with the gamma-ray bounds (Acciari et al., 2019; Bechtol et al., 2017; Eichmann et al., 2022), is somehow a limit situation, as the usual range is between s = 2.1 and s = 2.3 (Acciari et al., 2019), that might be affected by the limitation coming from the model itself, like not including the emission coming from the corona, or the fact that we are considering a system with no particle escape. Including both particle escape and the AGN corona transforms the non-thermal model of NGC 1068 from a purely calorimetric starburst scenario into a multi-zone system in which high-energy particles may leave the starburst region before interacting, reducing the hadronic gamma-ray yield, steepening the spectra, and potentially

requiring harder or more efficient cosmic-ray injection, hence changing the value of s. Conversely, the corona introduces efficient $p\gamma$ interactions, which dominate in the coronal region, and $\gamma\gamma$ absorption that can supply additional high-energy emission and neutrinos, reshaping the observed spectrum.
The other derived parameters are consistent and fall within the ranges of values found in other works, like Eichmann and Tjus (2016).

- The parameter-space exploration carried out in this work demonstrates that the non-thermal emission of the starburst region of NGC 1068 can be reproduced through a physically consistent combination of model parameters. The variation of each parameter confirms the physical dependencies from the parameters to the final SED discussed in Chapter 4.1. In particular, the magnetic field strength regulates the synchrotron cooling timescale ($t_{\rm syn} \propto B^{-2}$) and therefore affects only the low-energy portion of the SED, leaving the hadronic component unchanged, as expected for magnetic-field-independent *pp* interactions. The gas density $n_{\rm gas}$ modifies the relative importance of bremsstrahlung and inverse Compton emission, while preserving the shape of the pion-decay spectrum, consistent with the extremely short lifetime of pions, which prevents their interaction with the ambient medium. The spectral index s of the injection function constitutes the most sensitive parameter: any modification of s directly alters both proton and electron particle distributions, producing spectral variations across the entire energy domain. The injection efficiency $\epsilon_{\rm inj}$ acts solely as a normalization factor, and the height of the absorption region h influences only the high-energy attenuation through $\gamma\gamma$ absorption.
  The resulting cooling timescales for both hadronic and leptonic populations are in excellent agreement with those computed by Kornecki et al. (2020) and Eichmann et al. (2022). Protons lose energy predominantly through *pp* interactions on timescales of $\sim 1.7 \cdot 10^{13}$ s between $\sim 10^9$ and $\sim 10^{15}$ eV, confirming the starburst region of NGC 1068 to be an efficient hadronic calorimeter. Electrons present a faster cooling regime then protons. At low energies, ionization losses dominate the cooling, while at higher energies the radiative losses are governed by synchrotron emission. Moreover, the bremsstrahlung emission dominates for a very tiny portion of the energy spectrum, at around $\sim 10^9$ eV. This transition in the dominant cooling channel shapes the electron distribution and, consequently, the SED. The hierarchy among these cooling channels is dependent from the physical assumptions, hence the parameters, adopted in this work.
  The resulting multi-wavelength emission is consistent with previous works where modeling was presented. In particular, the high-energy component of our SED agrees with the starburst interpretation presented by Ajello et al. (2023). The total SED matches the results of Eichmann et al. (2022), proving the robustness of the model.
  In general, the consistency between our results and independent studies indicates that the starburst region alone is capable of reproducing the observed non-thermal emission of NGC 1068. This provides a solid basis for future extensions of the model.

- The $\gamma\gamma$ absorption in the high-energy part of the spectrum due to the IR field was manually computed since `naima` package does not support it. The model shows that it becomes relevant above $\sim 10^{13}$ eV, in agreement with Acciari et al. (2019).

Nevertheless, the inclusion of an UV/optical component associated with unprocessed stellar radiation could affect the emission at lower energies.
Including an additional UV/optical radiation component, associated with unprocessed stellar emission, would modify the predicted $\gamma\gamma$ absorption at lower energies. This effect arises because the pair-production threshold depends inversely on the energy of the target photons (Romero, 2021),

$$E_{\gamma}^{\mathrm{thr}} \simeq \frac{(m_e c^2)^2}{\epsilon_{\mathrm{target}}}, \tag{58}$$

so that introducing a population of higher-energy UV/optical photons (with energies around 10 eV) lowers the threshold for absorption by several orders of magnitude compared to the case in which only FIR photons ($\epsilon_{\mathrm{target}} \sim 0.1 - 1$ eV) are present.

- The neutrino spectrum usually has the same order of magnitude of the gamma emission, but in our prediction, the gamma ray emission is several orders of magnitude above and this model is not in accordance with it. Despite this, modeling the emission of the star forming region is extremely important to place some constraints on the value of the parameters of this region and a complete and accurate model.

- The results obtained after the comparison of COSI sensitivity curve are not really conclusive since the detection limit of the instrument ($\sim 10^{-11}\mathrm{erg\,s^{-1}cm^{-2}}$), is much higher then the emission in the same energy range given from the model ($\sim 10^{-15}\mathrm{erg\,s^{-1}cm^{-2}}$).
Even though this seems correct at first glance, this conclusion might be reconsidered since Peretti et al. (2019) and Kornecki et al. (2021) demonstrate that secondary electrons produced by pair creation from $\gamma\gamma$ absorption can produce synchrotron emission that boosts the MeV flux, implying that the starburst region could still contribute to the observable MeV emission.

- The results from the LST-1 analysis served as a reference for cross-checking another study conducted by PhD student Sweta Menon. All related details are documented on the Collaboration's internal wiki page, which is not publicly accessible.

- The whole work has been presented in form of outreach article on the journal Coelum Astronomia, n. 276, in an article called 'La galassia NGC 1068 - un esempio di studio complesso' (Figure 53).

Moreover, this work establishes the foundation for future research on topics such as:

1. The present work clearly revealed some issues with the LST-1 data of NGC 1068, especially at lower energies, which have been brought to the attention of the collaboration. This has opened the path to future investigation in this particular dataset, for example to better understand the background issues through some advanced background reconstruction models (de Bony de Lavergne et al., 2025). Another possible improvement would be to perform a more advanced analysis by modifying parameters that are usually kept at their default values, such as investigating how the results are affected by changing the gammaness threshold (i.e., the probability

of the primary particle being a gamma-ray).
The LST pipeline is quite new and continuously in development, changing rapidly, and so the analysis procedures, which means that we will keep having better results with time.

2. The results obtained from the analysis will be drastically improved increasing the observation hours. If we compare them ($\sim$ 20 hours of observations) with Fermi-LAT data (14 years of observations) and MAGIC (125 hours of observations), we can immediately notice the power of LST-1. The sensitivity increases further when we take into account CTAO. In Figure 52, we can see the comparison between the data and the sensitivity curves of CTAO North and South, obtained for 50 hours of observations. The full array in the Alpha Configuration (see Section 2.5.1) appears to be extremely promising as it is capable to reach the same results of MAGIC in less than half of the time.
Due to its favorable position in the sky $(\mathrm{RA}, \mathrm{Dec}) = (40.670°, -0.013°)$, NGC 1068 can be potentially observed by both the arrays, which would lead to more precise measurements, especially with CTAO South due to its higher sensitivity.

3. The finally derived model was a simplified version of the whole picture. It can be further improved including:

   - the emission from the corona (Eichmann et al., 2022), which could be fundamental to explain the discrepancy in the spectrum between neutrinos and gamma-rays. The high temperature of the gas in this site leads us to think about different acceleration mechanisms (Padovani et al., 2024), like stochastic acceleration in turbulence (Murase et al., 2020) and diffusive shock acceleration (Inoue et al., 2020). Both these mechanisms could be able to efficiently produce the neutrino spectrum observed by IceCube, while the gamma-ray counterpart is believed to be absorbed in the MeV band due to decays and interactions with other particles. A study on the corona of NGC 1068 (Inoue et al., 2021) shows much shorter cooling times (by a factor ~ 7 for both protons and electrons), affecting drastically the final SED, which results in a higher contribution especially in the MeV band;
   - the contribution of secondary electrons produced by pair production or through photohadronic collisions and tertiary electrons produced by pair production of high-energy gamma rays. Their inclusion may contribute to the hard X-ray band through synchrotron emission, which, in turn, can also place stronger constraints on the magnetic field strength (Peretti et al., 2019);

4. The study presented by Inoue et al. (2021) predicts a contribution to the gamma-ray emission originating from the coronal region, with an estimated flux of approximately $\sim 1.5 \times 10^{-10}$ erg s^{-1} cm^{-2} at an energy of around 1 MeV. This energy range falls well within the observational capabilities of the upcoming COSI mission, making this source a particularly promising candidate for future observations (Figure 54).
Such observations could substantially enhance our understanding of the system's emission mechanisms and offer critical insights into the origin and characteristics of its neutrino spectrum, thereby contributing to a more comprehensive picture of its multi-messenger behavior.

Figure 53: Outreach article about NGC 1068 published on the journal Coelum Astronomia.

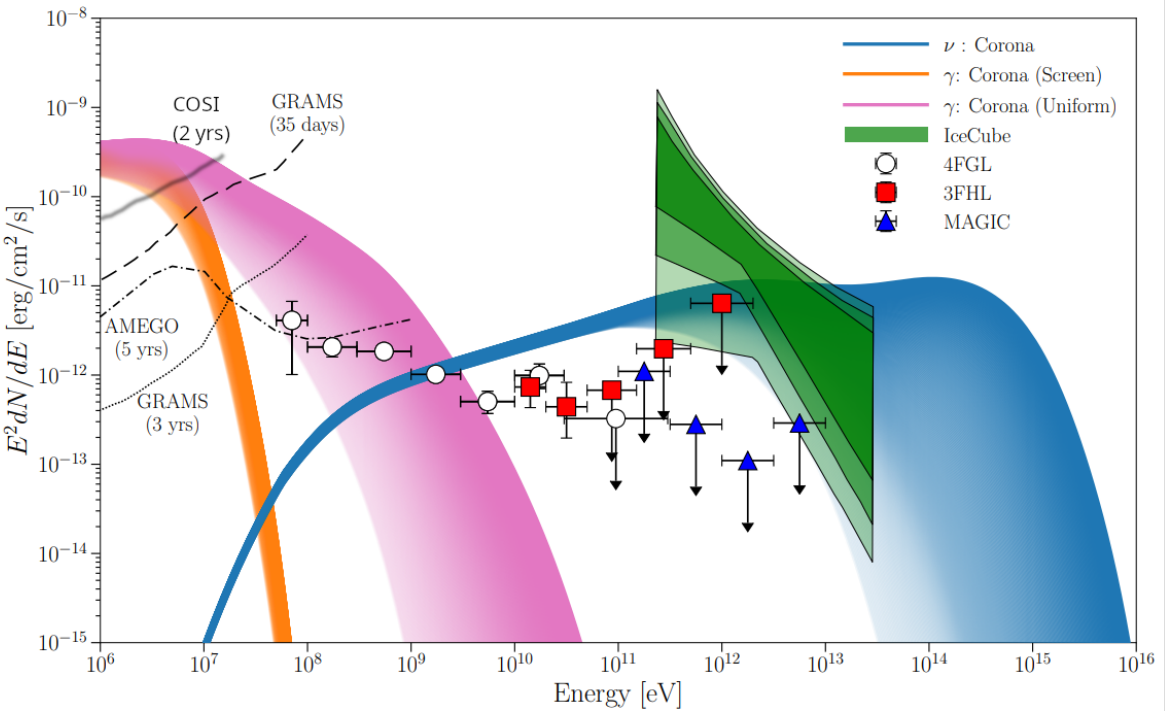

Figure 54: Gamma-ray and neutrino spectrum of NGC 1068, where the white, red markers correspond to data from the Fermi-LAT Collaboration, while the blue markers correspond to MAGIC data. The green shaded areas indicate the 1σ, 2σ, and 3σ confidence regions of the spectrum measured by IceCube. The blue shaded region shows the expected neutrino spectrum, while the orange and magenta regions depict the gamma-ray spectra for the uniform and screened cases, respectively. In the uniform emissivity case, gamma-rays and target photons are uniformly distributed. Gamma-rays are attenuated by a factor of $\frac{3(0.5+exp(-\tau)/\tau-[1-exp(-\tau)]/\tau^2)}{\tau^2}$. In the screened case, gamma-rays are assumed to be generated in the inner part of the corona, and the attenuating photon field surrounds it. In this case, the attenuation corresponds to a factor of $exp(-\tau)$. In both cases τ is the gamma-ray optical depth computed from the center of the corona. For comparison, the sensitivity curves of GRAMS (Aramaki et al., 2020), AMEGO (Kierans, 2020), as well as the one of COSI, are included. The GRAMS (Gamma-Ray and AntiMatter Survey) Project is a NASA mission which aims to reach extraordinary sensitivities to astrophysical observations with MeV gamma-rays and indirect dark matter searches with antimatter. The prototype flight is due in 2026 (`https://grams.sites.northeastern.edu/`). AMEGO is a next-generation mission concept by NASA that will advance MeV astrophysics by enabling sensitive continuum spectral studies, precise polarization measurements, and high-resolution nuclear line spectroscopy (`https://asd.gsfc.nasa.gov/amego/`). Figure adapted from Inoue et al. (2020).

Appendix

A Standard analysis and problems diagnostic

Standard analysis and background issues

The basic idea is that current IACT data is organized in runs or observations identified by an `OBS_ID`. For each observation, there is one `EVENTS` and several IRF FITS HDUs containing all the necessary information for the analysis. To manage these, two index tables are provided: the observation index table, which stores metadata about each run (e.g. pointing direction, duration, number of events), and the HDU index table, which lists all available HDUs and the files where they are located. These indices allow science tools to locate and load the relevant data. In particular, when opening a DL3 file for a given entry in the observation index, we obtain an `EventList`, which represents the detected events of that observation. The `EventList` carries detailed information such as event time, position, energy, and *gammaness*, the probability that a detected photon is truly a gamma ray.

The analysis was carried out following the standard procedure. To ensure data quality, only observations with a maximum zenith angle of 50° and a minimum live time of 60 seconds were selected. After applying these cuts, the dataset amounts to a total live time of 19.0 hours, with a total elapsed time of 20.0 hours, accounting for telescope pointing periods.

The reconstructed energy range was set from a minimum value of 0.05 TeV (*e_reco_min*, which is going to be a key variable parameter) to a maximum value of 50 TeV, while the true energy range was defined between 0.01–100 TeV. Energy binning was performed logarithmically, using 4 bins per decade for reconstructed energy and 10 bins per decade for true energy.

For background estimation, the wobble method was adopted, employing two OFF regions. In addition, a safe energy threshold was applied through the safe mask, setting the lower bound at 5% of the maximum effective area, in order to restrict the analysis to a reliable energy range. All the settings are summarized in Table 5.

After the initial analysis settings, we generated some diagnostic plot, counts maps, excess counts. In particular, the excess counts are defined as the difference between the ON counts and the OFF counts, livetime maps, shown below.

Table 5: Summary of Standard Analysis Settings

Parameter	**Value**
Maximum zenith angle	50°
Minimum live time per observation	60 s
Reconstructed energy range	0.05–50 TeV
True energy range	0.01–100 TeV
Reconstructed energy bins	4 bins per decade
True energy bins	10 bins per decade
Number of OFF regions	2
Safe energy threshold	5% of maximum effective area

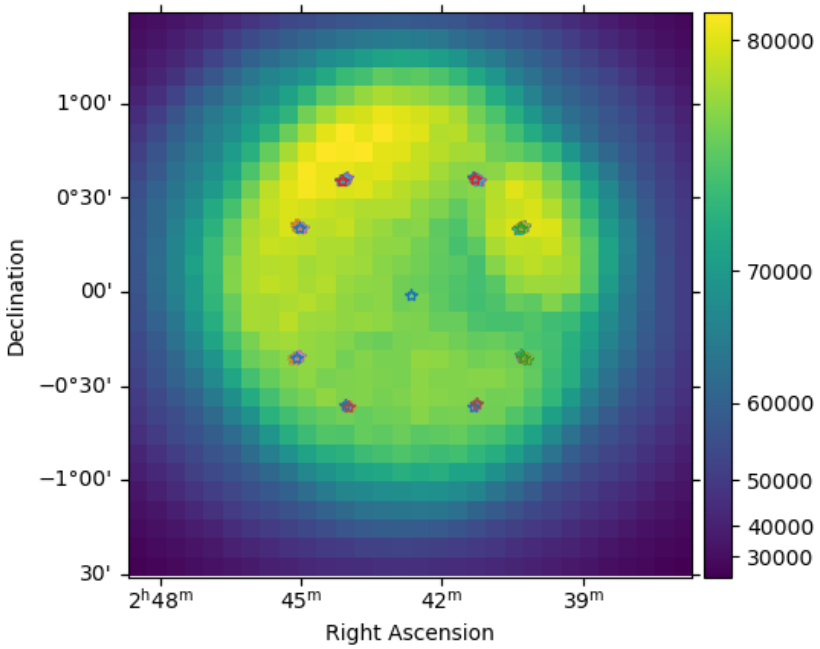

Figure 55: Cumulative map of counts for *e_reco_min* = 0.05 for showing the counts distribution in the sky. The central star represents the position of the source, while the others represent the off-regions.

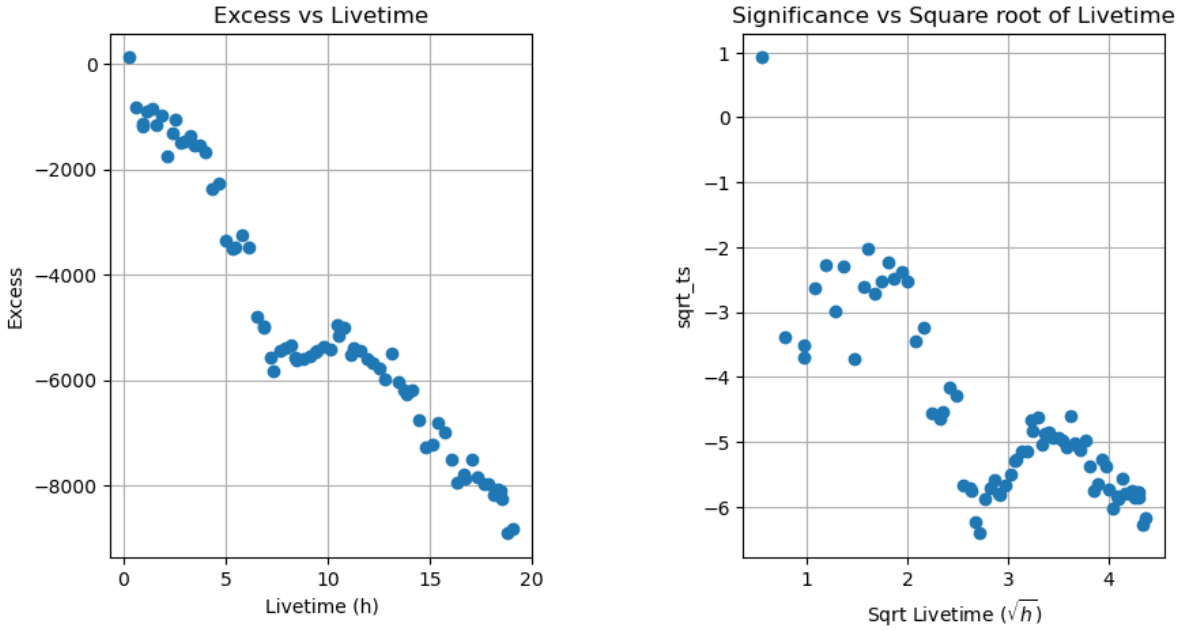

Figure 56: Temporal evolution of excess events and significance value for *e_reco_min* = 0.05.

Next, a spectral model based on Fermi observations of the same source was defined to estimate the flux points. It adopts a power-law form with an index of 2.35, an amplitude of $1.2 \times 10^{-13}\,\mathrm{cm}^{-2}\,\mathrm{s}^{-1}\,\mathrm{TeV}^{-1}$ at a reference energy of 1 TeV. The spectral index was kept frozen during the analysis.
Then, we obtained a total of 11 flux points, plotted in the Spectral Energy Distribution and the lightcurves:

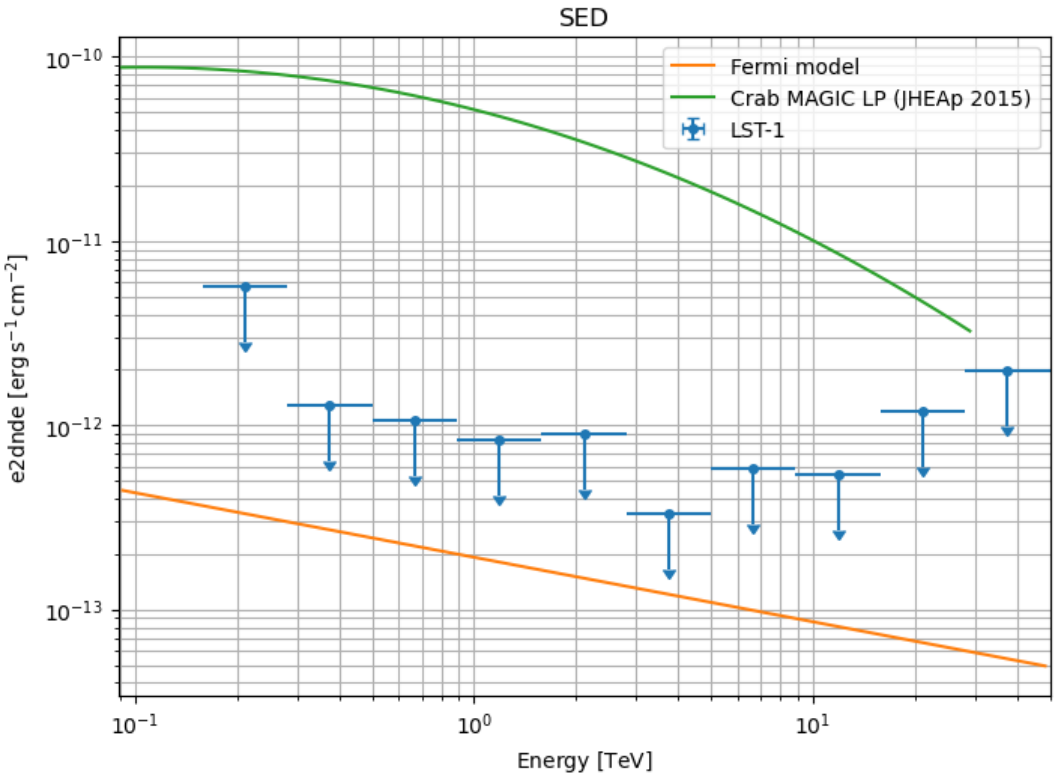

Figure 57: Spectral energy distribution for *e_reco_min* = 0.05 of LST-1 data, compared with the Fermi model and Crab SED.

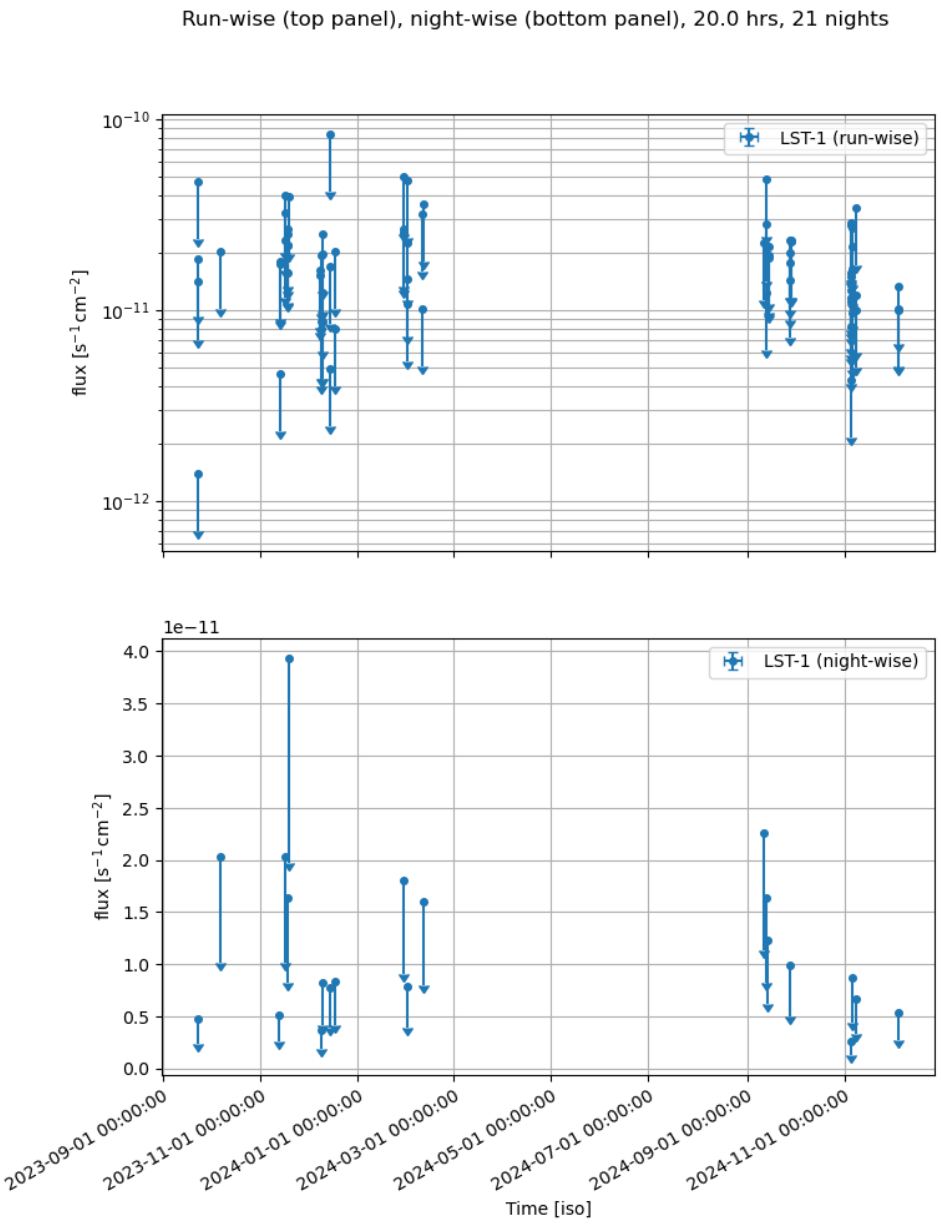

Figure 58: Run-wise (top panel) and night-wise (low-panel) light curves for *e_reco_min* = 0.05.

The same has been done keeping the same settings as before, but selecting *e_reco_min* = 0.1, obtaining the following:

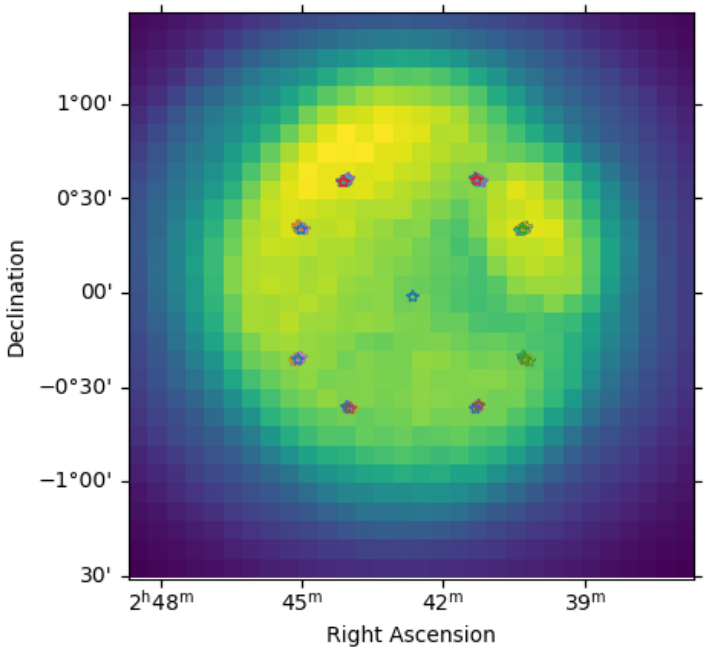

Figure 59: Cumulative map of counts for *e_reco_min* = 0.1 for showing the gamma-ray excess. The central star represents the position of the source, while the others represent the off-regions.

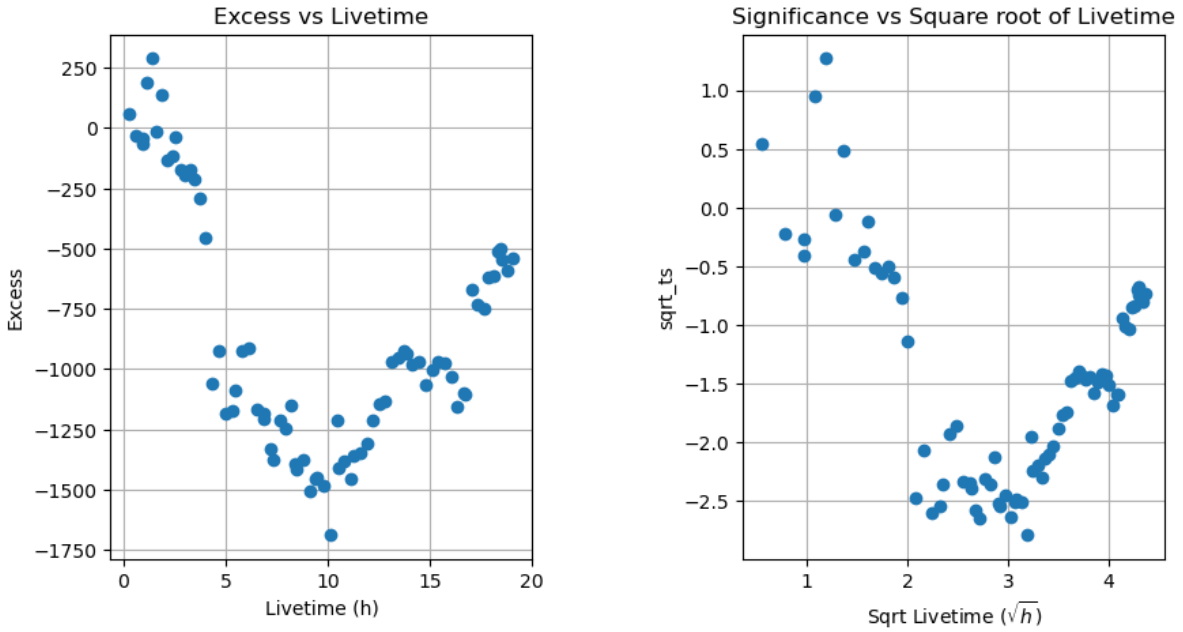

Figure 60: Temporal evolution of excess events and significance value for *e_reco_min* = 0.1.

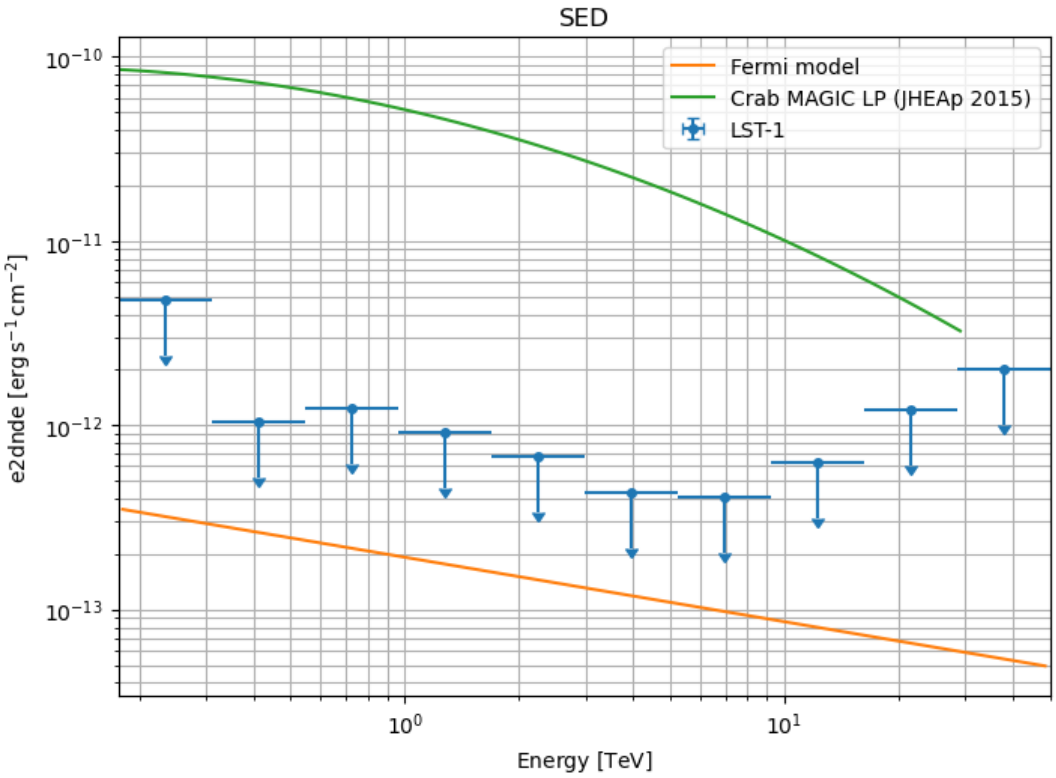

Figure 61: Spectral energy distribution for *e_reco_min* = 0.1 of LST-1 data, compared with the Fermi model and Crab SED.

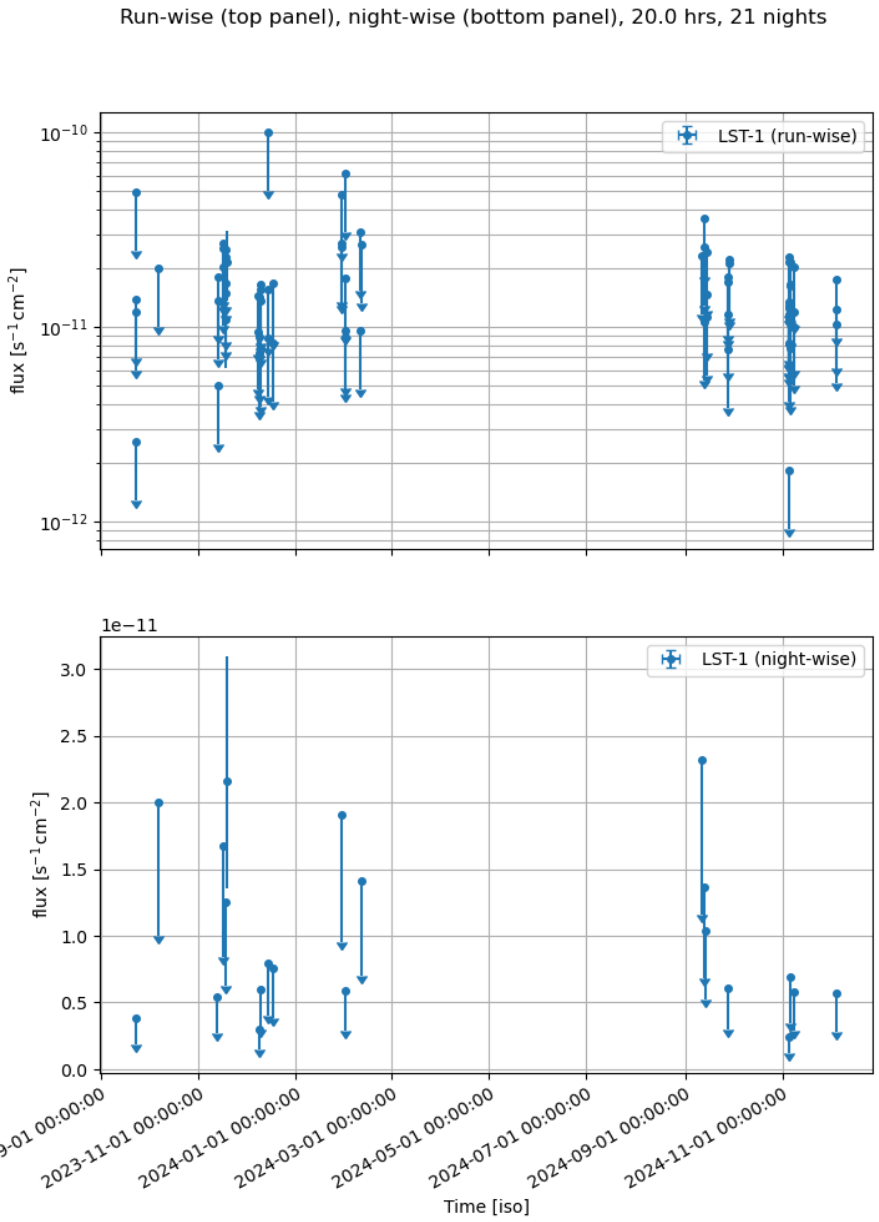

Figure 62: Run-wise (top panel) and night-wise (low panel) light curves for *e_reco_min* = 0.1.

Upon closer examination of the outputs, it became evident that certain inconsistencies emerged. That was visible especially in the excess plots shown in Figures 56 and 60 on the left side. Normally, the cumulative excess shows a growing trend with time or should at most remain constant if no signal is detected from the source, but in this case was definitely the opposite in the case of *e_reco_min*=0.05 and even more complex, even if better from the order of magnitude point of view in the case of *e_reco_min*=0.1.
Another problem, but less noticeable, was present in the counts maps in Figures 55 and 59. At both energies they presented some voids in the upper-right part of the plots, suggesting the presence of a problem related with the background calibration, which is strictly related to the excess plots' behavior.
Hence, a substantial amount of time has been spent investigating this problem.

Problem diagnostic
In order to understand what was the nature of the unusual behavior seen performing the standard analysis, the following checks have been performed:

- High zenith angle test
  To ensure the reliability of the LST data, we examined the zenith angle distribution of the runs shown in Figure 63. Observations at large zenith angles are less favorable, as the longer atmospheric path length can affect both the effective area and the background estimation. By inspecting the histogram of zenith angles, we verified that the runs were reasonably well distributed, with several concentrated at low zenith angles. Therefore, an excess of high-zenith-angle observations can be excluded as a potential source of bias in the analysis.

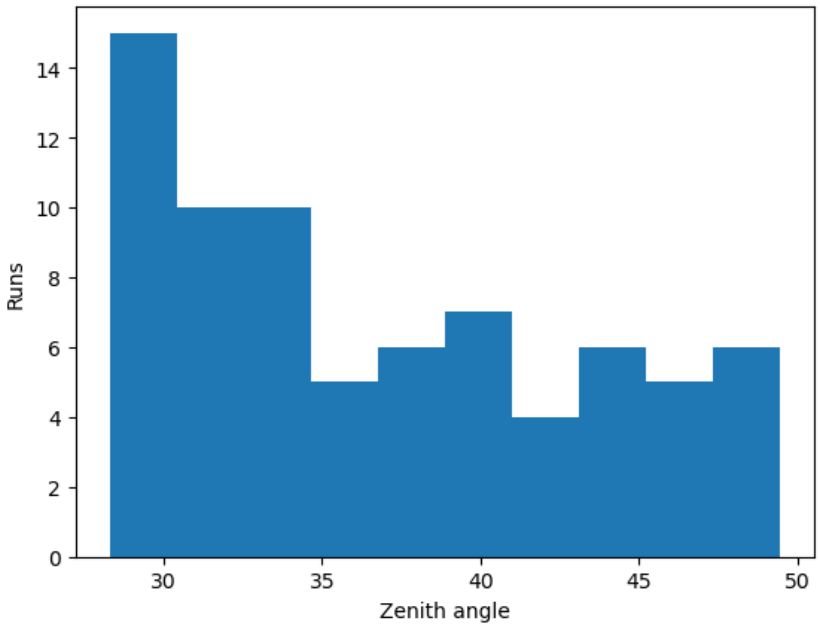

Figure 63: Histogram representing runs versus zenith angles. The runs seems evenly distributed, with a peak at low angles.

- Counts Map

  The map of counts revealed some "inhomogeneities" in the upper-right region of the field of view. Such features are indicative of possible background calibration issue.
  To further investigate these features, the counts map was plotted separately for each individual run. As shown in Figure 64, it is evident that the distribution of counts is not symmetric. Instead, very large differences are observed across the field, reinforcing the suspicion that the anomalies are not statistical fluctuations but rather systematic effects. Two are the main problems that might be the principal cause of it: one, the excess surrounded by a dip in the cumulative Counts Map in Figure 59 in the top right seems to be at fixed sky position, not camera position, indicating the effect of an astronomical object, likely a star; two, there are changing large-scale gradients, likely dependent on observing conditions (effects related to the atmosphere).

- Theta-Squared Analysis:

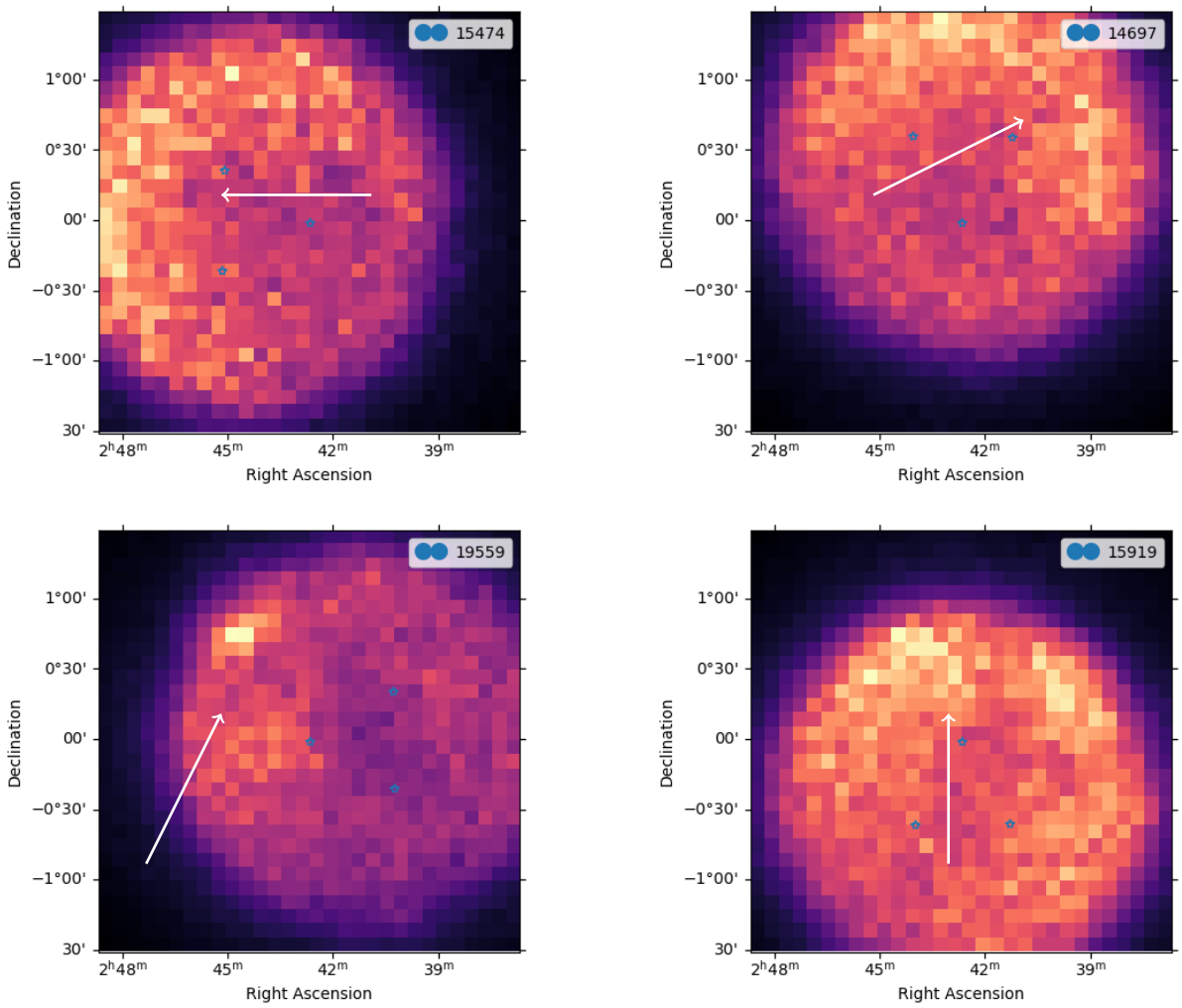

Figure 64: Representative subset of counts maps illustrating clear inhomogeneities in the field. These localized structures, indicated by the arrows, are later reflected in the cumulative counts map, suggesting that the observed effect is systematic rather than statistical.

To determine the number of gamma-ray events originating from the source, we evaluate the background contribution using the OFF regions. The squared angular distance, θ^2, represents the squared angular distance between the reconstructed event direction and the center of the ON or OFF region. Under the assumption of a radially symmetric background, the θ^2 distributions of background events in the ON and OFF regions are expected to be identical within statistical fluctuations. Gamma-ray events from the source, however, peak at small θ^2 values, leading to an excess in the ON region over the OFF region. By comparing the ON and OFF θ^2 distributions, the number of source events can be determined as the excess at low θ^2. The θ^2 distributions reveal a clear issue in the energy range between 0.01 and 1 TeV. In particular, the lowest bin (0.01–0.1 TeV) shows an unphysical behavior, with the number of counts as a function of θ^2 being consistently negative. This indicates the presence of a very strong background contamination dominating the signal.

A similar problem is also observed in the intermediate range (0.1–1 TeV), although in this case the effect appears less pronounced. Nevertheless, the systematic back-

ground contribution in both ranges suggests that the data quality in this region is significantly compromised.
An additional test, inspired by Abe et al. (2023), consisted of comparing the number of ON-counts with the corresponding background (OFF-counts) for different wobble positions. Specifically, we selected three positions, 90°, 180°, and 270°, as shown in Figure 22. For each case, we computed the relative difference between ON and OFF counts.

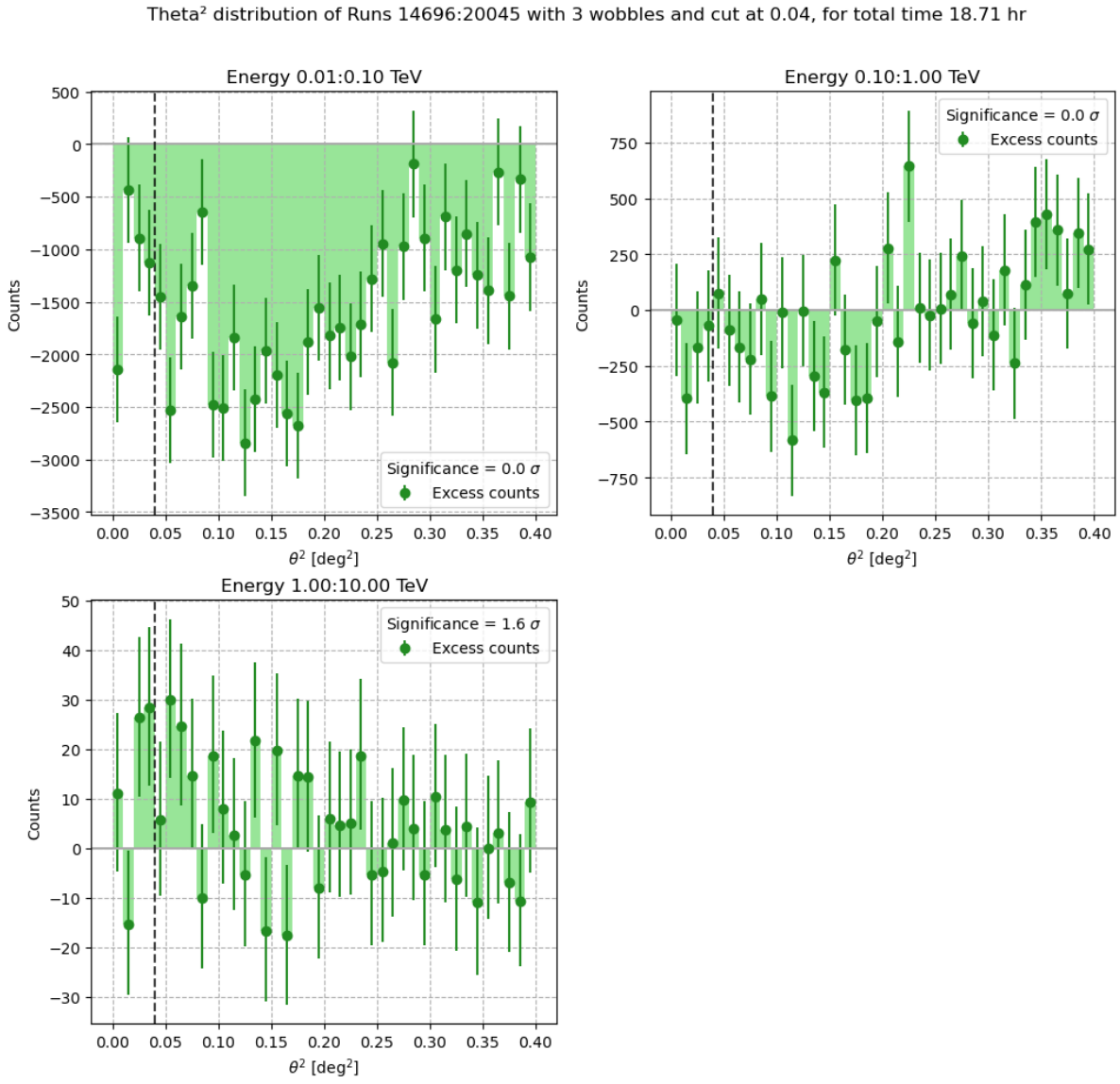

Figure 65: Cumulative Theta Squared plots in three different ranges of energies.

Wobble Position	N_{off}	N_{on}	**Relative Difference**
90°	9,583,123	9,533,137	0.00524 (0.524%)
180°	9,612,901	9,533,137	0.00838 (0.838%)
20°	9,587,910	9,533,137	0.00574 (0.574%)

Table 6: Relative difference between N_{off} and N_{on} for different wobble positions.

The results, summarized in Table 6, show that the ON and OFF counts differ only marginally. Nevertheless, from a closer look to the Table, it is evident that the

number of OFF counts is systematically higher than the ON counts, confirming the presence of a problem related to the background calibration.

Solution

The issue was presented during an LST Analysis Meeting, where we reported the observed anomalies. Following the discussion, the community suggested repeating the analysis with a higher value of *e_reco_min* than previously adopted, in order to mitigate the background contamination in the low-energy range. In this case the *e_reco_min* was set to 0.6 TeV.

References

Abbasi, R., Ackermann, M., Adams, J., Agarwalla, S., Aguilar, J., Ahlers, M., Alameddine, J., Ali, S., Amin, N., Andeen, K., et al. (2025). Evidence for neutrino emission from x-ray bright active galactic nuclei with icecube. *arXiv preprint arXiv:2510.13403*.

Abbott, B. P., Abbott, R., Abbott, T. D., Acernese, F., Ackley, K., Adams, C., Adams, T., Addesso, P., Adhikari, R. X., Adya, V. B., et al. (2017). Gw170817: observation of gravitational waves from a binary neutron star inspiral. *Physical review letters*, 119(16):161101.

Abe, H., Abe, K., Abe, S., Aguasca-Cabot, A., Agudo, I., Crespo, N. A., Antonelli, L., Aramo, C., Arbet-Engels, A., Arcaro, C., et al. (2023). Observations of the crab nebula and pulsar with the large-sized telescope prototype of the cherenkov telescope array. *The Astrophysical Journal*, 956(2):80.

Acciari, V. A., Ansoldi, S., Antonelli, L., Engels, A. A., Baack, D., Babić, A., Banerjee, B., de Almeida, U. B., Barrio, J., González, J. B., et al. (2019). Constraints on gamma-ray and neutrino emission from ngc 1068 with the magic telescopes. *The Astrophysical Journal*, 883(2):135.

Acero, F., Aguasca-Cabot, A., Bernete, J., Biederbeck, N., Djuvsland, J., Donath, A., Feijen, K., Fröse, S., Galelli, C., Khélifi, B., Konrad, J., Kornecki, P., Linhoff, M., McKee, K., Mender, S., Mohrmann, L., Morcuende, D., Olivera-Nieto, L., Peresano, M., Pintore, F., Punch, M., Regeard, M., Remy, Q., Roellinghoff, G., Sinha, A., Sipőcz, B. M., Stapel, H., Streil, K., Terrier, R., Unbehaun, T., Wong, S., and Yu, P. (2025). Gammapy v1.3: Python toolbox for gamma-ray astronomy.

Ackermann, M., Ajello, M., Allafort, A., Baldini, L., Ballet, J., Bastieri, D., Bechtol, K., Bellazzini, R., Berenji, B., Bloom, E., et al. (2012). Gev observations of star-forming galaxies with the fermi large area telescope. *The Astrophysical Journal*, 755(2):164.

Ajello, M., Di Mauro, M., Paliya, V., and Garrappa, S. (2020). The γ-ray emission of star-forming galaxies. *The Astrophysical Journal*, 894(2):88.

Ajello, M., Murase, K., and McDaniel, A. (2023). Disentangling the hadronic components in ngc 1068. *The Astrophysical Journal Letters*, 954(2):L49.

Aleksić, J., Ansoldi, S., Antonelli, L. A., Antoranz, P., Babic, A., Bangale, P., Barceló, M., Barrio, J., González, J. B., Bednarek, W., et al. (2016). The major upgrade of the magic telescopes, part ii: A performance study using observations of the crab nebula. *Astroparticle Physics*, 72:76–94.

Almeida, C. R., Levenson, N. A., Espinosa, J. R., Alonso-Herrero, A., Ramos, A. A., Radomski, J. T., Packham, C., Fisher, R. S., and Telesco, C. M. (2009). The infrared nuclear emission of seyfert galaxies on parsec scales: Testing the clumpy torus models. *The Astrophysical Journal*, 702(2):1127.

Ambrosi, G., Awane, Y., Baba, H., Bamba, A., Barceló, M., de Almeida, U. B., Barrio, J., Bigas, O. B., Boix, J., Brunetti, L., et al. (2013). The cherenkov telescope array large size telescope. *arXiv preprint arXiv:1307.4565*.

Antonucci, R. (1993). Unified models for active galactic nuclei and quasars. *In: Annual review of astronomy and astrophysics. Vol. 31 (A94-12726 02-90), p. 473-521.*, 31:473–521.

Aramaki, T., Adrian, P. O. H., Karagiorgi, G., and Odaka, H. (2020). Dual mev gamma-ray and dark matter observatory-grams project. *Astroparticle Physics*, 114:107–114.

Ballet, J., Bruel, P., Burnett, T. H., Lott, B., and collaboration, T. F.-L. (2024). Fermi large area telescope fourth source catalog data release 4 (4fgl-dr4).

Ballet, J., Burnett, T., Digel, S., and Lott, B. (2020). Fermi large area telescope fourth source catalog data release 2. *arXiv preprint arXiv:2005.11208*.

Bechtol, K., Ahlers, M., Di Mauro, M., Ajello, M., and Vandenbroucke, J. (2017). Evidence against star-forming galaxies as the dominant source of icecube neutrinos. *The Astrophysical Journal*, 836(1):47.

Berezinskii, V., Bulanov, S., Ginzburg, V., Dogel, V., and Ptuskin, V. (1984). Astrophysics of cosmic rays. *Moscow*.

Cherenkov, P. A. (1934). Visible luminescence of pure liquids under the influence of γ-radiation. *Dokl. Akad. Nauk SSSR*, 2(8):451–454.

Cicone, C., Brusa, M., Ramos Almeida, C., Cresci, G., Husemann, B., and Mainieri, V. (2018). The largely unconstrained multiphase nature of outflows in agn host galaxies. *Nature Astronomy*, 2(3):176–178.

Collaboration, I., Abbasi, R., Ackermann, M., Adams, J., Aguilar, J., Ahlers, M., Ahrens, M., Alameddine, J., Alispach, C., Alves Jr, A., et al. (2022). Evidence for neutrino emission from the nearby active galaxy ngc 1068. *Science*, 378(6619):538–543.

Cortina, J. (2019). Status of the large size telescopes of the cherenkov telescope array. *arXiv preprint arXiv:1907.10146*.

Cortina, J. and Teshima, M. (2015). Status of the cherenkov telescope array's large size telescopes. *arXiv preprint arXiv:1508.06438*.

De Angelis, A., Tatischeff, V., Argan, A., Brandt, S., Bulgarelli, A., Bykov, A., Costantini, E., Silva, R. C. d., Grenier, I. A., Hanlon, L., et al. (2021). Gamma-ray astrophysics in the mev range: The astrogam concept and beyond. *Experimental Astronomy*, 51(3):1225–1254.

De Angelis, A., Tatischeff, V., Grenier, I. A., McEnery, J., Mallamaci, M., Tavani, M., Oberlack, U., Hanlon, L., Walter, R., Argan, A., et al. (2018). Science with e-astrogam: A space mission for mev–gev gamma-ray astrophysics. *Journal of High Energy Astrophysics*, 19:1–106.

de Bony de Lavergne, M., Emery, G., Carrasco, M.-S., Aguasca-Cabot, A., and Fröse, S. (2025). Baccmod.

De Grijp, M., Miley, G., Lub, J., and De Jong, T. (1985). Infrared seyferts: a new population of active galaxies? *Nature*, 314(6008):240–242.

Donath, A., Terrier, R., Remy, Q., Sinha, A., Nigro, C., Pintore, F., Khélifi, B., Olivera-Nieto, L., Ruiz, J. E., Brügge, K., et al. (2023). Gammapy: A python package for gamma-ray astronomy. *Astronomy & Astrophysics*, 678:A157.

Dopita, M. A. (1995). Photoionising shocks in snrs and agn. *Astrophysics and Space Science*, 233(1):215–230.

Eichmann, B., Dettmar, R.-J., and Tjus, J. B. (2021). An agn-starburst composite multi-messenger model of ngc 1068. *arXiv preprint arXiv:2108.06990*.

Eichmann, B., Oikonomou, F., Salvatore, S., Dettmar, R.-J., and Tjus, J. B. (2022). Solving the multimessenger puzzle of the agn-starburst composite galaxy ngc 1068. *The Astrophysical Journal*, 939(1):43.

Eichmann, B. and Tjus, J. B. (2016). The radio–gamma correlation in starburst galaxies. *The Astrophysical Journal*, 821(2):87.

Fabian, A. C. (2012). Observational evidence of active galactic nuclei feedback. *Annual Review of Astronomy and Astrophysics*, 50(1):455–489.

Fomin, Y. A., Kalmykov, N., Kulikov, G., Sulakov, V., and Troitsky, S. (2013). Estimate of the fraction of primary photons in the cosmic-ray flux at energies 1017 ev from the eas-msu experiment data. *Journal of Experimental and Theoretical Physics*, 117(6):1011–1023.

Gaisser, T. K., Engel, R., and Resconi, E. (2016). *Cosmic rays and particle physics*. Cambridge University Press.

Gámez Rosas, V., Isbell, J. W., Jaffe, W., Petrov, R. G., Leftley, J. H., Hofmann, K.-H., Millour, F., Burtscher, L., Meisenheimer, K., Meilland, A., et al. (2022). Thermal imaging of dust hiding the black hole in ngc 1068. *Nature*, 602(7897):403–407.

Garcia, E., Vuillaume, T., and Nickel, L. (2022). The lstmcpipe library.

Ghisellini, G. (2013). *Radiative processes in high energy astrophysics*, volume 873. Springer.

Ginzburg, V. and Syrovatskii, S. (1964). The secondary electron component of cosmic rays and the spectrum of general galactic radio emission. *Soviet Astronomy, Vol. 8, p. 342*, 8:342.

Halzen, F. and Hooper, D. (2002). High-energy neutrino astronomy: the cosmic ray connection. *Reports on Progress in Physics*, 65(7):1025.

Heitler, W. (1984). *The quantum theory of radiation*. Courier Corporation.

Hillas, A. M. (1985). Cerenkov light images of eas produced by primary gamma. In *19th Intern. Cosmic Ray Conf-Vol. 3*, number OG-9.5-3.

Horvath, J. E. (2022). *Active Galactic Nuclei (AGNs)*, pages 177–186. Springer International Publishing, Cham.

Huang, K.-Y., Viti, S., Holdship, J., García-Burillo, S., Kohno, K., Taniguchi, A., Martn, S., Aladro, R., Fuente, A., and Sánchez-García, M. (2022). The chemical footprint of agn feedback in the outflowing circumnuclear disk of ngc 1068. *Astronomy & Astrophysics*, 666:A102.

Hummel, E., Van Gorkom, J., and Kotanyi, C. (1983). Anomalous radio continuum features in edge-on spiral galaxies. *Astrophysical Journal, Part 2-Letters to the Editor, vol. 267, Apr. 1, 1983, p. L5-L9.*, 267:L5–L9.

Inoue, Y., Khangulyan, D., and Doi, A. (2020). On the origin of high-energy neutrinos from ngc 1068: the role of nonthermal coronal activity. *The Astrophysical Journal Letters*, 891(2):L33.

Inoue, Y., Khangulyan, D., and Doi, A. (2021). Gamma-ray and neutrino signals from accretion disk coronae of active galactic nuclei. *Galaxies*, 9(2):36.

Kelner, S. R., Aharonian, F. A., and Bugayov, V. V. (2006). Energy spectra of gamma rays, electrons, and neutrinos produced at proton-proton interactions in the very high energy regime. *Physical Review D—Particles, Fields, Gravitation, and Cosmology*, 74(3):034018.

Kierans, C. A. (2020). Amego: exploring the extreme multi-messenger universe. In den Herder, J.-W. A., Nakazawa, K., and Nikzad, S., editors, *Space Telescopes and Instrumentation 2020: Ultraviolet to Gamma Ray*. SPIE.

Kornecki, P., Pellizza, L., del Palacio, S., Müller, A. L., Albacete-Colombo, J. F., and Romero, G. E. (2020). γ-ray/infrared luminosity correlation of star-forming galaxies. *Astronomy & Astrophysics*, 641:A147.

Kornecki, P., Peretti, E., del Palacio, S., Benaglia, P., and Pellizza, L. (2022). Exploring the physics behind the non-thermal emission from star-forming galaxies detected in γ rays. *Astronomy & Astrophysics*, 657:A49.

Kornecki, P., Peretti, E., del Palacio, S., Benaglia, P., Pellizza González, L. J., and Romero, G. E. (2021). A multi-wavelength view of the cosmic ray confinement in star-forming galaxies.

Kubo, M., Umehata, H., Matsuda, Y., Kajisawa, M., Steidel, C. C., Yamada, T., Tanaka, I., Hatsukade, B., Tamura, Y., Nakanishi, K., et al. (2022). An agn with an ionized gas outflow in a massive quiescent galaxy in a protocluster at z= 3.09. *The Astrophysical Journal*, 935(2):89.

Le Floc'h, E., Mirabel, I., Laurent, O., Charmandaris, V., Gallais, P., Sauvage, M., Vigroux, L., and Cesarsky, C. (2001). Mid-infrared observations of ngc 1068 with the infrared space observatory. *Astronomy & Astrophysics*, 367(2):487–497.

Li, T. P. and Ma, Y. Q. (1983). Analysis methods for results in gamma-ray astronomy. *Astrophysical Journal*, 272:317–324.

Liang, E. (1979). On the hard x-ray emission mechanism of active galactic nuclei sources. *Astrophysical Journal, Part 2-Letters to the Editor, vol. 231, Aug. 1, 1979, p. L111-L114.*, 231:L111–L114.

López Coto, R. (2015). *Very-high-energy gamma-ray observations of pulsar wind nebulae and cataclysmic variable stars with MAGIC and development of trigger systems for IACTs*. PhD thesis, Autonomous University of Barcelona, Spain.

López-Coto, R., Baquero, A., Bernardos, M. I., Cassol, F., Foffano, L., García, E., Gliwny, P., Iwamura, Y., Jacquemont, M., Jouvin, L., et al. (2020). lstchain: An analysis pipeline for lst-1, the first prototype large-sized telescope of cta. In *30th Astronomical Data Analysis Software and Systems*, volume 532, page 357. Astronomical Society of the Pacific.

Maiolino, R. and Rieke, G. (1995). Low-luminosity and obscured seyfert nuclei in nearby galaxies. *Astrophysical Journal v. 454, p. 95*, 454:95.

Marinucci, A., Bianchi, S., Matt, G., Alexander, D., Baloković, M., Bauer, F., Brandt, W., Gandhi, P., Guainazzi, M., Harrison, F., et al. (2015). Nustar catches the unveiling nucleus of ngc 1068. *Monthly Notices of the Royal Astronomical Society: Letters*, 456(1):L94–L98.

Markowitz, A., Krumpe, M., and Nikutta, R. (2014). First x-ray-based statistical tests for clumpy-torus models: eclipse events from 230 years of monitoring of seyfert agn. *Monthly Notices of the Royal Astronomical Society*, 439(2):1403–1458.

Mas Aguilar, Á. (2025). Search for very high energy emission from pulsars with lst-1 telescope.

Moralejo, A., Lopez-Coto, R., Vuillaume, T., Cassol, F., Linhoff, M., Priyadarshi, C., Morcuende, D., Nozaki, S., Bernardos, M., Gliwny, P., Ruiz, J. E., deborahDOR, Dalchenko, M., yrenier, Saha, L., Nickel, L., de Bony, M., Aguasca-Cabot, A., Sitarek, J., Alispach, C., Pillera, R., Láinez, M., Andres-Baquero, Balbo, M., Muñoz, F., Takahashi, M., sn621, and yiwamura (2025). cta-observatory/cta-lstchain: v0.11.3.

Morcuende Parrilla, D. (2023). *Study of the performance of the first Large-Sized Cherenkov telescope of CTA, the relevance of fluorescence in the Cherenkov technique and the multiwavelength emission from the blazar 1ES 0647+ 250*. PhD thesis, Universidad Complutense de Madrid.

Murase, K., Kimura, S. S., and Meszaros, P. (2020). Hidden cores of active galactic nuclei as the origin of medium-energy neutrinos: critical tests with the mev gamma-ray connection. *Physical review letters*, 125(1):011101.

Murdin, P. (2001). *Encyclopedia of astronomy and astrophysics*.

Nakai, N., Inoue, M., Miyazawa, K., Miyoshi, M., and Hall, P. (1995). Search for extremely-high-velocity h2o maser emission in seyfert galaxies. *Publications of the Astronomical Society of Japan*, 47(6):771–799.

Nakai, N., Inoue, M., and Miyoshi, M. (1993). Extremely-high-velocity h20 maser emission in the galaxy ngc4258. *Nature*, 361(6407):45–47.

Nigro, C., Hassan, T., and Olivera-Nieto, L. (2021). Evolution of data formats in very-high-energy gamma-ray astronomy. *Universe*, 7(10):374.

Observatory, C. T. A. and Consortium, C. T. A. (2021). Ctao instrument response functions - prod5 version v0.1.

Oliva, E., Origlia, L., Kotilainen, J., and Moorwood, A. (1995). Red supergiants as starburst tracers in galactic nuclei. *Astronomy and Astrophysics, v. 301, p. 55*, 301:55.

Osterbrock, D. (1991). Active galactic nuclei. *Reports on Progress in Physics*, 54(4):579.

Padovani, P., Alexander, D., Assef, R., De Marco, B., Giommi, P., Hickox, R., Richards, G., Smolčić, V., Hatziminaoglou, E., Mainieri, V., et al. (2017). Active galactic nuclei: what's in a name? *The Astronomy and Astrophysics Review*, 25(1):2.

Padovani, P., Resconi, E., Ajello, M., Bellenghi, C., Bianchi, S., Blasi, P., Huang, K.-Y., Gabici, S., Gámez Rosas, V., Niederhausen, H., et al. (2024). High-energy neutrinos from the vicinity of the supermassive black hole in ngc 1068. *Nature Astronomy*, 8(9):1077–1087.

Peretti, E., Blasi, P., Aharonian, F., and Morlino, G. (2019). Cosmic ray transport and radiative processes in nuclei of starburst galaxies. *Monthly Notices of the Royal Astronomical Society*, 487(1):168–180.

Peterson, B. M. (1997). *An introduction to active galactic nuclei*. Cambridge University Press.

Pfuhl, O., Davies, R., Dexter, J., Netzer, H., Hönig, S., Lutz, D., Schartmann, M., Sturm, E., Amorim, A., Brandner, W., et al. (2020). An image of the dust sublimation region in the nucleus of ngc 1068. *Astronomy & Astrophysics*, 634:A1.

Project, C.-L., Abe, H., Abe, K., Abe, S., Aguasca-Cabot, A., Agudo, I., Crespo, N. A., Antonelli, L., Aramo, C., Arbet-Engels, A., et al. (2023). Observations of the crab nebula and pulsar with the large-sized telescope prototype of the cherenkov telescope array. *arXiv preprint arXiv:2306.12960*.

Reynolds, C., Ueda, Y., Awaki, H., Gallo, L., Gandhi, P., Haba, Y., Kawamuro, T., LaMassa, S., Lohfink, A., Ricci, C., et al. (2014). Astro-h white paper-agn reflection. *arXiv preprint arXiv:1412.1177*.

Ricci, C., Trakhtenbrot, B., Koss, M. J., Ueda, Y., Del Vecchio, I., Treister, E., Schawinski, K., Paltani, S., Oh, K., Lamperti, I., et al. (2017). Bat agn spectroscopic survey. v. x-ray properties of the swift/bat 70-month agn catalog. *The Astrophysical Journal Supplement Series*, 233(2):17.

Rigopoulou, D., Papadakis, I., Lawrence, A., and Ward, M. (1997). Millimetre line co (2-¿ 1) observations of a complete sample of agn. *Astronomy and Astrophysics, v. 327, p. 493-502*, 327:493–502.

Romero, G. E. (2021). Introducción a la astrofísica relativista. Lecture notes.

Schonfelder, V., Aarts, H., Bennett, K., Deboer, H., Clear, J., Collmar, W., Connors, A., Deerenberg, A., Diehl, R., Von Dordrecht, A., et al. (1993). Instrument description and performance of the imaging gamma-ray telescope comptel aboard the compton gamma-ray observatory. *Astrophysical Journal Supplement Series*.

Sommers, P. (2004). Extensive air showers and measurement techniques. *Comptes Rendus Physique*, 5(4):463–472.

Thompson, T. A. and Lacki, B. C. (2013). The fir-radio correlation in rapidly star-forming galaxies: The spectral index problem and proton calorimetry. In *Cosmic Rays in Star-Forming Environments: Proceedings of the Second Session of the Sant Cugat Forum on Astrophysics*, pages 283–297. Springer.

Tomsick, J. A., Boggs, S. E., Zoglauer, A., Hartmann, D., Ajello, M., Burns, E., Fryer, C., Karwin, C., Kierans, C., Lowell, A., et al. (2023). The compton spectrometer and imager. *arXiv preprint arXiv:2308.12362*.

Urry, C. M. and Padovani, P. (1995). Unified schemes for radio-loud active galactic nuclei. *Publications of the Astronomical Society of the Pacific*, 107(715):803.

Vila, G., Aharonian, F., Romero, G., and Benaglia, P. (2009). Compact objects and their emission. *Asociación Argentina de Astronomiá Book series*, page 46.

Viti, S., García-Burillo, S., Fuente, A., Hunt, L., Usero, A., Henkel, C., Eckart, A., Martin, S., Spaans, M., Muller, S., et al. (2014). Molecular line emission in ngc 1068 imaged with alma-ii. the chemistry of the dense molecular gas. *Astronomy & Astrophysics*, 570:A28.

Völk, H. J. and Bernlöhr, K. (2009). Imaging very high energy gamma-ray telescopes. *Experimental Astronomy*, 25(1):173–191.

Vrtilek, S. (2022). *Messengers of Astrophysics*, pages 1–1.

Whittle, M. (1992). Virial and jet-induced velocities in seyfert galaxies. ii-galaxy rotation as virial parameter. iii-galaxy luminosity as virial parameter. *Astrophysical Journal, Part 1 (ISSN 0004-637X), vol. 387, March 1, 1992, p. 109-137.*, 387:109–137.

Wynn-Williams, C., Becklin, E., and Scoville, N. (1985). The 3 kiloparsec radio disk and halo of ngc 1068. *Astrophysical Journal, Part 1 (ISSN 0004-637X), vol. 297, Oct. 15, 1985, p. 607-610.*, 297:607–610.

Yoast-Hull, T. M., Gallagher III, J., Zweibel, E. G., and Everett, J. E. (2013). Active galactic nuclei, neutrinos, and interacting cosmic rays in ngc 253 and ngc 1068. *The Astrophysical Journal*, 780(2):137.

Zabalza, V. (2015). naima: a python package for inference of relativistic particle energy distributions from observed nonthermal spectra. *Proc. of International Cosmic Ray Conference 2015*, page 922.